SAPIENZA
UNIVERSITÀ DI ROMA

Sapienza Università di Roma
Department of Physics

Accelerator Physics PhD School - XXIX cycle

Design, realization and commissioning of RF Power system and accelerating structures for a Gamma Source

PhD Thesis of:
Fabio Cardelli

Director of Doctoral School:
Prof. Riccardo Faccini

Supervisor:
Prof. Luigi Palumbo
Co-supervisor:
Dr. David Alesini

A.A. 2016/2017

Commission of the final examination:

Prof. Antonio Capone - Universitá degli studi di Roma “Sapienza”

Prof. Danilo Giulietti - Universitá di Pisa

Prof. Renato Fedele - Universitá degli studi di Napoli “Federico II”

Referee of this work:

Dr. Gerardo D’Auria - Elettra Sinctrotrone, Trieste

Dr. Fabio Marcellini - Paul Sherrer Institute - PSI (CHE)

Final examination:

Date 21-01-2017

Universitá degli studi di Roma “Sapienza”, Rome, Italy

Contents

Introduction

Thanks to the recent technological progress in the fields of high power lasers and high brightness linac accelerators, new γ and X ray sources based on electron-photon interaction are under development in several laboratory world-wide.
These kind of sources uses Inverse Compton scattering in the collision between a relativistic high quality electron beam and high power optical laser pulses to generate secondary photon beams of unique performances. These photon beams are suitable for a wide range of applications and open new perspectives in many research fields. In particular gamma rays in the energy interval between 1-20 MeV are of great interest for basic research and application studies in the fields of nuclear physics and photonics.

In this framework, a very innovative Compton source is under construction in Magurele (RO), by the EuroGammaS association, with the aim to generate photon beams in that energy range, characterized by unprecedented performances in terms of mono-chromaticity, brilliance, spectral density, tunability and polarization. The realization of this source called ELI-NP-GBS is in the framework of the European Extreme Light infrastructure (ELI) project that pursues the creation of an international laser research infrastructure.

The challenging parameters of this source rely on the performances of the Linac and in particular of his radiofrequency (RF) system. The electron accelerator is a high brightness normal conducting RF Linac consisting of two S-band

(2856 MHz) and twelve C-band (5712 MHz) RF structures. The main advantages of using a Linac accelerator are the energy ”tunability” and the excellent electron beam quality that is possible to obtain. The accelerator will be operated at a repetition rate of 100 Hz. For every RF pulse up to 32 electron bunches, each one carrying 250 pC of charge, separated by 16 ns, will be accelerated. The Linac is required to achieve a normalized emittance in both planes better than 0.5 mm·mrad and energy spread below 0.1%. To guarantee these performances in a reliable and stable way, innovative and advance RF components have been developed. The aim of this thesis is the study, design and commissioning of the main components of RF system used for the realization of a state of the art gamma source such as the ELI-NP-GBS. High power RF sources driven by solid state modulators have to feed the accelerating structures with high pulse to pulse amplitude stability and RF pulse uniformity in order to minimize the electron beam energy spread. An innovative C-band High Order Mode (HOM) damped RF cavity has been conceived and designed in order to avoid beam emittance and energy spread degradation due to the Beam Break-Up instability along the Linac. In addition the S-band RF Gun has been realized with an innovative technique called “Gasket-clamping technique” and implements new radiofrequency features to sustain the 100 Hz repetition rate operation. All these devices have been realized and tested and the results obtained are reported in this work. Taking into account the extremely good results obtained by RF Gun realized with the gasket-clamping technique, in the last part of this dissertation, it has been explored the possibility to extend this fabrication procedure to the realization of an entire travelling wave Linac structure. This technique, thanks to the use of RF/vacuum special gaskets, allows avoiding the brazing process thus reducing the fabrication costs, the risk of failure and improving the performances of the device in terms of reachable peak electric field. To demonstrate the feasibility of the implementation of such technique an accurate electromagnetic and mechanical design of an S-band travelling wave structure has been performed.

Dissertation overview

The work for this dissertation is described in a total of five Chapters. In Chapter 1 physics of the Compton backscattering is introduced with a general overview of the Compton sources and their wide range of applications. In this scenario we also discuss the main parameters of the European ELI-NP-GBS project. Finally the Linac parameters and the layout of the machine are reported. Chapter 2 focuses on the Linac RF system. The entire waveguide network is described with particular attention to the RF sources composed by the modulator and the klystron. After a general description of the two systems the tests performed on the ELI-NP RF sources are reported. This Chapter ends with a description of Low Level RF system. In Chapter 3 the C-band HOM damped travelling wave structures designed for the ELI-NP source are described. The mechanical design and the realization procedure are also discussed. After their realization the structures have to be tuned in order to show the right phase advance per cell. Hence, the tuning procedure and measurement set-up are presented with the high power tests results, performed at the Bonn University, that demonstrated the capabilities of these devices to work at the nominal gradient (33 MV/m), nominal repetition rate (100 Hz) and long RF pulses for the multibunch operation. In Chapter 4 the RF Gun used in the ELI-NP photoinjector is presented. We also discuss the low and high power test results that confirmed the effectiveness of the gasket clamping technique for the fabrication of RF structures. In the last Chapter the design of an S-band LINAC structure that implements the gasket clamping technique is presented. The electromagnetic and mechanical designs are discussed and the first realized one-cell prototype is showed. In the conclusions, perspectives and future works for all these activities are put in evidence.

CHAPTER

1 Gamma Sources

Content

Recent developments in particle accelerators and lasers technology opened new perspectives for the realization of new X and γ ray sources through electron-photon collision. These sources are based on the inverse Compton scattering effect, in which a high brightness electron beam scatters an intense high power laser beam, converting optical photons ($E_{ph} \sim$ eV) into energetic photons ranging from keV to MeV.

1.1 Inverse Compton Scattering

The physics of the inverse Compton scattering effect has been studied extensively and can be described through two different models [1]: classical model and a linear quantum model. In the former the laser pulse field acts as an elec-

tromagnetic undulator. Like in a Free Electron Laser (FEL), the electrons oscillating in this field produce spontaneous emission radiation due to the transverse acceleration. This model considers all the collective effects (multi-photon absorption/emission) explaining the beam/laser pulse interaction within certain limits, but does not conserve energy and momentum. In order to take into account the quantum effects and how they impact on the quality of the produced secondary beam, the linear quantum approach is used. It is based on the relativistic kinematics and allows to predict the final characteristics and performances for a high energy Compton source.

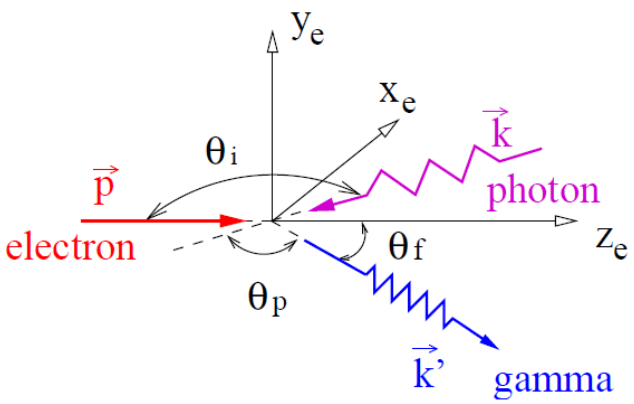

Figure 1.1: Sketch of Compton scattering of an electron and a photon in a laboratory frame coordinate system (x_e, y_e, z_e) in which the electron is incident along the z_e direction. The incident photon is propagating along the direction given by the polar angle θ_i and azimuthal angle ϕ_i. The collision occurs at the origin of the coordinate system. After the scattering, the scattered gamma ray propagates in the direction given by the polar angle θ_f and azimuthal angle ϕ_f. θ_p is the angle between the momenta of incident and scattered photons. The electron after scattering is not shown in the figure.

As reported in [2], in the laboratory frame shown in Figure 1.1 the energy E_γ of the scattered gamma ray, propagating in the direction given by the polar angle θ_f, can be expressed by

$$E_\gamma = \frac{(1-\beta\cos\theta_i)E_p}{1-\beta\cos\theta_f+(1-\cos\theta_p)E_p/E_e} \tag{1.1}$$

where $\beta = v/c$ is the ratio of the incident electron velocity relative to the speed of light, E_e and E_p are the energy of the electron and optical photon before scattering, θ_i is the angle between the momenta of the incident photon and the electron and θ_p is the angle between the momenta of the incident and scattered photons.

In case of head-on collision ($\theta_i = \pi$ and $\theta_p = \pi - \theta_f$) and ultra-relativistic electron ($\gamma \gg 1, \beta \sim 1$), the photon is scattered into a cone with a half-opening angle of $1/\gamma$ along the direction of the incident electron, where $\gamma = E_e/(mc^2)$ is the Lorentz factor of the electron and $E_0 = mc^2$ is its rest energy. For a small scattering angle, ($\theta_f \ll 1$), the equation 1.1 can be simplified to

$$E_\gamma \simeq \frac{4\gamma^2 E_p}{1 + \gamma^2\theta_f^2 + 4\gamma^2 E_p/E_e} \tag{1.2}$$

in which the last term in the denominator accounts for the so called electron recoil effect and it is responsible for the correct energy and momentum conservation in the scattering reaction. This term, that affects the performances of the emitted photon beam, is negligible for X ray Thomson Sources, while it is small but not negligible for higher energy Compton Sources, and becomes the dominant term for deep Compton Sources.

In general is possible to identify three different regimes:

- Thomson elastic regime: negligible electron recoil;
- Quasi-elastic Compton regime: small but not negligible recoil;
- Quantum Compton regime: dominant electron recoil.

As shown by equation 1.2, the photon energy gain factor in the inverse Compton scattering mainly depends on the energy of the colliding electron beam. This beam can be generated by a normal conducting linear accelerator (Linac), a storage ring or a superconducting Linac. Compton sources are easily tunable and their photon beam energies can be extended to cover a wide range from soft X ray to very high energy gamma ray. Due to a high energy gain factor, the Compton sources are considered the most effective ”photon accelerators”, able

to produce high power radiation with a required electron beam energy, dimensions and costs significantly lower than those of a synchrotron light source.

Furthermore, secondary photons emitted by inverse Compton scattering present an energy-angle correlation. Hence, by using a collimation system, it is possible to obtain a quasi-monochromatic photon beam, while the forward focusing ensures high spectral densities in small bandwidths. Compared with a Bremsstrahlung beam which is characterized by a broad band spectrum, a Compton beam is narrowly peaked around the desired energy. Another important feature is the preservation of the laser polarization in the scattered photons. Hence, the photon beams produced with this scheme can be highly polarized, and their polarization is controlled by the one of the incident photon beam.

Summarizing the Compton sources are able in producing radiation with high power, short wavelength, quasi-monochromatic spectrum, high directivity, ultrashort time duration and tunability.

1.2 Overview and applications

Compton sources can be seen as electron/photon colliders aimed at producing secondary beams of photons. Unlike normal colliders used for high-energy physics, where collisions are used to study rare physical events, in these machines the emphasis is on the secondary particle beam and his properties.

The idea of using Compton scattering to generate a high-energy X ray or γ ray beam was first proposed in 1963 by Milburn and Arutyunian [3, 4]. The LADON project [5] has been the first facility to produce a monochromatic polarized gamma beam exploiting the collision of a laser with the electrons from the ADONE storage ring [6] in Frascati.

Nowadays several test facilities, that generate γ ray beams by means of Compton scattering are present in different laboratories worldwide [7, 8, 9, 10, 11, 12], together with newly conceived user facilities [13, 14, 2, 15]. This is true both for X-ray sources, which are primarily used for advanced imaging techniques, and for the gamma-ray sources used for research in nuclear physics and industrial purposes. Such a new generation of γ beams allow to probe the matter on microscopic-to-nuclear scales in space and time. They found their natural

interest in imaging and nuclear fundamental physics, but their potential application range extends to a large number of fields: medicine, biology, material science, cultural heritage, national security and high energy physics. Photon beams generated by Compton scattering have been successfully used for the implementation of biological computer aided imaging techniques, like for instance phase-contrast tomography at the Munich Compact Light Source [13, 16]. This has been possible thanks to small round source spot size ($\sim 10\mu m$), high spatial ($\sim 80\mu m$) and temporal resolution (ps) and quasi-monochromaticity typical of these sources. Moreover, with respect to the conventional X ray tubes, the absence of low energy tails in the photon spectrum, allows edge enhancement with an overall improvement in the image contour visibility. In particular in the medical field, mammography with mono-chromatic X-rays at 20 keV has been proven far superior in signal to noise ratio with respect to conventional mammographic tubes, with a considerably lower radiation dose to the tissue.

The generation of photons in the gamma range ($E_{ph} > 1$ MeV) is particular interesting for nuclear physics applications, e.g. the Nuclear Resonance Fluorescence technique [17, 18] based on the nuclear absorption and subsequent emission of high-energy photons. This technique provides a versatile method of non-destructive analysis of both radioactive and stable nuclides. Therefore, it finds application for nuclear waste remote sensing and diagnostics, special nuclear material recognition for national security but also in isotope sensitive imaging for medical and cultural heritage purposes. Moreover, several research fields in nuclear physics and astro-physics dealing with fundamental nuclear structure studies such as nucleo-synthesis, clustering phenomena in light nuclei, photo-disintegration cross sections measurements and photo-fission phenomena will be possible by using such advanced gamma sources.

1.3 ELI-NP-GBS project

A new Compton source operating in the gamma energy range (0.2-19.5 MeV) that aims to provide a beam suitable for the applications mentioned in the previous paragraph, is presently under construction in the framework of the Extreme

Light Infrastructure Nuclear Physics Gamma Beam System (ELI-NP-GBS) project.

The ELI-NP-GBS project [19, 20, 21] consists in the realization and commissioning of a gamma ray source that will be hosted in Magurele, near Bucharest (RO). The conceivement and design of this machine has been performed by the EuroGammaS association [22] which gathers academic and research institutions together with commercial companies: Istituto Nazionale di Fisica Nucleare, Università di Roma "La Sapienza", the Centre National de la Recherche Scientifique, ACP S.A.S., Alsyom S.A.S., Comeb Srl and ScandiNova Systems AB. This project has been developed in the framework of the ELI project, born from the collaboration of 13 European countries and aims at the creation of an international laser research infrastructure that will host high-level research on ultra-high intensity laser, laser-matter interaction and secondary light sources. Its scope is to reach pulse peak power and brightness beyond the current state of the art by several orders of magnitude. Because of its unique properties, this multidisciplinary facility will provide new opportunities to study the fundamental processes unfolded during light-matter interaction. ELI will be implemented as a distributed research infrastructure based initially on 3 specialized and complementary facilities (or pillars):

- ELI Beamlines (Prague (CZ)): High Energy Beam Science pillar devoted to the development and usage of dedicated beam lines with ultra short pulses of high energy radiation and particles reaching almost the speed of light.
- ELI Attosecond (Szeged (HU)): Attosecond Laser Science pillar designed to conduct temporal investigation of electron dynamics in atoms, molecules, plasmas and solids at attosecond scale (10^{-18} s).
- ELI-NP (Magurele (RO)): Laser-based Nuclear Physics pillar will generate radiation and particle beams with much high energy and brilliance suited to studies of nuclear and fundamental processes.

At the ELI-NP pillar, the ELI-NP-GBS is foreseen as a major component of the infrastructure, aiming at producing extreme gamma ray beams for nu-

clear physics and photonics experiments characterized by unprecedented performances in terms of monochromaticity, brilliance, spectral density, tunability and polarization.

The ELI-NP source [21, 23] is a machine based on the collision of an intense high power Yb:Yag J-class laser and an high brightness electron beam with a tunable energy produced by a normal conducting Linac. Referring to equation 1.1 this source operates at the transition between the classical and the quantum regimes, since the required bandwidth is very narrow the quantum effects cannot be neglected. The main specifications of the Compton Source are: photon energy tunable between 0.2 and 19.5 MeV, rms relative bandwidth lower than 0.5% and spectral density larger than $5 \cdot 10^3$ photons/s·eV, with source spot size smaller than 100 μm and linear polarization of the gamma-ray beam larger than 95%. Moreover, the peak brilliance of the gamma beam is expected to be larger than 10^{19} photons/(s·mm^2 · mrad^2 · 0.1%). To reach these challenging specifications, the luminosity $\mathscr{L}$ of the source must be larger than 10^{35} s^{-1}· cm^{-2}, as specified by equation

$$\mathscr{L} = \frac{N_e N_p r}{4\pi\sigma_0^2} \tag{1.3}$$

where N_p are the photons carried by the laser pulse at the collision, N_e the electrons carried in the bunch, σ_0 the spot size at the Interaction Point (IP) and r the repetition rate of the collisions (assuming ideal overlap in space and time of the two colliding pulses, as well as negligible diffraction of the two beams over the interaction distance). The total number of photons scattered per second, all over the spectrum and solid angle, is given by the luminosity multiplied by the total cross section $N = \mathscr{L} \cdot \theta_{tot}$, in our case $N = 7 \cdot 10^{10}$ photons/s. Any Compton source generates polychromatic beam. Hence, in order to produce a monochromatic photon beam it is necessary to select a narrow cone around the electron beam propagation axis by means of special collimators. Therefore, what really matters for experiments and applications is the number of photons carried by the radiation pulse within such a small angle N^{bw}, and their associated rms bandwidth $\Delta\nu_p$. This is the definition of spectral density, which is the figure of

merit interesting for nuclear physics and photonics applications. The Spectral Density, defined as

$$SD = \frac{N^{bw}r}{\sqrt{2\pi}\Delta\nu_p} \tag{1.4}$$

is typically expressed in units of photons/$s \cdot eV$. Various generations of machines have improved this parameter, from values of the order of 1 for bremsstrahlung sources, to about 10^2 for the present HiγS facility [2], towards the 10^4 range which is the goal of ELI-NP-GBS. Since the laser pulse carries about 10^{18} photons at the IP, but only a maximum of 10^7 photons are scattered at each collision (in other words the electron beam is almost transparent to the laser pulse), the laser pulse can be "re-used" bringing it back to a new collision at the same IP with a new incoming electron bunch. To recirculate the laser pulse an advanced and innovative laser re-circulator has been developed and it is presently under test. A full description of this new optical device can be found in [24, 25].

To achieve this outstanding performance the laser pulse needs to be recirculated 32 times at the interaction point and consequently the Linac will accelerate 32 electron bunches (separated by 16 ns) within the same RF bucket, with a repetition rate of 100 Hz. The final parameters of the gamma beam of ELI-NP GBS are summarized in table 1.1 and the layout of the entire building is shown in Figure 1.2.

1.4 Description of the ELI-NP Linac

In order to reach these challenging performances that are at least two orders of magnitude higher than the present state of the art (in terms of gamma beam bandwidth, brilliance and spectral density) innovative and advanced components have been developed specifically for this machine. In particular, to accelerate the multi-bunch electron beam, the ELI-NP-GBS adopts an S-band (2856 MHz) photo-injector coupled to a C-band (5712 MHz) radiofrequency (RF) Linac capable to bring the electron beam up to an energy of 740 MeV with outstanding

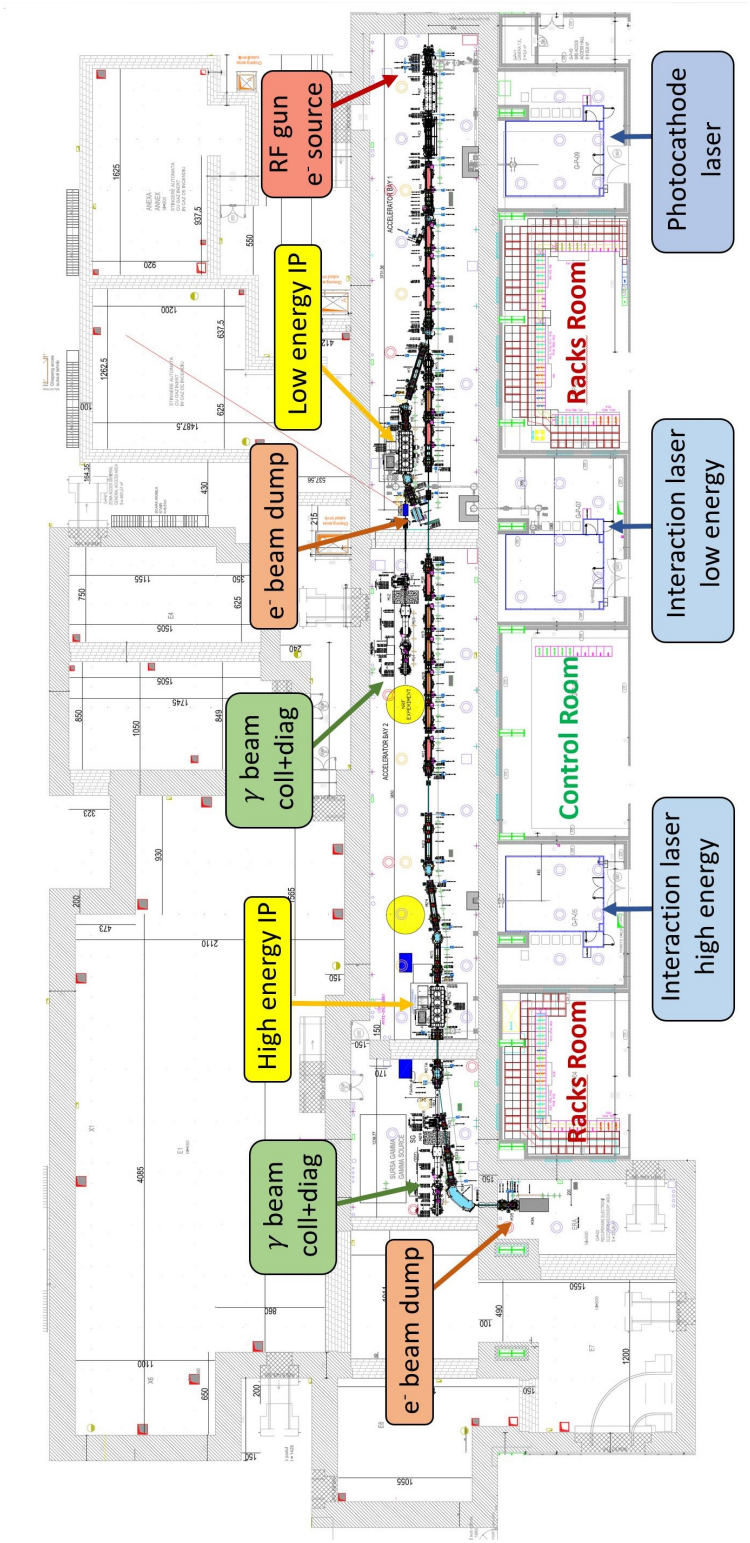

Figure 1.2: ELI-NP-GBS layout.

Parameter	Value
Energy [MeV]	$0.2 - 19.5$
Spectral density $[ph/s \cdot eV]$	$0.8 - 4 \cdot 10^4$
Bandwidth rms [%]	≤ 0.5
# photons/pulse within FWHM bdw	$\leq 2.6 \cdot 10^5$
# photons/s within FWHM bdw	$\leq 8.3 \cdot 10^8$
Source rms size $[\mu m]$	$10 - 30$
Source rms divergence $[\mu rad]$	$25 - 200$
Peak brilliance $[N_{ph}/s \cdot mm^2 \cdot mmrad^2 \cdot 0.1\%]$	$10^{20} - 10^{23}$
Radiation pulse length rms [ps]	$0.7 - 1.5$
Linear polarization [%]	> 99

Table 1.1: Main parameters of the ELI-NP-GBS Gamma beam.

beam quality [26]: normalized rms emittance in both planes below 0.5 mm $\cdot$ mrad and energy spread below 0.1%. In table 1.2 are summarized the main required parameters of the electron beam. As already mentioned, to increase as much as possible the number of collision per second, the Linac will work at 100 Hz repetition rate and in multi-bunch scheme. These requirements have direct impact on the design of the accelerating structures and in the overall RF system. In the design phase of the Linac components, we had to take into account the longitudinal and transverse wakefields produced by the passage of the bunches, in order to compensate the beam loading effect and avoid beam instabilities, like the multibunch beam break-up (BBU). Moreover, an accurate thermal design of the accelerating structures and of the power sources has been performed to understand the capability to withstand the effective repetition rate of 3.2 kHz.

To realize a reliable and compact machine a hybrid S/C-band scheme has been chosen. The combination of C-band acceleration with an S-band injector allows to obtain good performance in terms of beam quality [27]. The injector is derived from the one of SPARC_LAB Linac [28, 29] at INFN Frascati laboratories and is composed by one 1.6 cell RF gun with copper photo-cathode and emittance compensation solenoid, followed by two SLAC-type 3 m long Travelling Wave (TW) sections. The picture of the ELI-NP-GBS injector assembled at INFN-LNF is given in Figure 1.3. To compensate space charge effect in the

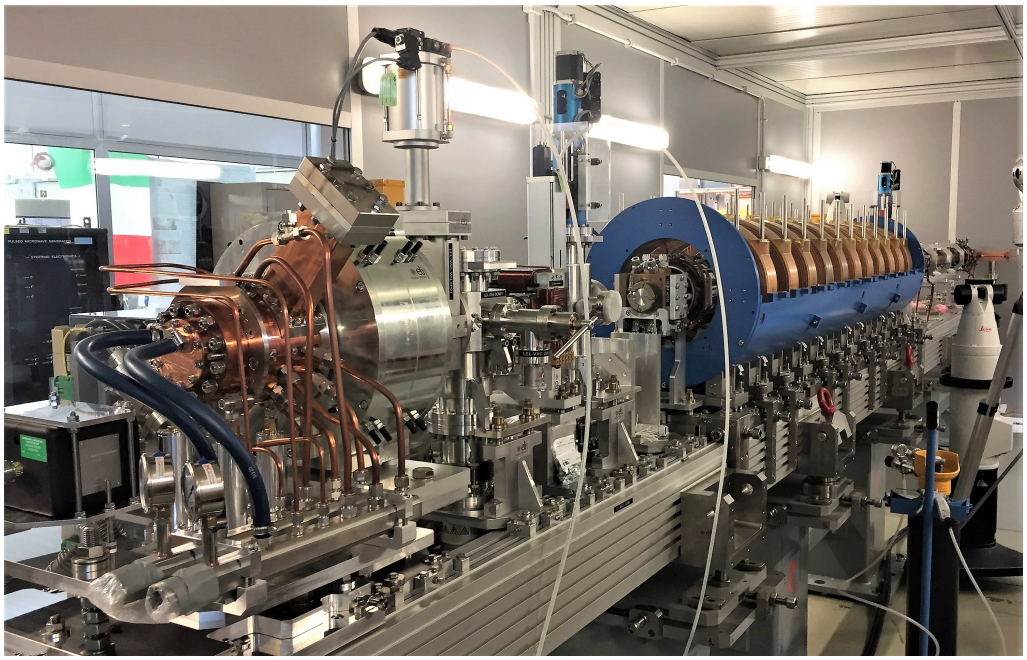

Figure 1.3: Picture of the assembled ELI-NP-GBS S-band injector.

gun region and to reduce the bunch length, the velocity bunching technique [30] is applied in the first accelerating section placed after the gun. This technique consists in injecting a non-relativistic beam in an RF structure with a phase near the zero crossing of the acceleration field. In this way the beam slips back up to the acceleration phase undergoing a quarter of synchrotron oscillation and is chirped and compressed. In the ELI case, a "gentle" velocity bunching (compression factor < 3) in the first accelerating section allows injecting into the C-band booster a beam that is short enough to reduce the final energy spread, avoiding also emittance degradation. In the first accelerating section, the transverse emittance dilution is controlled by using a solenoid embedding the RF compressor. The C-band booster comprises twelve TW C-band room temperature accelerating structures, downstream of the S-band photo-injector.

Two beamlines are planned to deliver the electron beam at the two Compton IPs: one at low energy ($E_{e^-} = 75 - 312$ MeV) and one at high energy (E_{e^-} up to 740 MeV). Downstream the injector and the first four C-band structures, a dogleg with two dipoles provide an off axis deviation towards the low energy interaction point. At the end of the Linac a second dogleg drives the

beam to the high energy Compton IP. After each interaction point the electron beam is driven through dipoles towards the low and high energy dump, while the Compton radiation proceeds in straight direction towards the collimator and the γ ray diagnostics (Compton spectrometer, calorimeter etc.) in the experimental rooms. The lattice design of the Linac takes into account a diagnostic section after the first C-band structure. This will perform the 6-D phase space characterization at the exit of the photoinjector, by means of an RF deflector combined with an adjacent spectrometer using the quadrupole scan technique. Another diagnostic station with RF deflector is foreseen after the first dogleg. In Figure 1.4 a detailed schematic of the Linac is shown, reporting also the position of all the quadrupoles, dipoles, beam position monitors and steerers along the machine. The overall accelerator has been divided in 36 modules that have been pre-assembled and tested, in order to reduce the time needed to install the machine on site. The total length of the accelerator is about 90 m.

Parameter	Value
Energy [MeV]	$75 - 740$
Bunch charge [pC]	$25 - 400$
# bunch per pulse	32
Bunch distance [ns]	16
Bunch length [μm]	$100 - 400$
Energy spread (rms) [$\%$]	0.04 - 0.1
Normalized emittance [$mm \cdot mrad$]	0.4
RF pulse repetition rate [Hz]	100

Table 1.2: Electron beam parameters of the ELI-NP-GBS Linac.

Parameter	Value
Pulse energy [J]	$0.2 - 0.4$
Wavelength [nm]	515
Photon energy [eV]	2.4
Pulse length [ps] rms	1.5
Focal spot size w_0 [μm]	28
Laser M^2	< 1.2
rms bandwidth	< 0.1
Laser parameter a_0	0.02 - 0.04
Collision angle α [$^\circ$]	172
Repetition rate [Hz]	100
Recirculator rate per laser pulse	32

Table 1.3: Laser pulse main parameters of the ELI-NP-GBS.

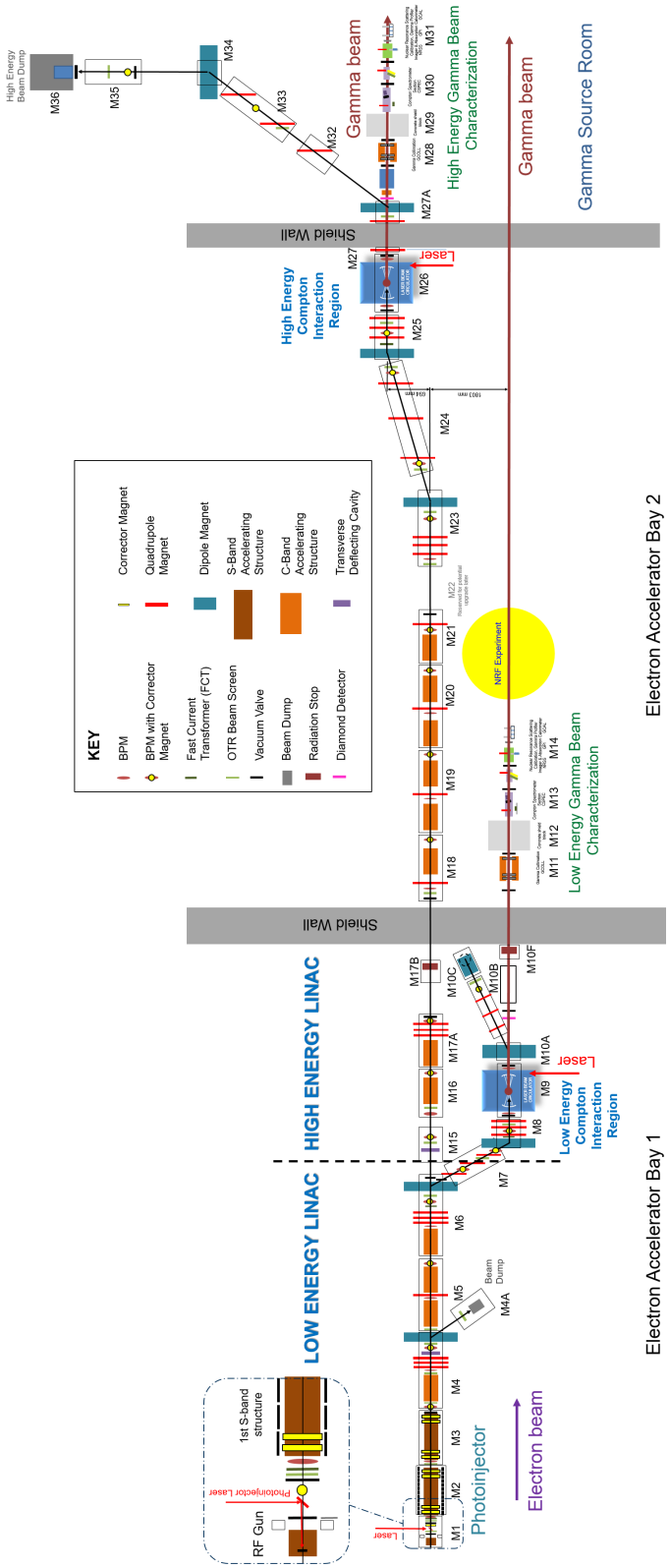

Figure 1.4: ELI-NP-GBS Linac layout.

CHAPTER

2 RF System of the ELI-NP Linac

Content

2.1 Introduction

In a radiofrequency Linac the electron beam gains energy by means of RF electric fields confined in accelerating structures and generated with high peak power sources. The RF power is distributed to the accelerating structures with a network of waveguides (made in general of copper). The sources consists of high power microwave amplifiers called klystrons that are pulsed by high voltage power supplies known as modulators. The klystrons are driven with amplifiers

that pre-amplify the signal received from the low level radiofrequency system (LLRF) up to 100-400 W.

As discussed in the previous chapter the ELI-NP linac is composed by an S-band injector followed by a C-band booster. In order minimize the energy spread along the bunch train due to beam loading effects, the pulses have to be properly shaped by the LLRF system. Therefore, the choice of RF pulse compression schemes, that in principle would allow to reduce the number of required klystrons, has not been pursued. Thus, each structure is individually fed by a dedicated power station (except for the last 4 TW sections that are powered by 2 klystrons), which also allows to have a higher operational flexibility.

A schematic sketch of ELI-NP RF system is shown in Figure 2.1.

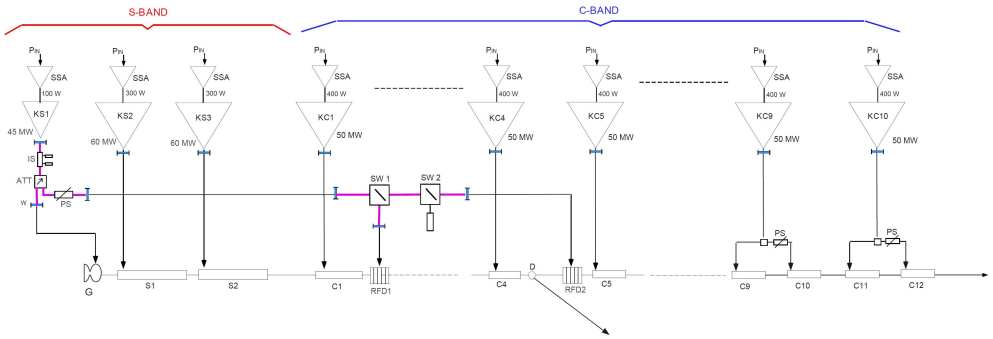

Figure 2.1: Sketch of the RF power and distribution system of the ELI-NP Linac.

The injector is composed by an RF Gun powered by a 45 MW S-band power source and two S-band travelling wave structures fed with two 60 MW sources. Considering the filling time of these structures (800 ns) and the beam length (512 ns), the S-band power sources must generate a stable and flat RF pulse $> 1.3\,\mu$s pulse width. The Linac scheme is then completed by two deflecting cavities, for beam longitudinal diagnostics at low and high energy, feed by the same power source of the Gun. The energy booster consists of a series of twelve C-band travelling wave accelerating structures. The filling time of each structure is $313\,ns$ therefore the RF pulse width has been defined equal to 1μs. Eight of these structure are powered individually by 50 MW C-band RF sources while the last four are fed in couple splitting the power with a magic T coupler. In table 2.1 the parameters of the Gun, S-band and C-band TW structure are summarized.

In this chapter the power distribution network of the ELI-NP Linac is described, including tests on some network devices. The RF power sources are described and the acceptance tests on Modulator and klystron systems are shown with a brief description of the LLRF system. The C-band accelerating structures and the RF Gun will be described in detail in chapter 3 and 4.

Parameter	**S-band RF Gun**
Frequency [MHz]	2856
Filling time [ns]	420
Max RF pulse duration [μs]	2 (1.5 nominal)
Max RF input power [MW]	2 (16)
RF pulse duration for beam [μs]	0.5
Shunt impedance [MΩ]	1.64
Unloaded Q factor	14600
Working temperature [°C]	34
Operating vacuum pressure [mbar]	$1 - 5 \cdot 10^{-9}$

Parameter	**S-band struct.**	**C-band struct.**
Frequency [MHz]	2856	5712
Number of structures	2	12
Structure length [m]	3	1.8
Filling time [ns]	800	313
Max RF pulse duration [μs]	1.3	0.8
Max RF input power [MW]	45	40
Average accel. gradient [MeV/m]	23.5	33
Average shunt impedance [MΩ/m]	53	70
Unloaded Q factor	12300	8860
Working temperature [°C]	30	30
Operating vacuum pressure [mbar]	$5 \cdot 10^{-9} - 10^{-8}$	$5 \cdot 10^{-9} - 10^{-8}$
Type	CG	quasi CG

Table 2.1: Parameters of the ELI-NP RF structures: RF Gun, S-band structures and C-band structures.

2.2 Power distribution network

In the ELI-NP Linac the RF power is distributed to each accelerating structure by means of a network of copper rectangular waveguides. For the S-band injector we use the standard WR284 waveguides (inner dimensions of 72 mm $\times$ 34 mm), while for the C-band booster the WR187 waveguide (inner dimensions of 47 mm $\times$ 22 mm) has been adopted. The waveguide are connected through flanges: for the S-band the standard is the "LIL" type while for the C-band system it is the "Riken-Desy" type. The waveguide material is Oxygen Free High Conductivity (OFHC) copper, that guarantees high thermal conductivity and good vacuum performances. The waveguides operate in ultra-vacuum, with a pressure lower than 10^{-7} mbar to avoid internal arcs due to the high peak power conveyed to the accelerating structures. Moreover, all the network is stabilized in temperature at 35 ± 1°C, to avoid length variation due to different operating conditions. This is achieved by means of copper pipes with circulating water, welded longitudinally along the external broader surface of the waveguides. The waveguide resistive losses at nominal operating frequencies for WR284 and WR187 are 0.02 dB/m and 0.035 dB/m respectively. Hence, all the power units have been evenly distributed on the building roof above the accelerator bunker to reduce the waveguides length thus minimizing the power losses.

To verify the final available power at the accelerating structures input, a first order evaluation of the total attenuation along the different branches of the waveguide network has been performed. The length of the different waveguide tracks have been evaluated from the 3D model of the power distribution network. The results of this analysis are reported in Figure 2.2, where the maximum available power at the input of the different accelerating structure is "P_{in} section". The maximum energy gain has been computed assuming the particles propagating "on crest" in the accelerating structures. The output power available for each klystron has been kept lower than the maximum achievable to increase the plant safety margin with a consequent improvement in reliability. Moreover, in order to take into account the attenuation due to waveguide flange connections and to consider the worst case scenario, the attenuation has been increased by 5% with respect to the theoretical one.

Section	WG length [m]	P_{out} Klystron [MW] Max	P_{out} Klystron [MW] available	Theoretical Atten. [dB]	Attenuation [dB]	Pin section [MW]	Maximum Energy gain [MeV]
Gun	16	45	40	0.32	1.13	15.00	6
S1	11	60	55	0.22	1.10	49.79	71.21
S2	12	60	55	0.24	1.11	49.56	71.04
S-band Linac	--	--	--	--	--	--	≤148
C1	10	50	45	0.35	1.14	39.54	59.96
C2	13	50	45	0.46	1.17	38.59	58.79
C3	12	50	45	0.42	1.16	38.91	59.03
C4	13	50	45	0.46	1.17	38.59	58.79
C5	10	50	45	0.35	1.14	39.54	59.96
C6	10	50	45	0.35	1.14	39.54	59.96
C7	10	50	45	0.35	1.14	39.54	59.96
C8	10	50	45	0.35	1.14	39.54	59.96
C9	9	25	22.5	0.32	1.13	19.93	42.40
C10	11	25	22.5	0.39	1.15	19.61	42.06
C11	9	25	22.5	0.32	1.13	19.93	42.40
C12	11	25	22.5	0.39	1.15	19.61	42.06
Total Energy	--	--	--	--	--	--	≤793

Figure 2.2: Power calculations along the waveguide network.

The first waveguide network which connects the 45 MW klystron to the RF gun and deflecting cavities includes different RF devices. The position in the network layout of such devices can be seen in Figure 2.3, where a 3D drawing is reported.

Since the Gun and the deflectors are standing wave cavities, they are not intrinsically matched to the klystron output. To protect the klystron themselves from the reflected power that occurs at the rise and fall edges of the RF pulses or in case of internal discharges, an isolator (or circulator) [31] has been inserted between the source and the cavities. The amplitude of the signal feeding the gun and the deflectors can be varied with a variable attenuator that in this case acts like a power divider. A picture of this device is reported in Figure 2.4. This device used a motorized phase-shifter in combination with three 3dB hybrids to split the power at input port between the two output ports at the desired ratio.

The power divider has been fully characterized measuring the output power level at the output ports (2, 3) with a power meter, while the input port (1) was feed with a 10 dB calibrated signal. The results of the measurements are shown in Figure 2.5.

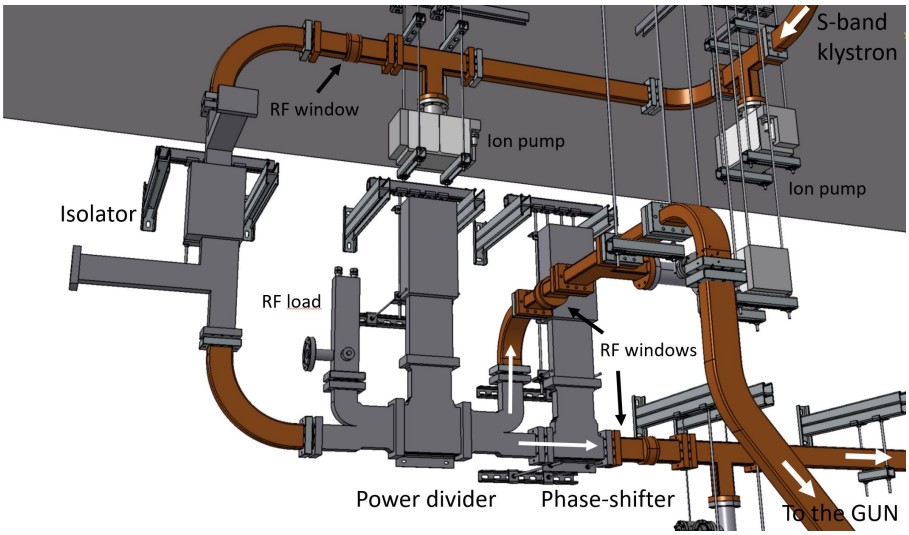

Figure 2.3: 3D drawing of the first network waveguide branch which connects the first klystron to the S-band RF Gun and the two deflecting cavities.

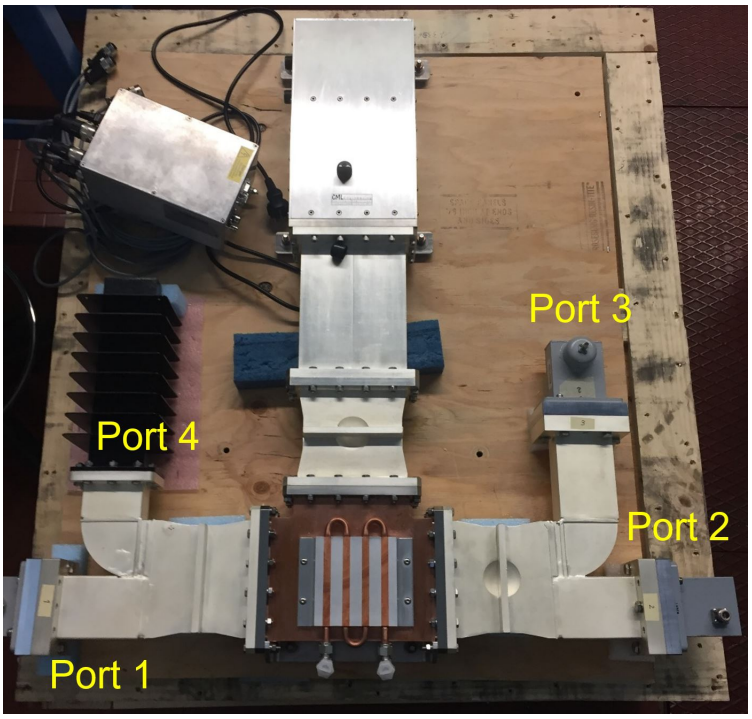

Figure 2.4: Picture of the ELI-NP S-band power divider during the low power measurement.

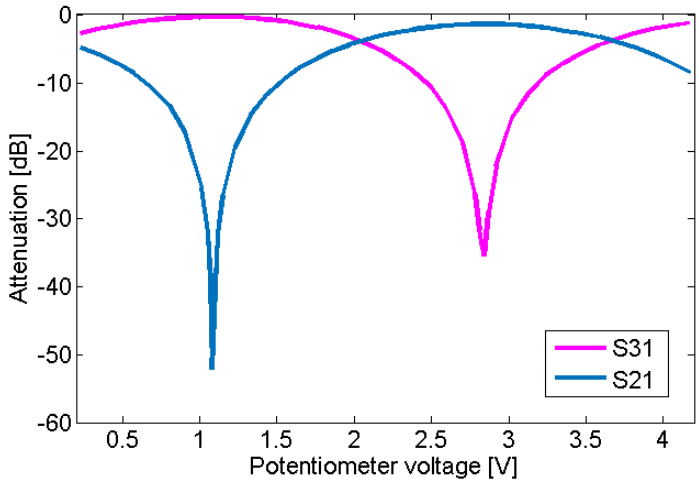

Figure 2.5: Measurement of S21 and S31 as function of the voltage of the motor potentiometer, of the ELI-NP S-band power divider.

In its final installation one output port (port 3) is connected to the waveguide of the RF gun while the other (port 2) to a phase-shifter which allows changing the phase of the electromagnetic field that travels towards the deflecting cavities. The phase-shifter is shown in Figure 2.6. This device has been characterized at low RF power through a vector network analyzer. Figure 2.7 shows the measured phase of S21 as function of the voltage potentiometer (which is related to the step motor position).

After the phase-shifter two S-band RF switches, mounted in series, allow selecting the feeding of one of the two deflecting cavities. They also provide 120 dB of isolation that guarantees the completely absence of field inside the two resonant cavities when the switches are closed. A picture of the ELI-NP RF switches is reported in Figure 2.8. The RF signal, coming from the power divider and phase-shifter, enters at port 1 then normally when the deflectors are switched off the power goes to an RF load. If switch 1 or switch 2 are ”open” the RF signal is routed to the first deflector (port 2) or the second (port 3) respectively.

Two segments of the RF-gun waveguide network are pressurized to 2 atm with sulfur-exafluoride (SF6) because the isolator and the two switches (employing ferrite materials or movable components), are not suitable to operate in ultra-high vacuum, due to their high out-gassing rate. SF6 is a gas that is

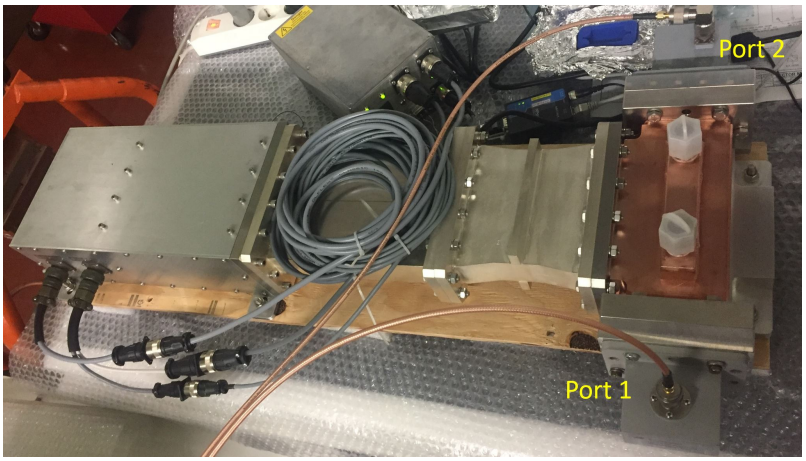

Figure 2.6: Picture of the ELI-NP S-band phase-shifter during the low power measurement.

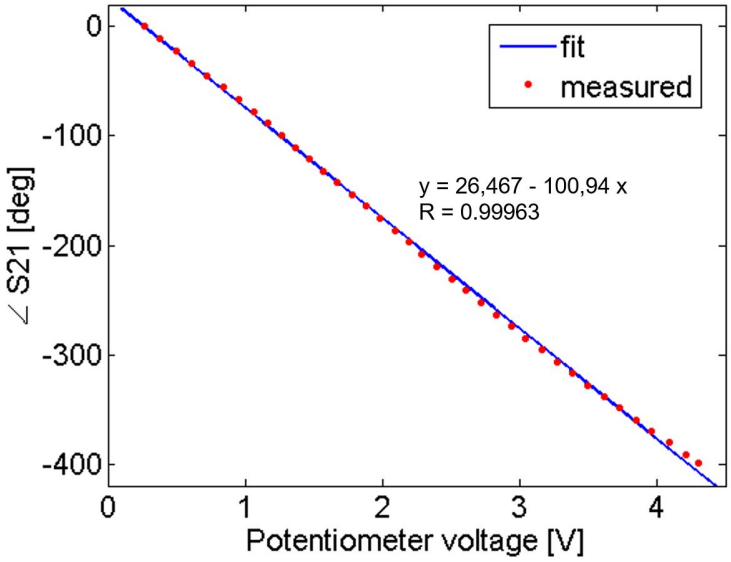

Figure 2.7: S21 phase measurement of the ELI-NP S-band phase-shifter.

used in different electrical devices for his high dielectric strength and excellent arc-quenching capabilities. In Figure 2.1 the SF6 segments are highlighted in magenta. A pressure switch monitors the pressure of the gas into each waveguide section. In case of electric arc or other electrical discharge, the heating produced can lead to SF6 decomposition. Therefore, after a certain amount of

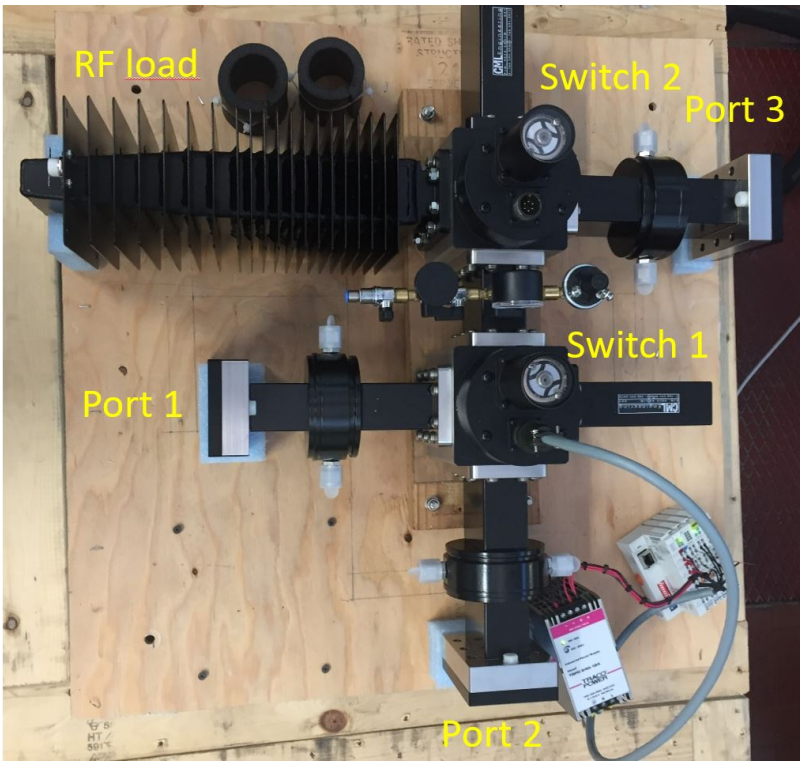

Figure 2.8: Picture of the ELI-NP S-band RF switches mounted in series during the low power measurement.

time, the SF6 can be exhausted and has to be replaced and the used gas recycled.

To separate the Linac vacuum (of the order of 10^{-9} mbar) from the waveguide one, RF ceramic windows have been inserted at each accelerating section input. Also the component under SF6 are isolated through waveguide windows. As mentioned, the last four accelerating structures are fed in couple, splitting the RF signal after the two power sources through a magic T splitter. A phase-shifter is placed after the splitter (see Figure 2.1 or 2.9) to adjust the phase of the signal at the input of the structures.

In Figure 2.9 the entire vacuum system of the power distribution network is represented. The vacuum of the waveguides is maintained at the optimal pressure by means of 70 ion pumps (Agilent 55 l/s) distributed every 4-6 m along the network, which are connected to the waveguides with T pumping units. All the ion pumps are read by the control system and the machine protection system (MPS) through the ion pump controllers arranged in three racks. The MPS

monitoring the ion pump current absorption in case of discharge or leak inside a certain waveguide section can turn of the relative modulator through an hard-wired interlock.

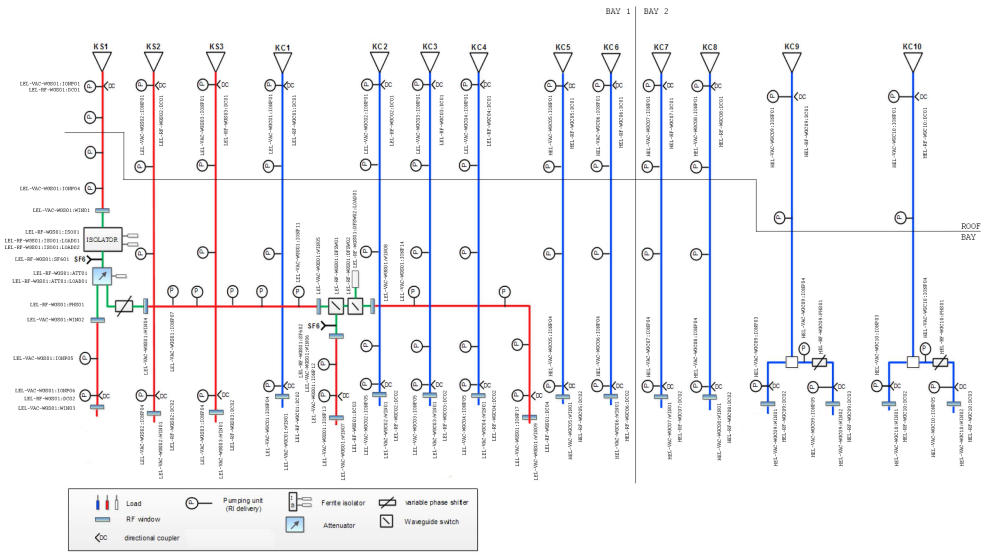

Figure 2.9: Schematic of the vacuum system of the RF power distribution network of the ELI-NP Linac.

Parameter	**Value**
Frequency	2856 MHz
3dB Bandwidth	± 100 MHz
isolation	≥ 23 dB
Insertion loss	≤ 0.3 dB
Max peak power	20 MW
VSWR	1.10
flanges	LIL-type
Internal atmosphere	SF6 @ 2 bar
Water cooling temperature	$30 \pm 1°C$

Table 2.2: Specifications of the S-band ferrite isolator.

2.3 Power sources

An RF Source is generally made up by different subsystems, but normally the main element is the high power microwave amplifier. The microwave amplifier usually used in Linacs is the klystron, that is a linear beam vacuum tube, capable of generating RF pulses with peak power of the order of tens of MW. The other two main elements of the RF source are the power modulator, that fed the klystron with an high voltage (HV) pulse, and the solid state driver amplifier, which amplifies the RF signal coming from the LLRF and provide it at the klystron input.

Klystrons

Klystrons are vacuum electron devices used for the generation and amplification of signals in the microwave frequency range. A schematic representation of this device is reported in Figure 2.10. In a klystron, after being formed in an electron gun (by a thermionic cathode and accelerated towards the anode by an electrostatic field provided by the modulator), the electron beam travels linearly through a certain number of resonant cavities up to a collector. An RF signal, coupled to the first resonant cavity, accelerates and decelerates electrons in the beam (velocity modulation). As the beam drifts, faster electrons catch up with slower electrons and this results in the formation of bunches and an RF current in the beam that grows as the beam moves along. This current is coupled first to intermediate cavities (only one is shown) and then to the output cavity. At each intermediate cavity the RF beam current induces a signal, which produces a field that enhances the bunching process in the beam. Finally, the coupling of the intense RF beam current to the last cavity produces an RF power signal at the output of the device. The gain of a klystron can be very large, 60 dB or more, but the bandwidth is usually limited to a few percent. Output power levels can reach tens of megawatts.

The klystron has to be fed by different subsystems. As mentioned, the cathode of the klystron is fed with an high voltage pulse generated by a pulsed modulator. Generally the anode and the body of the tube are at ground potential, hence

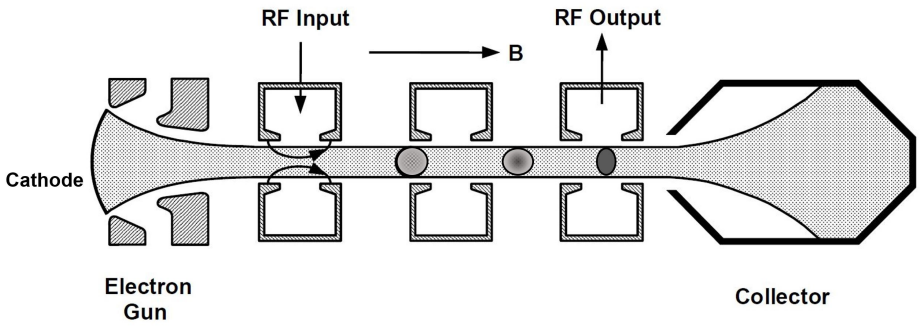

Figure 2.10: Simplified schematic of klystron tube amplifier.

to turn the beam on, the cathode is pulsed negative with high voltage pulses. For this reason the lower part of klystron has to be immersed in transformer oil, that acts as electrical insulation and cooling medium. The filament is heated trough low voltage signal ($\sim 20\,V$) and releases electrons which are accelerated through the klystron tube when the modulator high voltage pulse (300-400 kV) is applied. A solenoid confines the electrons to circular orbits within the klystron tube while they pass from the first klystron cavity, where the RF signal from the LLRF is applied, up past the output cavity where the amplified high power RF is extracted, and finally into the collector where the remaining energy is deposited. Each klystron subsystems need a supply system. The solenoid and the filament are fed by dedicated power supply and vacuum ion pump is used to maintain high vacuum inside the beam tube of the klystron. A more detailed description of the klystron working principles and design can be found in [32].

Pulsed Modulators

In a power system, an essential device is the pulsed modulator. Modulators are electronic devices that convert AC line power into trains of high-voltage high-current pulses needed to drive a load (i.e. klystron), which in turn generate the high power RF waves that accelerate the linac beams.

They find use in a wide variety of applications, in particular, they are used for feeding microwave amplifier tubes used in driving particle accelerator system and microwave generating system for medical radiation-production applications and radar system. The specifications for modulator voltage, current, pulse peak

and average energy, pulse width, flatness, repeatability, etc. vary with the application, but ideally all the required design parameters can be configured from a common set of building blocks.

The majority of these device uses a pulse forming network (PFN) and vacuum tube switch which drive a pulse transformer to reach the required pulse shape and energy. This kind of modulators, called also line type modulators, are commonly used in all the facilities that needs high voltage pulsed signals, in particular for high energy physics. For example the four power sources of the linac injector of the DaΦne ring at INFN-LNF laboratories implement this kind of modulator [33, 34]. A PFN is a network composed of inductors and capacitors connected together as shown in Figure 2.11. The PFN is connected to the primary winding of a step-up transformer through an high voltage switch. Gas-filled tube switches (thyratrons) are commonly used because they can handle very high currents and voltages. The energy previously stored in the PFN, through a power supply, is delivered to a step-up transformer which drives the klystron cathode. The PFN has the purpose of feeding the load with a rectangular shape pulse, in particular the length and the ”good” rectangular profile of the pulse are determined directly by the number of cells (L-C) of the network. Moreover, adjusting capacitance and/or inductance of certain cells is possible to compensate the overshooting inherent in this type of network. The PFN needs to be matched to the load impedance and it must be capable of store the entire pulse energy because for each pulse of the modulator it has to be completely discharged and charged again in order to form the new pulse. For this reason, operating at high repetition rate, the capacitors of the PFN have to withstand voltages of the order of tens of kV and hence have to be quite large. This of course have a direct impact on the overall dimensions and cost of the system.

The commonly used gas-filled tube switches are hydrogen thyratron tubes. These are hot-cathode vacuum tubes filled with hydrogen characterized by a limited life due to the depletion of the hot cathode. Hence, they have to be periodically replaced.

These kind of systems based on PFN/thyratron have been employed for the last 50 years and are commonly used even nowadays in a lot of facilities. Nevertheless, thanks to improvements in solid state switches in terms of speed and

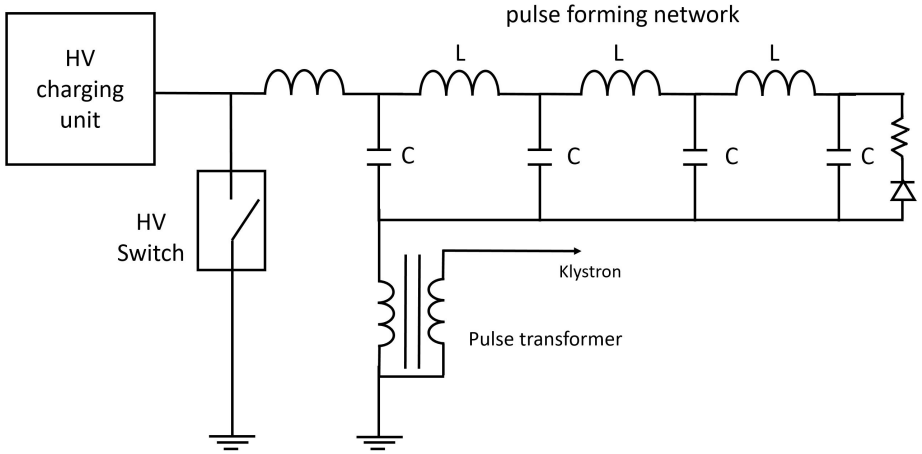

Figure 2.11: Simplified schematic of a pulse forming network connected to a pulse transformer through a switch.

sustained peak power a new generation of pulse modulators, called solid state pulse modulators, has become popular in the past years [35, 36, 37]. Single solid state switches generally don't have the peak voltage rating required for most accelerator applications and, consequently, different topologies using more solid state devices connected at the same time has been studied and implemented in real modulator [38]. A simplified schematic of a solid state pulsed modulator is represented in Figure 2.12, in which is possible to distinguish three main subsystem: the capacitor charging power supply, the switching units with the capacitors and the pulse transformer.

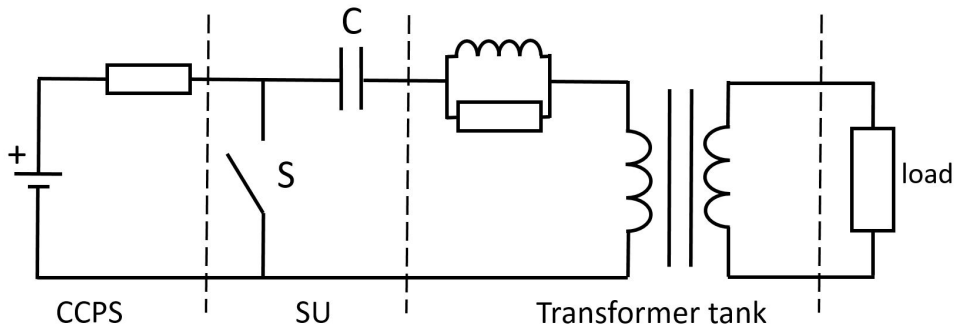

Figure 2.12: Simplified schematic of a solid state pulsed modulator with a single switching unit.

In this simplified scheme the power supply keep charged the capacitor C at relatively low voltage ($\approx 1 - 5\,kV$), when the switch S receives a trigger signal from the control system, it closes the circuit and part of the charge stored in it flows towards the primary winding of the step up pulse transformer. When the switch is opened, a rectangular pulse is generated on the secondary winding of the transformer. The L-R circuit in series to the capacitor acts as a tuning circuit to avoid the capacitance voltage drop while the switch is closed. In this way the pulse is compensated to reach the flat top requirements. The solid state switches can be turned on and off electronically through low power pulses, transferring charges towards the transformer for a specified time controlled by this trigger signal. In this way the length of the output pulse is easily controlled by the trigger pulse.

As mentioned before, using only one solid state switch it is not possible to satisfy the requirements of an high power system, for this reason in the actual systems more switching units are used in parallel. The switching elements mostly used are Insulated Gate Bipolar Transistor (IGBT) that can withstand current higher than 500 A and voltage higher than 1 kV. There are different models of IGBT switch that can be used depending on the maximum sustainable voltage and current. The choice of the IGBT model affects directly the topology of the solid state modulator, the number of switch, the pulse transformer design etc. A schematic of the solid state pulsed modulator architecture with different switching units used in parallel is shown in Figure 2.13.

The pulse transformer configuration used in this scheme is the fractional turn transformer with a one turn secondary. The primary winding of the pulse transformer is made up by multiple primaries in parallel, each connected to one or more switching units containing the capacitors. By closing the switches with the trigger signal, the capacitors starts to discharge generating a current on each primary winding. All the fluxes of the magnetic field generated by the primary currents sum up inductively and generate a single high voltage pulse on the secondary winding of the pulse transformer. Then the secondary winding is directly connected to the klystron providing him the high voltage pulse.

There is a substantial difference, in the way the line type modulator and the solid state one, handle the charge stored in the capacitors. In line type modulator

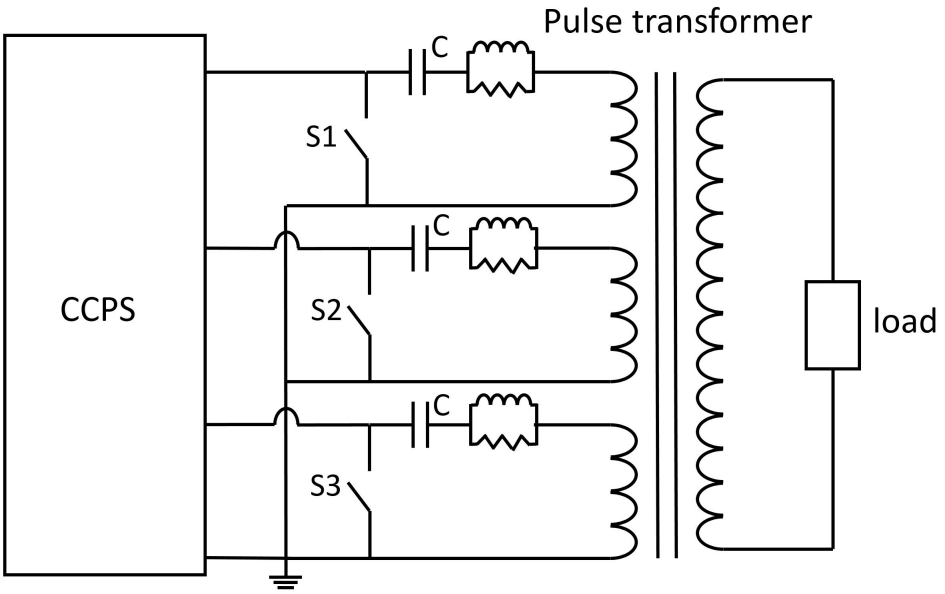

Figure 2.13: Simplified schematic of the solid state pulsed modulator with different switching units in parallel linked to the primary winding of the pulse transformer.

the high voltage capacitors of the PFN are charged to the maximum voltage (tens of kV) and discharged completely for each output pulse, while for the solid state modulator the capacitors are always at an almost constant voltage ($\sim 1\,kV$) and when the IGBT switch are turned on, closing the circuit, only about the 10% of their stored charge is used to generate the output pulse. This is because a large number of capacitors and switches are used in parallel and the voltage is distributed between them. The charge lost during the generation of the pulse is completely restored by the power supply prior to the next pulse. There are different schemes to realize a solid state modulator depending on the number and on the model of switches used. In the next section the solid state modulators used in the ELI-NP Linac are described.

ELI-NP RF Sources

The Linac beam energy is correlated with RF amplitude fluctuations and in order to minimize the bunch by bunch energy spread, the RF accelerating field fed into the different accelerating structures has to be, in principle perfectly flat

and stable. Therefore there are two important requirements for the RF sources: the pulse to pulse amplitude stability ($< \pm 0.005\%$), and the RF pulse uniformity (pulse flatness $< \pm 1\%$). In table 2.3 the main requirements for the 3 types of RF sources are reported.

Parameter	**Sb 45MW**	**Sb 60MW**	**Cb 50MW**
Modulator model	K 2-3	K 2-3	K 2-2
Number	1	2	10
RF Frequency [MHz]	2856	2856	5712
RF Peak Power [MW]	45	60	50
RF Average Power [kW]	15	15	5
RF drive Power [W]	300	400	300
Operational voltage range [kV]	$0 \div 340$	$0 \div 380$	$0 \div 350$
Operational current range [A]	$0 \div 360$	$0 \div 430$	$0 \div 317$
Modulator Peak power [MW]	122	163	111
Modulator Avg Power [kW]	49	65	32
Max rep. rate [Hz]	100	100	100
Pulse length (top) [μs]	2.5	2.5	1
Top flatness (dV) [%]	$\leq \pm 1$	$\leq \pm 1$	$\leq \pm 0.5$
Rate of Rise [$kV/\mu s$]	$250 \div 350$	$250 \div 350$	$250 \div 350$
Amplitude stability [%]	$\leq \pm 0.005$	$\leq \pm 0.005$	$\leq \pm 0.005$
Pulse to pulse time jitter [ns]	$\leq \pm 4$	$\leq \pm 4$	$\leq \pm 4$
Pulse width time jitter [ns]	$\leq \pm 8$	$\leq \pm 8$	$\leq \pm 8$

Table 2.3: Main parameters specifications of the 45 MW S-band, 60 MW S-band and 50 MW C-band power sources used for the ELI-NP Linac.

These power sources are composed by three main devices: the modulator made by Scandinova [39], the klystron made by Toshiba [40] and the RF driver amplifier made by Microwave amplifiers [41].

The modulator can be seen as a unique ensemble comprehending different subsystems and devices. Both the RF driver amplifier and the klystron with solenoid and his accessory systems are integrated into the modulator. The klystron is inserted in the oil tank near the pulse transformer, while the RF amplifier output is directly connected to the klystron input cell. The filament power supply (FPS), the solenoid power supply (SPS) and the ion pump controller are also integrated in the modulator front rack. In Figure 2.14 the 3D model of the

K2-2 Scandinova modulator is reported.

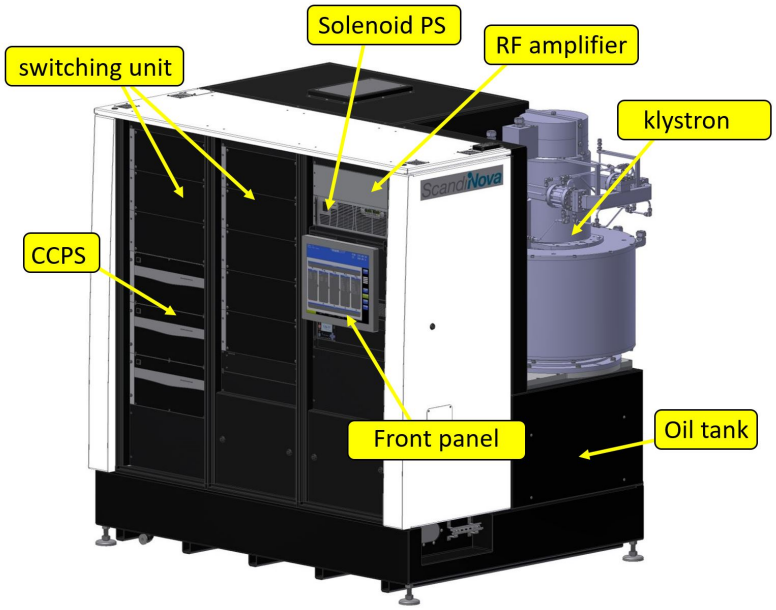

Figure 2.14: 3D model of the Scandinova solid state pulsed modulator (K2-2 model) with 50MW Toshiba klystron.

The Scandinova modulator is in solid state technology, and uses several (up to 72) 1.2kV IGBT switches in parallel to generate the high voltage pulse on the secondary winding of the transformer. The entire schematic with all the subsystems of the modulator is reported in Figure 2.15, where is possible to recognize the system topology described in the previous section composed by the capacitive voltage power supplies (CCPS), the switching units (SU) (which contain the IGBT switches and the capacitor banks) and the pulse transformer. In this configuration the number of SU determines the peak power of the modulator while the number of CCPS determines the its average output power. Therefore the 60MW S-band modulator has 4 CCPS units and 12 SU, while the 50MW C-band modulator consists of 3 CCPS units and 8 SU. The pulse to pulse stability of the system mainly depends by the stability of the power supply, which has to charge the capacitor at the same voltage after each pulse.

In the schematic reported in 2.15 it can be distinguished the power distribution unit, the cooling system and the control system. The power distribution unit feeds all the subsystems included in the modulator with the 3-phase and

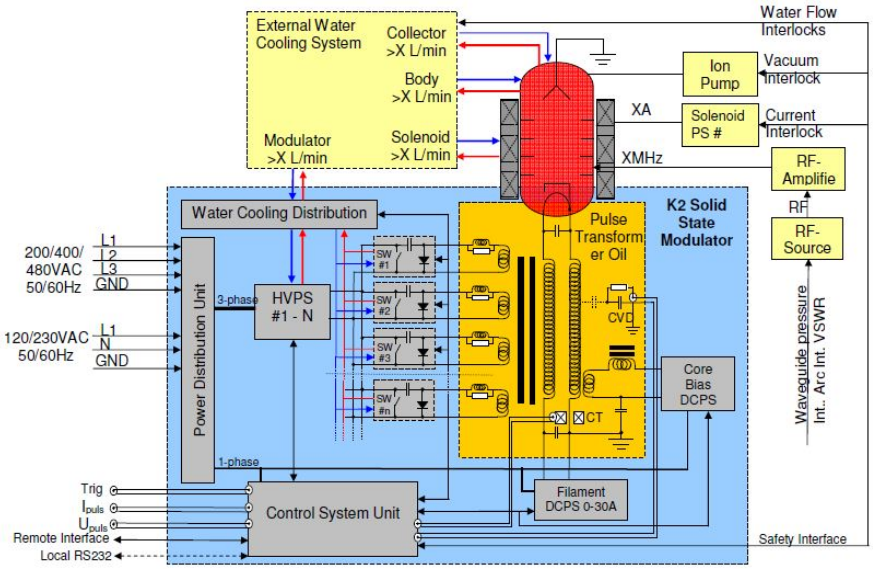

Figure 2.15: Schematic of the solid state pulsed modulator (courtesy of Scandinova).

single phase AC power. The cooling system monitors and distribute cooling water to the CCPS, the SU and the transformer tank. It also includes four circuits for different parts of the klystron: the collector, the body, the solenoid and the RF ceramic window. The control system monitors the signal coming from all the modulator subsystems and handles the trigger and interlock signals for the different sub-units. It consists in a PLC controller connected to an FPGA that handles the hardwired interlocks. The correct operation of the overall system has to be constantly monitored in order to prevent damage of the system itself or danger for the user. For this reason both software interlock than hardwired interlock are implemented. Some of the most critical interlocks are on the filament current and voltage, ion pump current absorption, solenoid current, water cooling flows, over current on the IGBT switches, oil temperature, over current at the pulse transformer output etc. Moreover the system presents interfaces for external interlock signals generated by the ELI-NP-GBS Machine Protection System that can turn off the modulator. All the hardwired interlock signals of the modulator have a reaction time $< 10\,ms$, hence is possible to turn off the modulator output pulse before a second pulse is generated.

All the ELI-NP sources realized until now has been tested in factory in order

to verify their reliability and their conformity to the requirements (reported in tables 2.3). Ten power sources have been successfully tested: 3 S-band and 7 C-band. These test have been conducted in the Scandinova factory in Uppsala (Sweden). The general set-up used during the Factory Acceptance Tests (FAT) is represented in Figure 2.16.

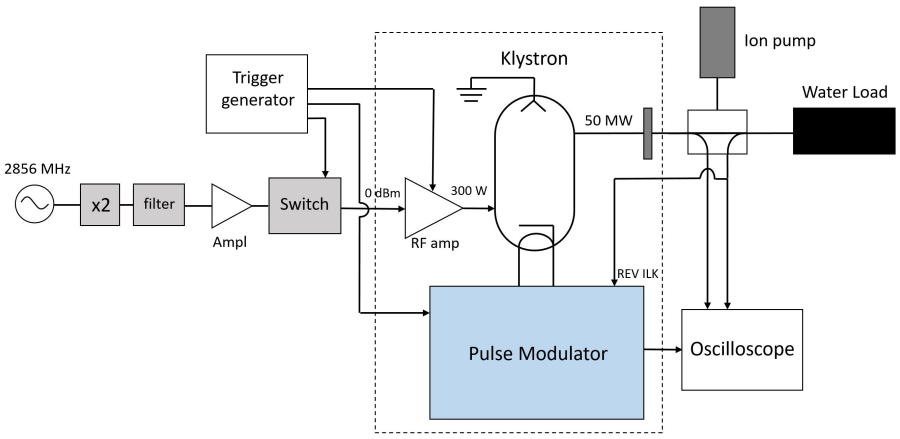

Figure 2.16: Schematic of the set-up used for the C-band power source factory acceptance test.

It is composed by the following elements:

- A digital delay pulse generator, which was used to generate the three signals that enable the RF driver amplifier and trigger the modulator and the RF switch at 100 Hz;
- a LLRF signal generation system (signal generator, frequency multiplier, filter, amplifier and switch);
- the device under test, i.e. the power source, composed by the pulsed modulator, the klystron and the RF driver amplifier;
- a directional coupler connected at the output of the klystron;
- an ion pump for the waveguide system;
- a water cooled RF dummy load;
- an oscilloscope.

The output of the klystron was connected to an RF load through a directional coupler and a small waveguide network comprehending an ion pump. In order to drive the RF amplifier with the LLRF signal a simple set-up has been realized. It consist in a 3 GHz signal generator feeding in order a $\times 2$ frequency multiplier, a filter and an amplifier connected to an RF switch driven by a 100Hz trigger signal. In Figure 2.17 is possible to see a picture of this set-up taken during one of the C-band FAT.

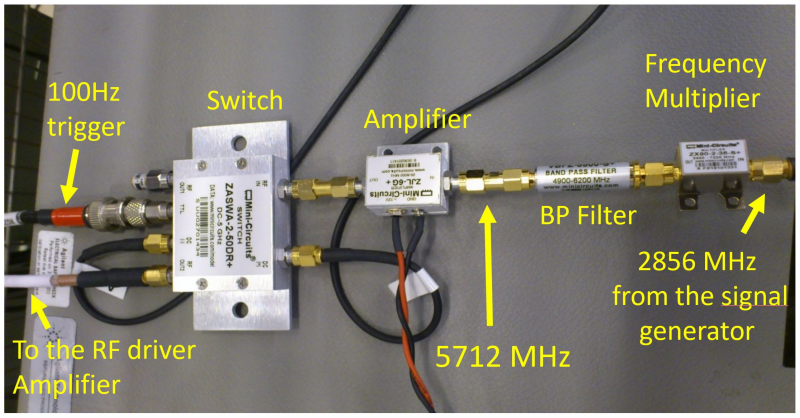

Figure 2.17: Picture of the LLRF signal generation set-up used during the C-band power sourced FAT.

In the S-band case, the 3 GHz generator was directly connected to the RF switch. In Figures 2.18 are reported two pictures taken during the factory acceptance test. Before each test the klystron and the waveguide network have been conditioned monitoring the current absorption of the two ion pumps. A chiller was used for the cooling of the RF load.

The FAT protocol starts with a complete characterization of the output HV pulses generated by the modulator at full power. The klystron in this initial phase was run in ”diode” mode, hence without RF signal at his input. In this working mode there is no bunching of the klystron particle beam and all his energy is dissipated on the collector. Current and voltage of the HV pulse generated by the modulator were measured through a current transformer (CT) and a voltage divider (CVD) present inside the transformer tank just before the connection to the klystron cathode. The output signals of these device is available with two BNC connector at the front panel of the modulator and were read by an oscil-

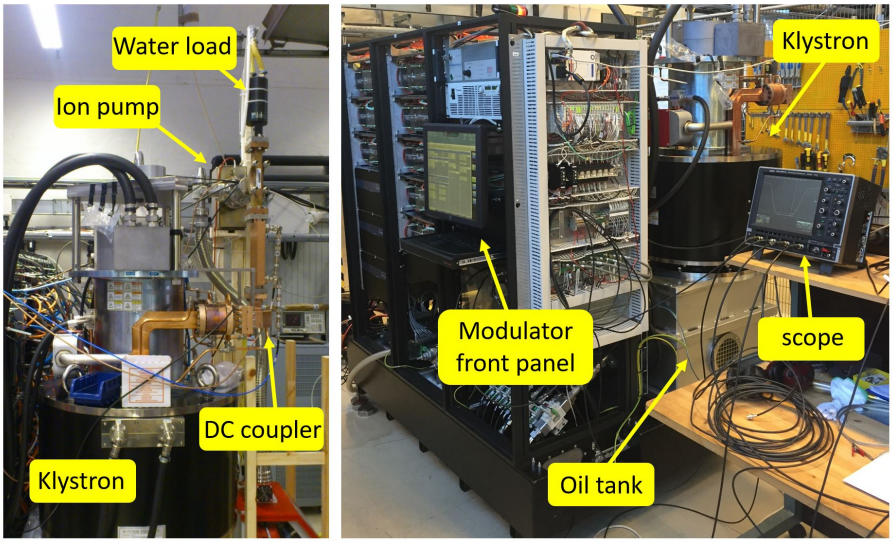

Figure 2.18: Pictures of the FAT setup of a C-band RF power source.

loscope. By scaling the measured signals through the transform ratios of the CVD and the CT has been possible to obtain the correct values. Multiplying together the measured values of current and voltage with the klystron efficiency $(35 - 40\%)$ is possible to evaluate the power feeding the klystron. Moreover to verify the compliance of the system with the requirements the pulse to pulse amplitude stability, the pulse top flatness, rise and fall time were measured through the oscilloscope.

By switching on the LLRF signal we measured also the high power RF pulse. Forward and reverse signals at the klystron output were available at the pick-ups of a directional coupler. The signals at the pick-ups were attenuated and sampled through peak diode detectors and the envelope of the signals were read thanks to an oscilloscope. To check the validity of the measurements the power of the reverse and forward signal was measured also with a power meter. In Figures 2.19 and 2.20 signals measured during the FAT of a 60MW S-band power source and of a 50MW C-band power source are reported.

The ratio between forward and reflected RF pulses, shown in the plot, is determined by the dummy load Return loss. In the real case, being the load of the klystron a traveling wave accelerating section, this ratio will be higher (>25 dB). The reflected signal was split at the directional coupler pick-up and

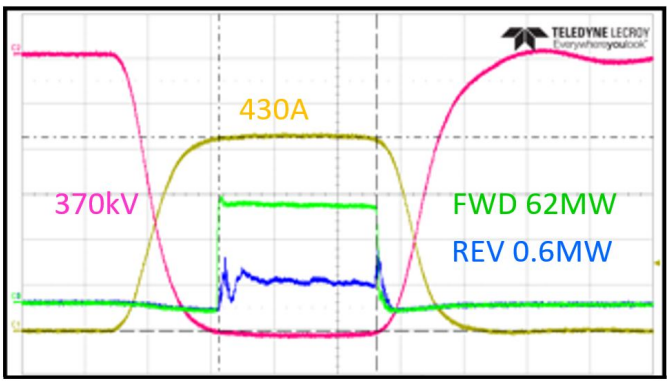

Figure 2.19: Signals of a 60MW S-band power source measured during the factory acceptance test: modulator output pulse voltage (magenta) and current (yellow), forward (green) and reverse (blue) RF signals at the klystron output.

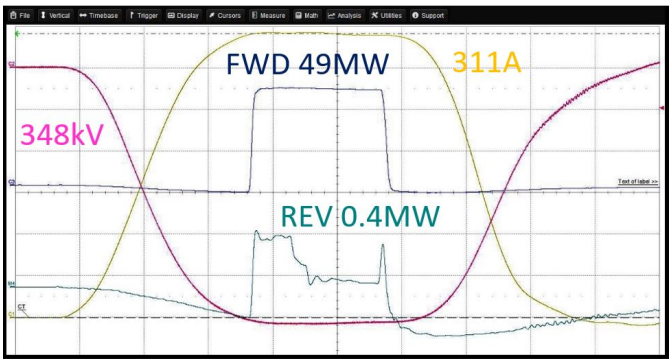

Figure 2.20: Signals of a 50MW C-band power source measured during the factory acceptance test: modulator output pulse voltage (magenta) and current (yellow), forward (blue) and reverse (green) RF signals at the klystron output.

was sent with the correct attenuation to a digitizer embedded in the modulator. This digitizer interlocks the modulator to protect the klystron when the reflected power exceeds a pre-set threshold. In our case the modulator was interlocked if the reverse power level overcome the 20% of the forward power level (for the Toshiba klystrons, $VSWR_{max} = 1.5 : 1$, which gives a voltage reflection coefficient of $\Gamma = (VSWR - 1)/(VSWR + 1) = 0.2$). The results of the measurements taken during the FAT of the S-band RF sources are reported in table 2.4, while the results obtained for the C-band modulators tested up to now are reported in tables 2.5 and 2.6.

After the pulses characterization a long run test of more than 5 hours at full

Parameter	Unit	MSB1	MSB2	MSB3
Output Pulse Voltage	kV	345	375	370
Output Pulse Current	A	371	430	410
Modulator Average Power	kW	51	69	60.8
Beam Peak Power	MW	128	161	152
Pulse top flatness	%	0.47	0.58	1.6
Pulse repetition freq.	Hz	100	100	100
Pulse length (top)	μs	2.5	2.5	2.5
Pulse length (FWHM)	μs	4	4.3	4
Pulse to pulse stability	%	0.0022	0.004	0.0057
Rate of rise	$kV/\mu s$	423	442	260
Rate of fall (top)	$kV/\mu s$	405	379	189
Klystron filament DC current	A	30.2	31.3	30.28
Klystron filament DC voltage	V	11.8	11.7	12.5

Table 2.4: Results of the measurement performed during the FAT of the ELI-NP S-band modulators.

Parameter	Unit	MCB1	MCB2	MCB3
Output Pulse Voltage	kV	348	362	347.4
Output Pulse Current	A	311	327	323
Modulator Average Power	kW	30	35.5	30.2
Beam Peak Power	MW	108	118	112
Pulse top flatness	%	0.86	0.84	0.73
Pulse repetition freq.	Hz	100	100	100
Pulse length (top)	μs	1	1	1
Pulse length (FWHM)	μs	2.9	3	2.9
Pulse to pulse stability	%	0.004	0.0067	0.004
Rate of rise	$kV/\mu s$	380	395	414
Rate of fall (top)	$kV/\mu s$	278	331	362
Klystron filament DC current	A	19.5	18.2	18
Klystron filament DC voltage	V	18.3	15.8	15.5

Table 2.5: Results of the measurement performed during the FAT of the ELI-NP C-band modulators 1-3.

power has been performed. During this test the output modulator pulse (voltage and current), the RF pulse and all the main parameters of the system were

Parameter	Unit	MCB4	MCB5	MCB6	MCB7
Output Pulse Voltage	kV	360	346	366	358
Output Pulse Current	A	324	320	325	325
Modulator Average Power	kW	30	33.2	35.6	34.9
Beam Peak Power	MW	116	110.9	119	116
Pulse top flatness	%	0.74	0.58	0.9	0.58
Pulse repetition freq.	Hz	100	100	100	100
Pulse length (top)	μs	1	1	1	1
Pulse length (FWHM)	μs	2.9	3	3	3
Pulse to pulse stability	%	0.0033	0.006	0.0033	0.0076
Rate of rise	$kV/\mu s$	431	421	385	408
Rate of fall (top)	$kV/\mu s$	366	386	310	390
Klystron filament DC current	A	19.5	19	19.5	19.1
Klystron filament DC voltage	V	17.3	17.3	18.1	17.3

Table 2.6: Results of the measurement performed during the FAT of the ELI-NP C-band modulators 4-7.

continuously monitored. During the long run test, radiation measurements have been performed all around the klystron at a distance of 1 m and and a height of 1 m and 1.5 m from the ground with a Fluke ion chamber 451-P. As example, in table 2.7 the results for a 50 MW C-band klystron are shown.

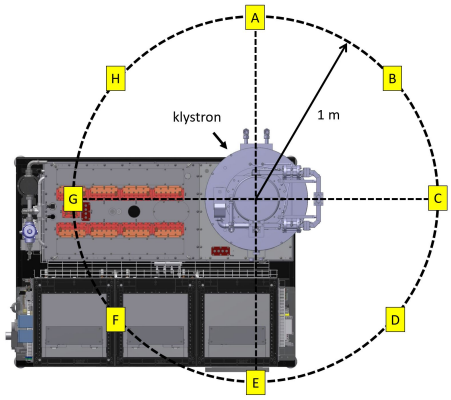

Figure 2.21: Radiation measurements positions around the 50 MW C-band klystron.

The FAT was concluded with the test of the main interlocks of the modulator and of its subs-system. All the systems tested up to now has been successfully

Pos.	0.5 m from floor		1.5 m from floor	
	diode mode μSv/h	**RF mode** μSv/h	**diode mode** μSv/h	**RF mode** μSv/h
A	0.6	0.9	0.2	0.3
B	0.2	0.2	0.1	0.2
C	1.2	1.0	0.2	0.3
D	0.5	0.5	0.2	0.3
E	0.1	0.3	0.2	0.1
F	0.1	0.2	0.1	0.1
G	0.1	0.2	0.2	0.2
H	0.3	0.3	0.2	0.2

Table 2.7: Radiation measurement performed at different position around a 50MW C-band Toshiba klystron (according to Figure 2.21)

characterized and no critical faults have been detected during all the test performed.

2.4 Low level RF

The last subsystem that compose the RF system of the ELI-NP Linac is the low level radiofrequency (LLRF) system. The aim of any LLRF system is twofold: it generates the RF pulses used to drive the power units, and it acquires and monitors the RF signals picked-up along the accelerator (e.g. from the waveguide network, the accelerating sections or inside the RF cavities). Moreover, it must allows to generate suitable control signals, either manually or automatically through feedback loop, to set the required levels and phases of the RF fields in any RF device of the machine.

The ELI-NP LLRF system, "Libera LLRF" manufactured by Instrumentation Technologies [42], consists of 13 temperature stabilized digital boards (one for each power unit): 3 S-band and 10 C-band. This choice has been made in order to guarantee the maximum flexibility in terms of pulse shaping and machine operation stability. In Figure 2.22 is reported one of the Libera LLRF board.

One of the main advantages of a digital LLRF system is, in fact, the possibility to perform a pulse-by-pulse feedback interactively choosing from control

Figure 2.22: Libera LLRF digital board manufactured by Instrumentation technology.

system the target signals for amplitude and phase loops. Moreover, the pulse shape can be arbitrarily chosen (e.g. for beam loading compensation, as it will be shown in section 3.6) simply loading a spreadsheet to Libera FPGA.

The request for thermal stabilization has been introduced to compensate the long-term effect of temperature drifts, that must not exceed 100 fs for normal operation: $(24 \pm 2)^{\circ}C$.

Each board contains four main elements:

1. an analog front-end with 8 RF inputs per module (a board can host up to 4 modules);
2. an analog back-end (with 1 RF output from vector modulator - I/Q);
3. the main CPU (which hosts the sampling cards, the FPGA and the EPICS control system server);
4. the Local Oscillator generator and timing unit (with 1 input for the RF reference, 1 input for the trigger of FPGA, DAC and ADC and the interlock I/O).

The main parameters of Libera LLRF boards have been summarized in Table 2.8. Each board monitoring the TW structures will acquire 6 RF signals (solid state amplifier output, klystron output and section output forward and reflected power), with the exception of the last four sections that will be squeezed in two boards equipped with two sampling modules each, in order to manage 12 RF signals. All the signals from the SW cavities, instead, will be acquired by the first S-band board. In this case also three RF probes will be acquired to monitor the electric fields in the cavities, for a total of 13 RF signals.

Parameter	**Value**
Resolution	Amplitude: 0.1%
	Phase adder jitter: $< 10 fs\%$
Long term stability	100 fs at $T = (24 \pm 2)^{\circ}C$
Analog front-end	BW: $5\,MHz\%$
	Max RF level: $20\,dBm$
Analog back-end	BW: $16\,MHz\%$
	Max RF level: $13\,dBm$
LO gen. and timing	Min RF ref. level: $15\,dBm$
	Sampl. clock: $119\,MHz$, 16 bit
	IF: $44.625\,MHz$

Table 2.8: Libera LLRF main specifications.

CHAPTER

3 C-Band Accelerating Structures

Content

3.1 Introduction

The ELI-NP linac booster consists of twelve 1.8 m long TW C-Band disk loaded accelerating structures, each one is a quasi-Constant Gradient (CG) structure with $2\pi/3$ phase advance per cell and will operate at an average accelerating gradient of 33 MV/m with 40 MW of input power. Because of the multi-bunch operation, the structures have been designed with a damping system to avoid beam break-up (BBU) instabilities. Moreover since the average dissipated power in the structure at full power is 2.3 kW, the cooling system has been integrated into the structure itself and it has been dimensioned in order to avoid structure detuning under RF powering. The main electron beam and C-band cavity parameters of the ELI-NP Gamma Beam System (GBS) are given in Table 3.1.

Parameter	**Value**
Working frequency [MHz]	5712
Number of cells	102 + 2 couplers
Structure length [m]	1.8
Working mode	TM_{01}-like
Iris half aperture radius [mm]	6.8 - 5.78
Cell phase advance	$2\pi/3$
RF input power [MW]	40
Average accelerating field [MV/m]	33
Average quality factor	8860
Shunt impedance [$M\Omega/m$]	67 - 74
Group velocity (v_g/c)	0.025-0.015
Filling time [ns]	313
Output power	$0.29 \cdot P_{in}$
Repetition rate [Hz]	100
Pulsed heating for $512\,ns$ pulse length [$^{\circ}C$]	< 21
Working temperature [$^{\circ}C$]	30

Table 3.1: ELI-NP C-band accelerating structures main parameters.

The design criteria and the realization of these structures are described in the following sections. A detailed descriptions of this structure can be found also in [43, 44, 45]. In particular the tuning procedure, the low and the high power tests are discussed in detail in the following sections. The results of these tests

for all the ELI-NP structures realized until now are reported together with the calculations for a possible beam loading compensation scheme.

3.2 Design

The electromagnetic design of this structure followed the main criteria that have been adopted for the SPARC C-band sections [46, 47]. In particular the dimensions of each cell has been optimized to obtain:

- the lowest peak surface electric field on the irises;
- an average accelerating field of 33 MV/m with 40 MW input power;
- the largest iris aperture compatible with the previous points to increase the pumping speed of the structure, to reduce the dipole wakefield intensity and the filling time of the structure.

The low filling time allows to have short RF pulse reducing the breakdown rate probability. Each cell had four tuners and eight cooling pipes to sustain the 100 Hz repetition rate operation. A detailed thermal analysis has been done to demonstrate the possibility to operate at 100 Hz repetition rate [48]. The input and output couplers have been designed with a symmetric feeding and rounded edges to reduce the pulsed heating on their surfaces. Moreover, they had a race-track shape to completely suppress the quadrupole field components induced by the presence of the waveguide hole apertures. The same criteria will be discussed in detail in Chapter 5 for the design of a TW structure prototype.

The aperture of the irises have been shaped to have a quasi-constant accelerating field from 38 to 28 MV/m (see Figure 3.9(right)). It has been decided to adopt such a design with respect to a constant impedance structure because, in this last case, to have an average accelerating field of 33 MV/m, the field in the first cells has to be increased of more than 44 MV/m giving potential problems from the breakdown rate point of view. On the other hand a perfect constant gradient structure would require very small irises at the end of the structure with a consequent increase of the dipole mode R/Q, reduction of the pumping speed and beam clearance.

HOM damping system

Each devices which introduce discontinuities in the beam pipe, as an accelerating structure, is source of radiated wakefields after the passage of the beam. These radiated fields can lead several consequences: excitations of high order modes (HOMs) in resonant structures, new configuration of the self field, propagation of electromagnetic fields at frequencies above the cut-off of the beam pipe etc [49]. These fields can have longitudinal and transverse components and can interact with the beam affecting the beam dynamics. In particular for a linac which operates in multi-bunch mode, like the ELI-NP Linac, the long range wakefields represent a source of instability for the particle beam. The longitudinal wakefield are related to the excitation of the fundamental accelerating mode of an accelerating structure and can lead to the so called beam loading (BL) effects, i.e. a modulation of the beam energy along the train of bunches. A possible scheme for beam loading compensation is discussed in 3.6. The transverse wakefield interacting with subsequent bunches, can drive an instability along the train called multibunch beam break-up (BBU) that can lead to the complete loss of the beam. Due to tight requirements on the narrow bandwidth of the gamma ray photon beam, which in turns asks for very low transverse emittance, we must carefully evaluate the emittance degradation due to long range transverse wakefield, and minimize as much as possible its dilution. For this reasons the ELI-NP C-band structure have been designed with an effective damping system of the HOM dipole modes. Several possible schemes for dipole mode damping can be found in literature [50]. The solution implemented in this structure is similar to the one adopted for the CLIC structures at CERN [51]. Each cell of the structure has four waveguides that allows the excited HOMs to propagate and dissipate into silicon-carbide (SiC, Ekasic-P) RF loads (see Figure 3.1). To reduce the fabrication costs, the geometry of the SiC absorbers has been strongly simplified. A detailed analysis of the HOM damping inside these structures can be found in [43, 45].

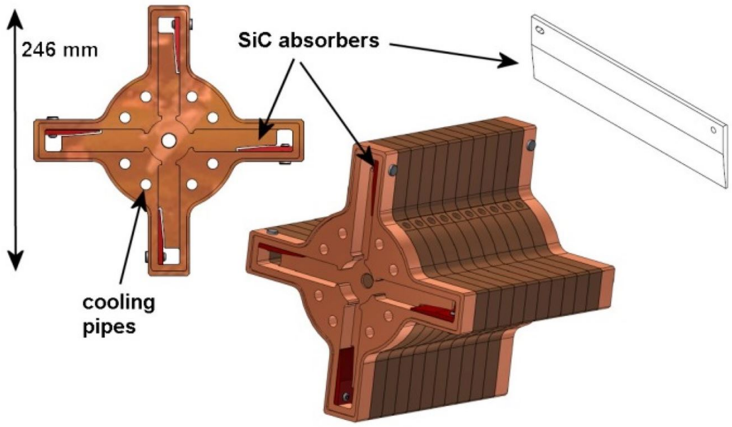

Figure 3.1: Final mechanical drawing of the ELI-NP C-band single cell with the SiC absorbers and of the 12 cell module.

3.3 Realization

Each C-band structure is divided in 10 modules: the input and output coupler ones (with the two adjacent cells) and eight modules, each one consisting of 12 cells. All modules are fabricated, brazed and tested separately and then brazed all together. The fabrication of all components has been done by Comeb [52]. In particular the manufacturing of the cells required several steps described in detail in [53]. The cells are at first machined roughly by lathe then are subjected to a stress relieving treatment in a vacuum furnace and to a final precise machining with a milling machine and a ultra precise lathe. The manufacturing of the input and output couplers followed a similar procedure. Pictures of a machined cell and of the input output coupler are given in Figure 3.2.

Before the brazing procedure all the components have been cleaned with weak acid (citric) and neutral soaps in an ultrasound bath. The modules of 12 cells have been brazed at $850°C$. The SiC (Ekasic-P) absorbers have then been inserted in the cells and fixed with special screws. The last brazing steps have been performed in the INFN-LNL Legnaro laboratories where a large vacuum furnace is available. Two brazing steps were necessary because the full length of the vacuum furnace at LNL can be achieved with an extension not heated.

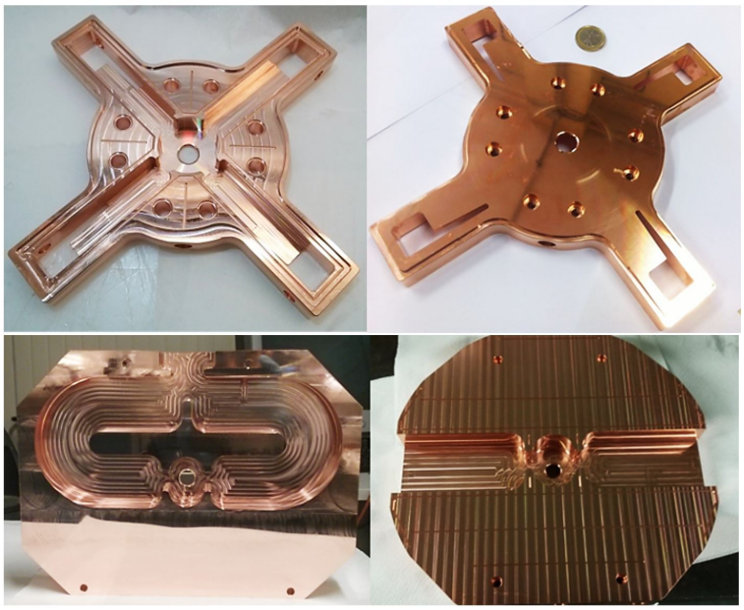

Figure 3.2: Picture of the machined cell and of the input and output couplers.

The first sub-assembly was composed of six modules plus the output coupler while the second one was made up of the remaining two modules with the input coupler. In the last oven cycle the two sub-assemblies have been joined at $780°C$. The picture of of the two half structures before brazing and the full assembled structure in the INFN-LNL oven is given in Figure 3.3.

Figure 3.3: Picture of the INFN-LNF vacuum oven before and after the final brazing of the ELI-NP C-band structure.

3.4 Tuning and Low power measurements

The machining technology used to realized accelerating structures components has a limited precision in producing identical cells. Very high precisions in the cell manufacture is needed but it is not economical and can give a strong increase in the cost of the structure. Working at 5.712 GHz in a $2\pi/3$ travelling wave structure, $10\,\mu$m error in the single cell radius dimension cause a frequency shift of 3 MHz and so a phase advance error of more than 2 degrees which, if not compensated, can lead to degradation of the structure performances [45, 46]. Moreover, during the brazing process the structure is subjected to high thermal stresses that can lead to further modification of the cells inner dimensions. Therefore, in general, tuning procedure is necessary to have the right phase advance between adjacent cells, and minimize the reflection from the detuned cells. This allows to avoid standing wave in the structure, which will introduce local field enhancement and may limit the overall accelerating gradient.

To tune the different ELI-NP C-band structures an automatic measurement system has been developed. This system integrate the use of the ”bead-pull” measurement, based on the non resonant perturbation technique developed by Steele [54], and the tuning algorithm described in [55, 56] that has been already used for the SPARC C-band structure. In the next subsections the “bead-pull” measurement and the tuning method are described and then the results of the ELI-NP C-band structures tuning is reported.

Bead-pull measurement

The set up measurement to perform the bead-pull, was composed by the following elements:

1. Vector network analyzer R&S ZVB 20;

2. PC interfaced with the VNA through bus GPIB (General Purpose Interface Bus) connected to the motor controller;

3. step motor controller IPSES;

4. perturbing bead, which is a spherical lead object, glued on a nylon wire;

5. a weight to stretch the nylon wire;

6. Labview virtual instrument (VI) which allows to control the motor and to automatically acquire the signals from the VNA.

In Figures 3.4 and 3.4 a sketch and a picture of the bead-pull experimental setup in the INFN-LNF clean room are showed:

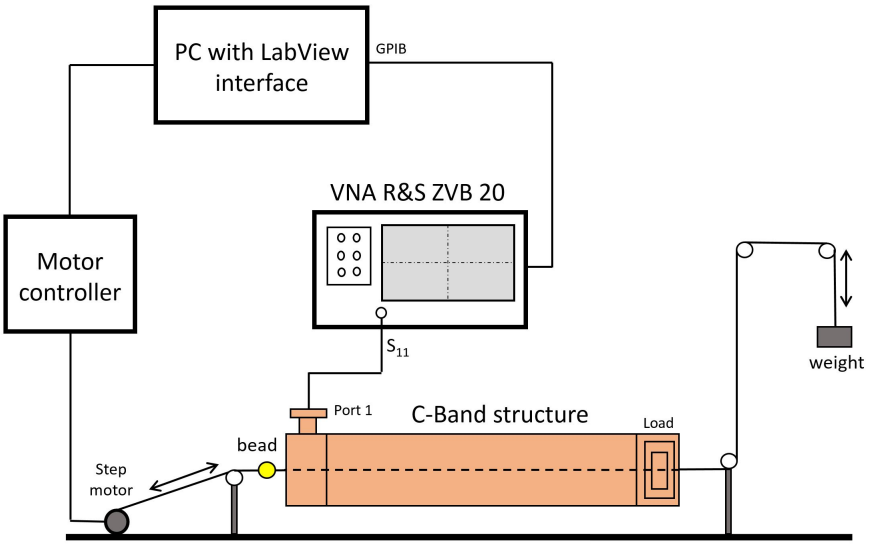

Figure 3.4: Schematic diagram of the bead-pull measurement set-up.

In the bead-pull technique a small object is inserted on the beam axis of a travelling wave structure. It interacts with the stored electromagnetic field which results in a modification of the reflection coefficient measured at the input of the structure. On the axis of the structure the component of the magnetic field is zero and the effect of the bead can be described by the formula:

$$2P_{in} \cdot (\Gamma_p - \Gamma_u) = -j\omega k_{steele} \cdot |E_z|^2 \tag{3.1}$$

where P_{in} is the average power entering the electromagnetic structure, Γ_p and Γ_u are the perturbed and unperturbed reflection coefficients, k_{steele} is a constant (which depends on the bead electric parameters and geometry) and E_z is the

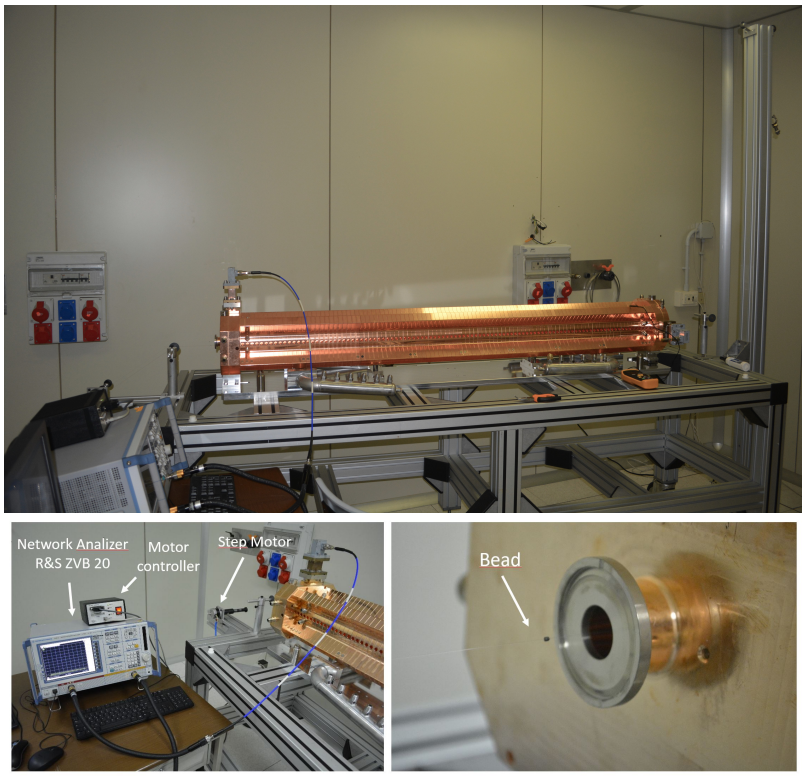

Figure 3.5: Pictures of the bead-pull measurement set-up used for the ELI-NP C-band structures.

electric field at the bead position and at angular frequency ω. With this method is possible to measure the electric field amplitude and phase, at a given frequency, in the perturbing bead position by measuring the complex variation of the reflection coefficient with and without the perturbing object. The perturbing object that has been used is a metallic spherical bead with a diameter of 1 mm, that can be moved along the structure axis using the step motor controlled by Labview VI. The set-up has been tested at different bead velocities along the axis in order to avoid ”wobbling” during the measurement and to check the system accuracy. The distance covered by the beads to perform the measurement on the C-band structure was 1930 mm covered in 60 s.

The Labview VI allowed to control the network analyzer and the step motor to perform the measure in an automatic way. All the parameters of the motor and of the network analyzer could be easily set in the front panel of the VI. Matlab

routines for data analysis have been implemented, hence , after one measurement, the data was stored and automatically analyzed. Then the results of the analysis were plotted on the screen.

The measurement procedure can be summarize in the following steps:

1. Settings on the front panel of all the measurement parameters: measurement time (ms), measurement length (mm), excitation frequency (Hz), start frequency (Hz), stop frequency (Hz), number of the measurement, etc;

2. Start of the Steele measurement: The VNA, controlled by the VI, starts a sweep at constant excitation frequency, synchronized with the movement of the bead within the structure, where it measures S_{11} with the bead perturbation.

3. Elaboration of the measurement: the amplitude and phase of the electric field calculated through expression 3.1 are plotted (see Figure 3.9), together with the results of the tuning algorithm and the data are stored in the PC.

In Figure 3.6 is showed the front panel of the realized Labview interface. The left part is relative to the motor control and his settings. After setting the measurement parameters, the VI calculate the step motor velocity and the number of steps of the motor. The central parts refers to the network analyzer connection and configuration. It allows to set all the parameters for the measurement, while the right part present some utilities to help in saving and plotting the results. In the lower side there are the panels to start a Steele measurement, by setting the excitation frequency and the number of the measure, and that for the Slater method used for field measurement of standing wave structure. This last has been used for the ELI-NP RF gun measurements that will be described in the next Chapter.

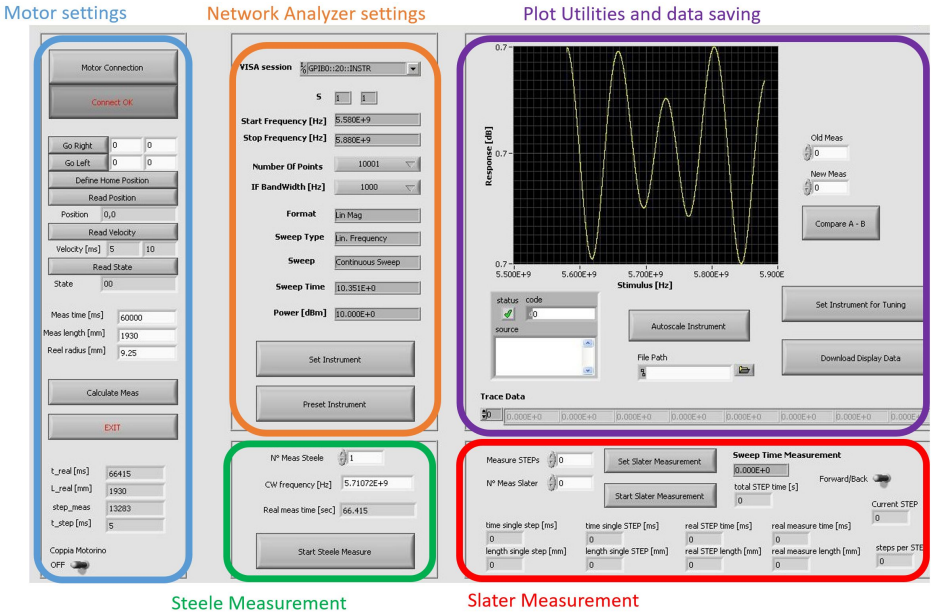

Figure 3.6: Labview VI front panel used for the bead-pull and bead-drop measurements.

Tuning procedures

Generally, the tuning of an accelerating structure consists in the introduction of a deformation on the cavity wall in order to correct the cell-to-cell phase advance and minimize the input reflection coefficient S_{11}. In the ELI-NP structures this deformation is obtained by applying a force on the outer wall of a cell. The bi-directional tuner, that have been used, allows to apply this force in both directions (outward and inward) in order to increase or decrease the internal volume of the cell. The whole TW structure is seen as a lossless transmission line in which the longitudinal electric field in the n-th cell is expressed by the sum of a progressive wave A_n and a regressive wave B_n. For each cell it can be defined a local reflection coefficient:

$$\Gamma_n = \frac{B_n}{A_n} \tag{3.2}$$

which can be expressed as function of the peak field in the n-th cell and the two adjacent cells n-1 and n+1. By measuring the field profile through bead-pull technique, it is possible to obtain this parameter for each cell. The imaginary

part of this local reflection coefficient is linked to the resonant frequency of the cell and allows to predict the sign of the resonant frequency shift that should be applied to correctly tune the cell:

$$\Gamma_n \approx j\frac{Q'_{o,n}\Delta f_n}{f_{RF}} \Rightarrow \begin{cases} Im\Gamma_n > 0\, \Delta f > 0 \rightarrow f_{res} - f_{RF} > 0 \rightarrow pull \\ Im\Gamma_n < 0\, \Delta f < 0 \rightarrow f_{res} - f_{RF} < 0 \rightarrow push \end{cases} \tag{3.3}$$

where $Q'_{0,n} = \frac{c\varphi_n}{v_{g,n}}$, with $v_{g,n}$ the group velocity in the n-th cell and φ_n the phase advance per cell. A detailed description of the tuning algorithm can be found in [55, 56]. The tuning process of a structure starts with its complete RF characterization, measuring the transmission and reflection coefficients at each port. All the plots reported in this section refers to the 4th C-band structure realized, the results of the other structures tuned so far are reported in subsection 3.4.

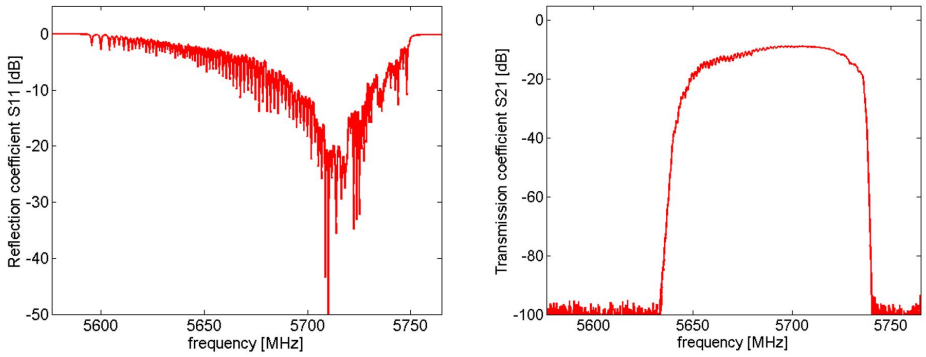

Figure 3.7: Reflection coefficient S_{11} (left) and transmission coefficient S_{21} (rigth) of the 4th C-band accelerating structure before the tuning procedure.

The red curve in Figure 3.9 shows the field profile measured before the tuning and in Figure 3.7 the measurement of the S_{11} and S_{21} of the section are reported. At the operating frequency the structure shows reflections of about -20dB. From the measured data, optimizing the particles injection phase and considering a nominal power at the input of the section of $40\,MW$, a maximum acceleration gradient equal to $24.44MV/m$ (about 26% less than the nominal gradient) has been calculated for this structure.

To excite the structure correctly during each field measurements and consequently tune the structure at the right operation frequency, two contribution have to be considered: the frequency shift due to the presence of the nylon wire inside the structure and the shift due to the difference of ambient conditions during the measurements from the working ones. The wire contribution has been evaluated through electromagnetic simulations and and comparing the measurement of the S_{11} with and without the wire inserted inside the structure (Figure 3.8). This contribution has been evaluated about $-360\,kHz$ with good agreement between measurement and simulations.

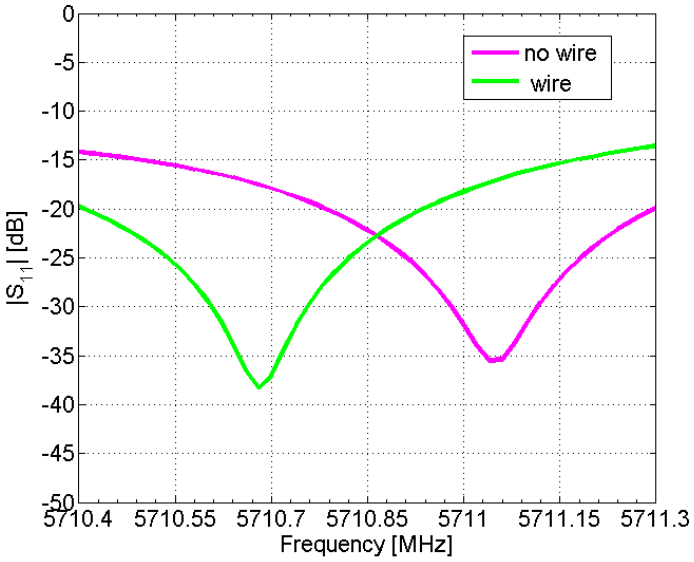

Figure 3.8: Reflection coefficient of the C-band structure measured with and without the nylon wire inside. A frequency shift due to the wire of 360 kHz has been measured.

The frequency shift due to the presence of air inside the structure (instead of vacuum) and to the different ambient temperature with respect to the operating one, have been considered by scaling the resonance frequency as function of the air humidity temperature and pressure and the structure temperature, through the expression:

$$f'_{RF} = \frac{f_{RF}}{(1 + 1.7 \cdot 10^{-5}(T_{amb} - T_{op}))} \frac{1}{\sqrt{\varepsilon}} \tag{3.4}$$

where $f_{RF} = 5712\,MHz$ is the operation frequency of the structure at the nominal temperature $T_{op} = 30°C$. In order to calculate the relative dielectric constant ε and pressure P_0 the following formulae have been used:

$$\begin{aligned} \epsilon &= 1 + P_{air}/T_{amb}(211 + P_0 H_{air}/P_{air}(10160/T_{amb} - 0.294)) \cdot 10^{-6} \\ P_0 &= 10^{(7.45(T_{amb}-273)/(T_{amb}-38.3)+0.656} \end{aligned} \tag{3.5}$$

where H_{air} is the air humidity, P_{air} the air pressure and T_{amb} is the temperature of the structure during the measurement. This frequency shift was of the order of 1 MHz. To perfectly center the nylon wire into the section hole two pierced teflon dishes as been realized and installed at the input and output of the section. All the measurements has been acquired with the Vector Network Analyzer R&S ZVB 20.

The procedure used can be divided in the following steps:

1. Measurement of electric field amplitude and phase through bead-pull technique at the scaled frequency, as discussed in the previous section;
2. identification of the center of each cell through the local maximum of the electric field;
3. calculation of the local reflection coefficient Γ_n and of the detuning of each cell;
4. tuning of the cells using the bidirectional tuners disposed around the cells according to equation 3.3. In order to evaluate the deformation given to each cell the modulus of the global reflection coefficient variations $|\Delta S_{11}|$ (linked to the variation of the local reflection coefficient [56]) is monitored during this phase.

This procedure is iterative, groups of five-ten cells have been tuned together, verifying, for each iteration, the effects of the applied deformations. The procedure was started from the last cell near the output coupler and proceeds backward up to the input coupler. We tuned the structure in order to have a phase advance per cell equal to 120 ± 2 deg with a cumulative error in the phase advance per cell

within $5°$. According to the analysis described in 3.4. These conditions allow to have a reduction of the final accelerating field $< 0.5\%$.

The electric field profile inside the structure has been reconstructed from the bead-pull measurement and it has been shown in Figure 3.9 before (left) and after (right) the tuning.

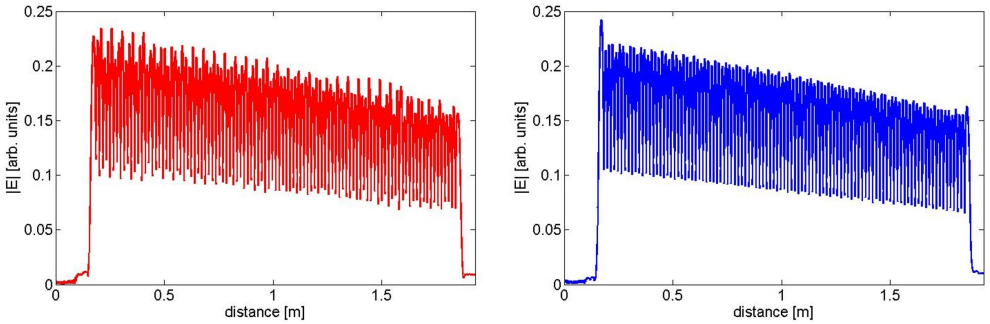

Figure 3.9: Electric field module on the axis of the 4th C-band accelerating structure, (left) before and (right) after the tuning procedure.

In Figures 3.10, and 3.11 are reported the phase advance per cell and the cumulative phase advance along the structure. In Figure 3.11 is reported the plot of Re(S_{11}) vs Im(S_{11}). The superimposition of the three petals which present an angle of $2\pi/3$ between them is an indication of the structure tuning.

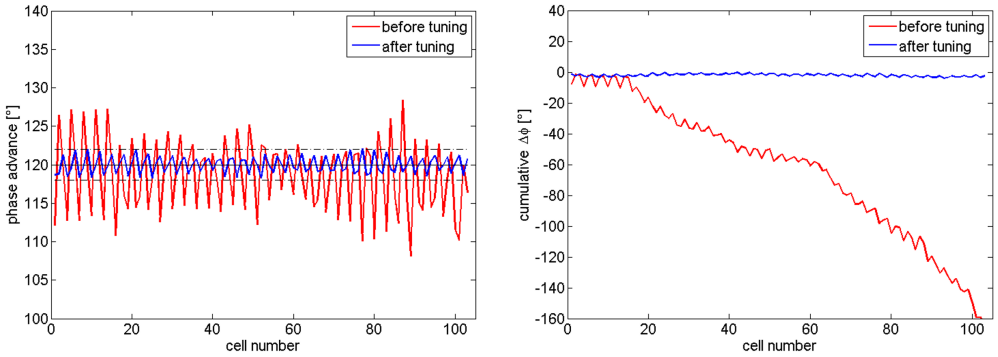

Figure 3.10: Phase advance per cell (left) and cumulative phase avance (right) of the 4th C-band accelerating structure before and after the tuning procedure.

The final field flatness was below 1%, the phase advance per cell was within $\pm 2°$ with respect to the nominal one and the cumulative phase advance total

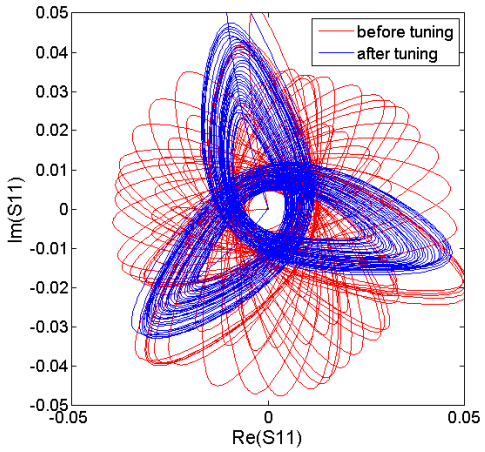

Figure 3.11: Plot of Re(S_{11}) vs Im(S_{11}) of the 4th C-band accelerating structure before and after the tuning procedure.

range for this structure was $4.1°$. After the tuning procedure the wire has been removed and the scattering parameters of the structure have been measured again. The reflection coefficient at the input port and the transmission coefficient are reported in Figure 3.12. The measured S_{11} of the tuned structure was about $-30\,dB$ at the working frequency.

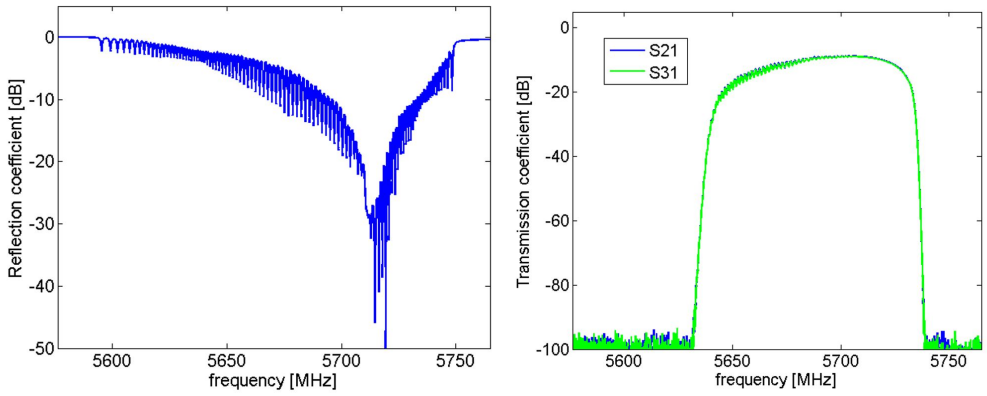

Figure 3.12: Reflection coefficient S_{11} (left) and transmission coefficient S_{21} (right) of the 4th C-band accelerating structure after the tuning procedure.

Results for the ELI-NP C-band structures

Nowadays four ELI-NP C-band structures have been realized, tuned and tested successfully. In Figures 3.13, 3.14, 3.15 and 3.16 the results of the tuning and low power measurements of the four ELI-NP C-band accelerating structures realized so far are reported.

The non uniformities of the field profile at the end of the first two structures have been introduced on purpose, in order to correctly compensate a strong field reflection in the output coupler. The strong reflections at the output coupler probably derives from deformation of the cell coupler dimensions during the brazing process. This effect can be observed also in the plot of the phase advance per cell as well as in the cumulative phase advance, shown in Figure 3.17. In the 3rd section this problem has been partially fixed, after simulations with Ansys HFSS, increasing the dimensions of the output coupler cell and it has been completely eliminated in the 4th section. Table 3.2 resumes the tuning results for the structures realized, reporting the values of some main parameters before and after the tuning procedure.

	Before tuning			**After tuning**		
Sect.	S_{11}	$\Delta\Phi_{cum}$	E_{acc} at 40MW	S_{11}	$\Delta\Phi_{cum}$	E_{acc} at 40 MW
1	-18 dB	302°	7.2 MV/m	-33 dB	5°	32.96 MV/m
2	-14 dB	179°	24.4 MV/m	-28 dB	4.8°	32.93 MV/m
3	-15 dB	160°	25.2 MV/m	-29 dB	4.7°	33 MV/m
4	-23 dB	162°	24.45 MV/m	-29 dB	4°	33 MV/m

Table 3.2: Summary of some parameters of the ELI-NP C-band structure before and after the tuning procedure.

In Figure 3.17 are reported the plots of the cumulative phase advance for all the tuned structures. Also in this case in the first three structures can be seen the effect of the output coupler reflection compensation through the last cell. For each structure a deviation $< \pm 2^\circ$ on the delta phase advance per cell $\Delta\phi$ and a total cumulative phase advance excursion $< 5^\circ$ have been obtained. These two conditions must be fulfilled at the same time in order to guarantee the nominal acceleration gradient.

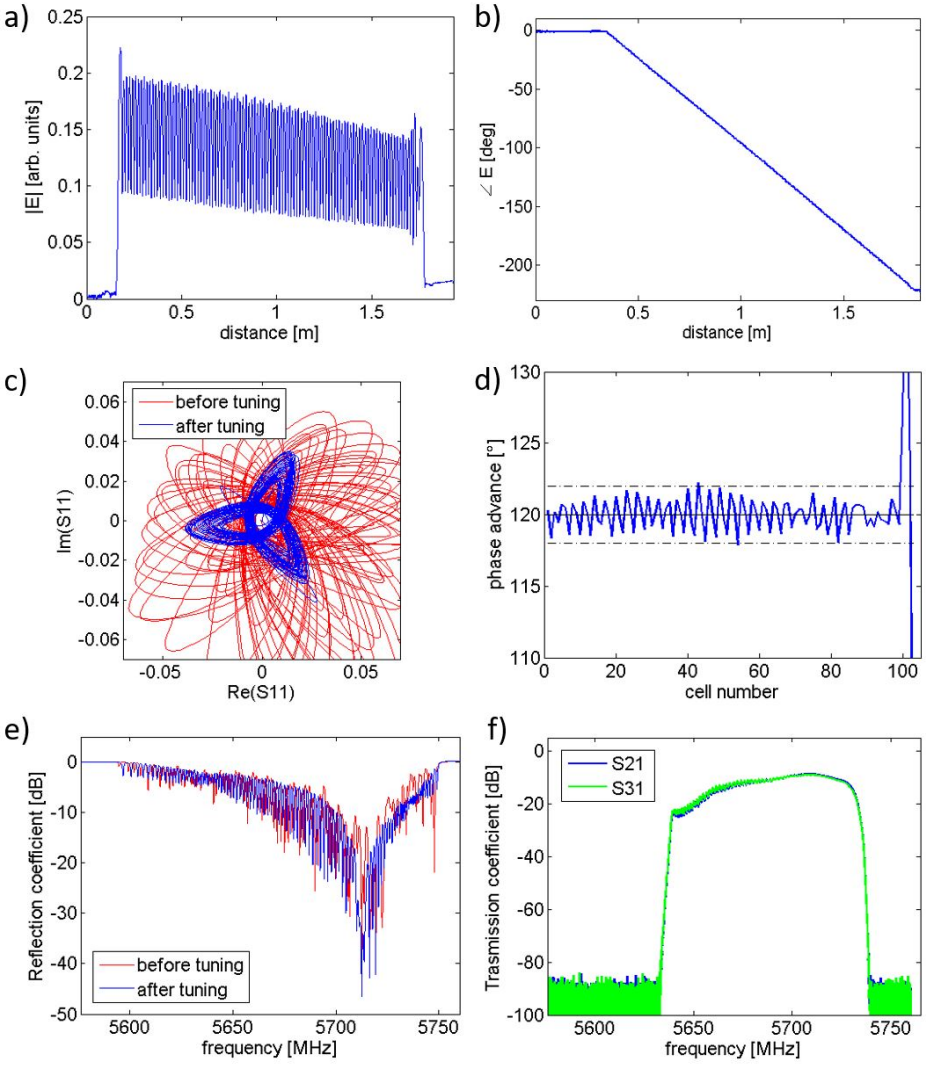

Figure 3.13: Low power RF measurements of the first ELI-NP C-band accelerating structure after the tuning procedure. Electric field amplitude (a) and phase (b) on the axis of the structure, "flower" diagram (c), phase advance per cell (d), reflection coefficient (e) at the input of the structure and transmission coefficients (f) at the structure ports.

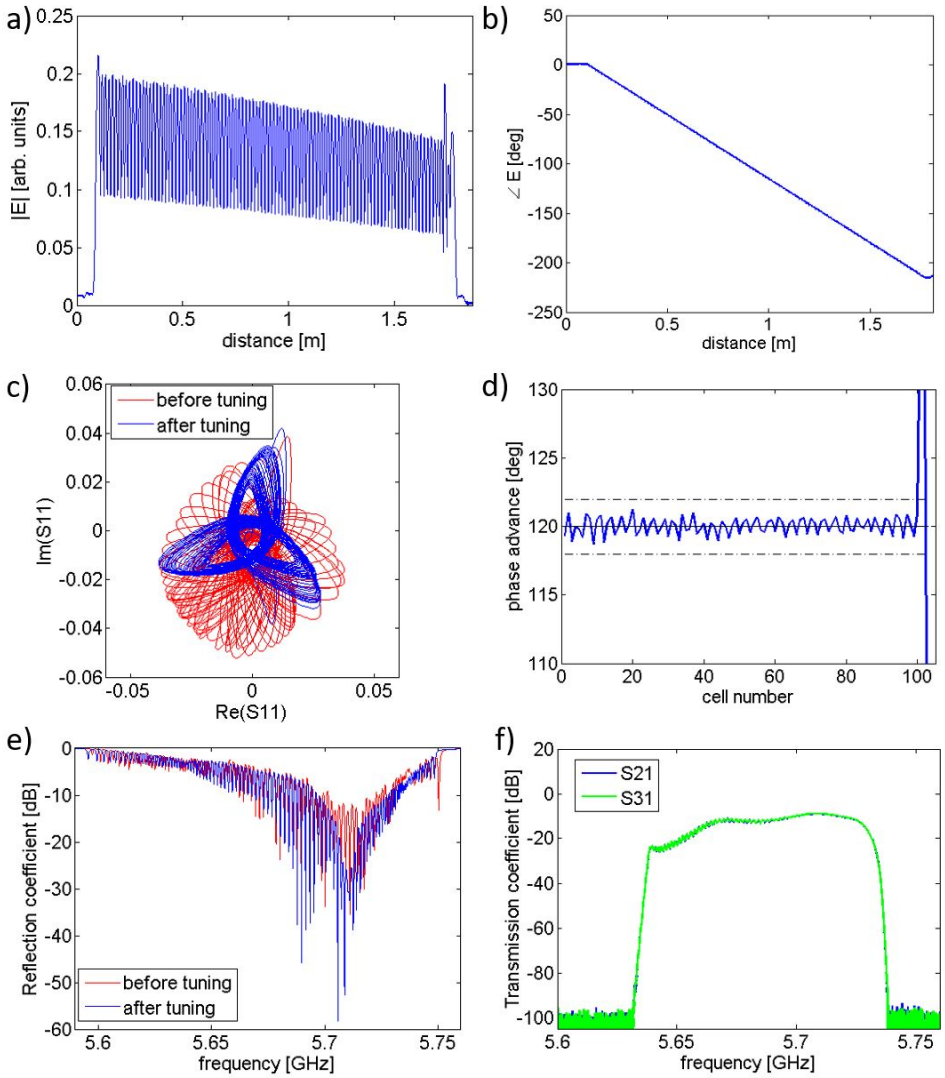

Figure 3.14: Low power RF measurements of the second ELI-NP C-band accelerating structure after the tuning procedure. Electric field amplitude (a) and phase (b) on the axis of the structure, ”flower” diagram (c), phase advance per cell (d), reflection coefficient (e) at the input of the structure and transmission coefficients (f) at the structure ports.

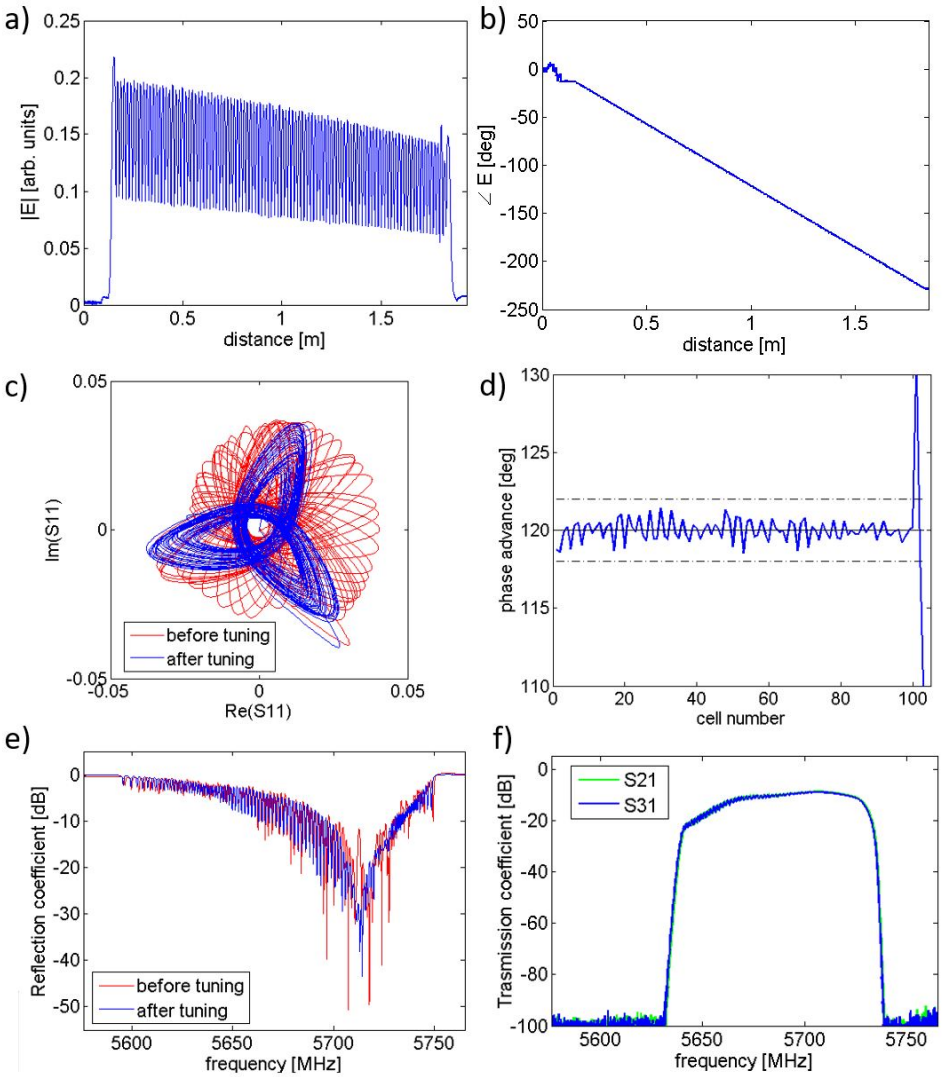

Figure 3.15: Low power RF measurements of the third ELI-NP C-band accelerating structure after the tuning procedure. Electric field amplitude (a) and phase (b) on the axis of the structure, ”flower” diagram (c), phase advance per cell (d), reflection coefficient (e) at the input of the structure and transmission coefficients (f) at the structure ports.

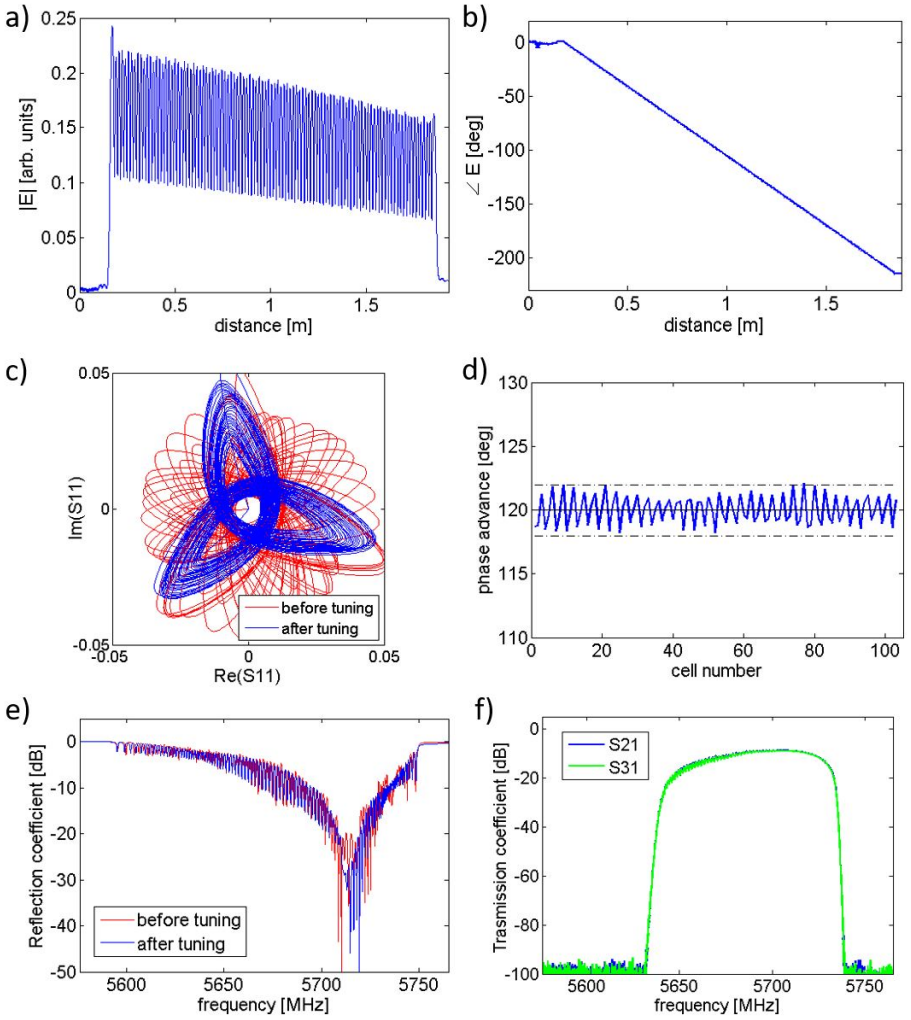

Figure 3.16: Low power RF measurements of the fourth ELI-NP C-band accelerating structure after the tuning procedure. Electric field amplitude (a) and phase (b) on the axis of the structure, ”flower” diagram (c), phase advance per cell (d), reflection coefficient (e) at the input of the structure and transmission coefficients (f) at the structure ports.

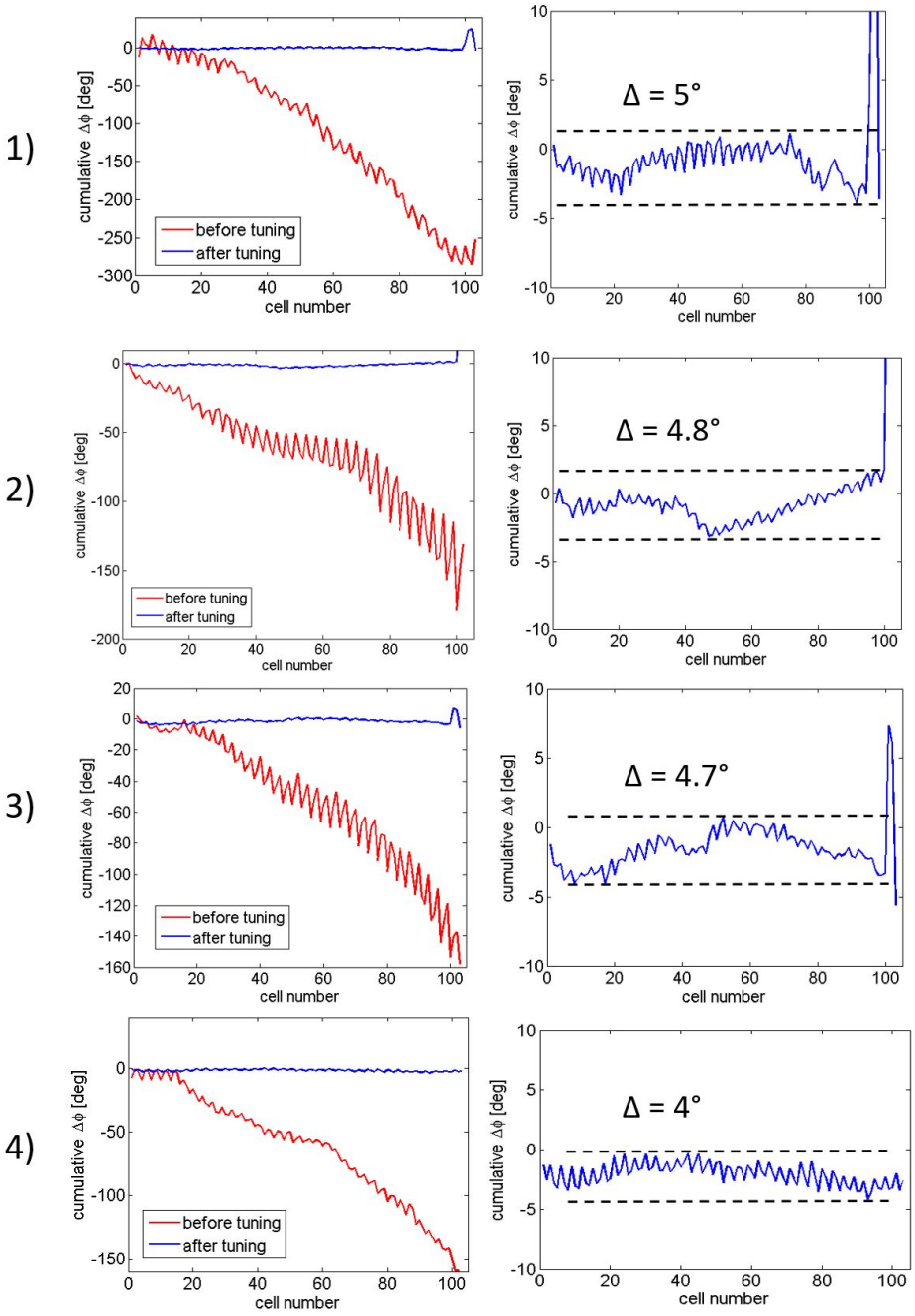

Figure 3.17: Cumulative phase advance before and after the tuning procedure for the first four ELI-NP C-band TW structures.

Analysis of tuning efficiency

A statistic evaluation has been done in order to fix the conditions that allow to determine the allowable tolerances in the final phase advance per cell, after tuning. As reported in [57, 58] the energy gain of an electron of charge e traveling in a TW structure can be expressed as:

$$\Delta W = e \cdot V_{acc} = e \int_0^L E(z) \cdot \cos\left[\omega t - \int_0^z k(z')dz' + \phi\right] dz \tag{3.6}$$

where $E(z)$ is the electric field along the axis of the structures ($E(z) = \sqrt{Z(z) \cdot P(z)}$), L is the structure length, ω is the angular frequency of the electric field, $k(z) = \omega / v_{phase}(z)$ is the wave number and ϕ is the electron injection phase. Converting the previous equation in the discrete domain ($L \rightarrow Ncells$), the accelerating voltage V_{acc} became:

$$V_{acc} = \sum_{i=1}^{N} E_n D \cos\left(\omega \frac{i \cdot D}{c} - \sum_{n=1}^{i} \beta_n \cdot D + \phi\right) \tag{3.7}$$

where D is the cell length and considering that $\frac{\omega D}{c} = kD = \Delta\phi_{nom} = \frac{2\pi}{3}$ and $\beta_n \cdot D = \Delta\phi_i$ is possible to write:

$$\begin{aligned} V_{acc} &= \sum_{i=1}^{N} E_n D \cos\left(i \cdot \phi_{nom} - \sum_{n=1}^{i} \phi_n + \phi\right) = \\ &= \sum_{i=1}^{N} E_n D \cos\left(\sum_{n=1}^{i} (\phi_{nom} - \phi_n) + \phi\right) = \\ &= \sum_{i=1}^{N} E_n D \cos\left(\sum_{n=1}^{i} \Delta\Phi_n + \phi\right) \end{aligned} \tag{3.8}$$

where $\Delta\Phi_n = \phi_{nom} - \phi_n$ is the deviation of the real phase advance at cell n from the nominal phase advance $2\pi/3$. The sum of all the $\Delta\Phi_n$ along the structure is the so called cumulative phase advance error. Through equation 3.8 it is possible to calculate the accelerating gradient for a given distribution of the phase advances per cell. Using equation 3.8 and random phases distributions it is

also possible to calculate the expected reduction in the average accelerating field due to the detuning of the structures. In Figure 3.18 it is reported, as an example, the distribution of the average accelerating field variation calculated considering 10000 random cases. The random phases, in each case, have a uniform distribution with a maximum deviation $\Delta\Phi = \pm 2^\circ$ and different maximum cumulative phase advance errors $\sum \Delta\Phi_n = 10^\circ,\ 20^\circ,\ 100^\circ$. From the plot it is possible to to see that both the maximum phase advance deviation than the cumulative errors play an important role in the final efficiency of the structure.

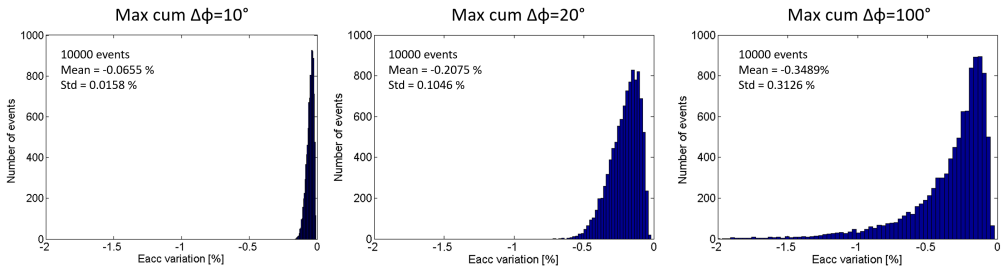

Figure 3.18: Events distributions of the accelerating gradient variation with respect to the nominal one computed for different values of the maximum cumulative phase advance (10°, 20° and 100°) at constant maximum phase advance deviation $\Delta\Phi = \pm 2^\circ$.

The effect of the cumulative phase advance can be seen also in Figure 3.19, where the percent variation of the accelerating gradient has been calculated as function of the maximum cumulative phase advance for different values of maximum $\Delta\Phi$. In particular, the mean value of the distribution, the mean value minus $3\times$ standard deviations and the minimum value achievable are reported.

With a cumulative lower than 10° and a Δ phase advance included in ± 2 we have the nominal accelerating gradient $33\,MV/m$ with a maximum deviation lower than the 0.5% In this way we have been able to confirm that the conditions $\Delta\Phi < \pm 2^\circ$ and max cumulative $\Delta\Phi < 5^\circ$ are very conservative and guarantee the nominal performance of the structure.

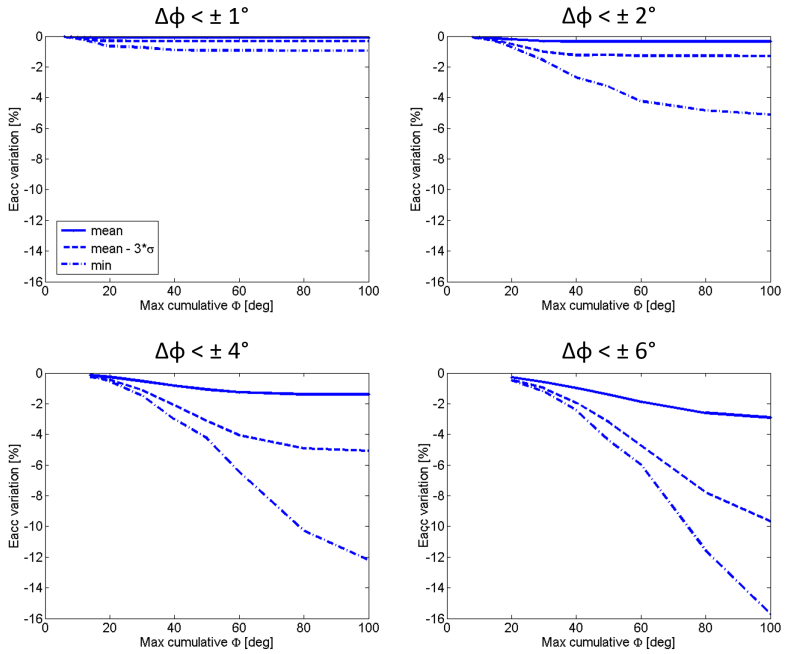

Figure 3.19: Percent variation of the accelerating gradient as function of the maximum cumulative phase advance for four different Δ phase advance maximum deviations: $\pm 1^\circ$ $\pm 2^\circ$, $\pm 4^\circ$ and $\pm 6^\circ$.

3.5 High power test

Radiofrequency components need to be conditioned to reach the nominal parameters in term of accelerating gradient and pulse duration. The goal of the conditioning process is to expose the internal surface of the component to a ramped RF power in order to clean it. The surface is cleaned by several effects: induced out-gassing due to RF-heating, arcing, multipacting enhances local heating and desorption. To avoid damages to the structures RF conditioning has to be done gradually and in a controlled way. Generally during the conditioning process different parameters are monitored, like the vacuum quality inside the RF components and the forward and reflected RF signals in different points of the set-up. These parameters are used to verify the progress in the conditioning but also to generate interlocks in order to protect the components in case of breakdowns.

The conditioning and high power test of the first ELI-NP C-band accelerating structure was held at the ELSA facility at the University of Bonn under Research

Instrument GmbH [59] responsibility with the collaboration of the INFN. Only the high power test of the first fabricated structure has been performed in this test area, the next structures will be conditioned directly at the installation site. A picture of the structure under high power test is given in Figure 3.20 and a schematic layout of the experimental set-up is shown in Figure 3.21.

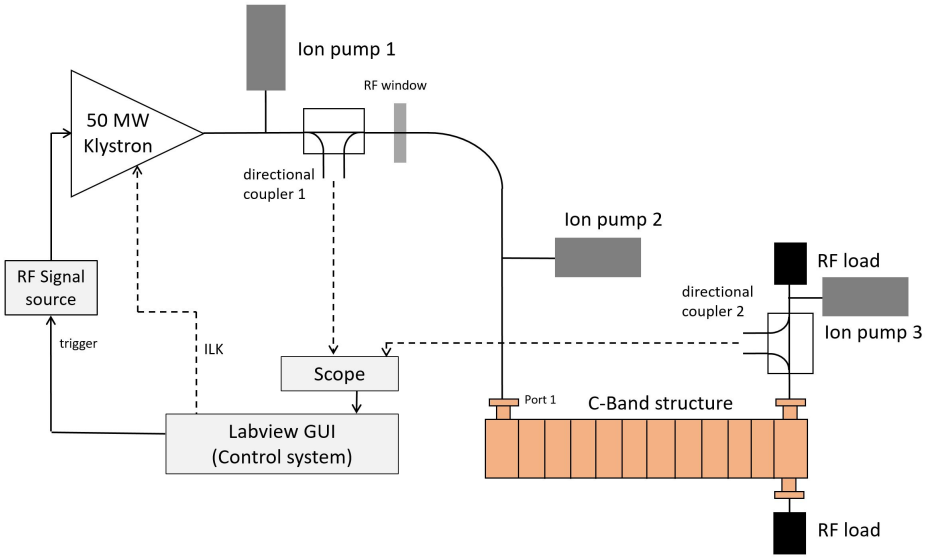

Figure 3.20: Schematic diagram of the high power RF test set-up of the first ELI-NP C-band accelerating structure.

The experimental Set-Up was composed by the following elements:

1. LLRF system (signal generator and switch);
2. 50 MW C-band RF Source;
3. two directional couplers (DC1 and DC2);
4. three vacuum ion pumps;
5. two water cooled RF loads;
6. chiller for structure cooling.

The power source was the ELI-NP nominal one (described in 2.3): Scandinova RF Unit based on Solid State modulator K2-2 adapted for 50MW C-band

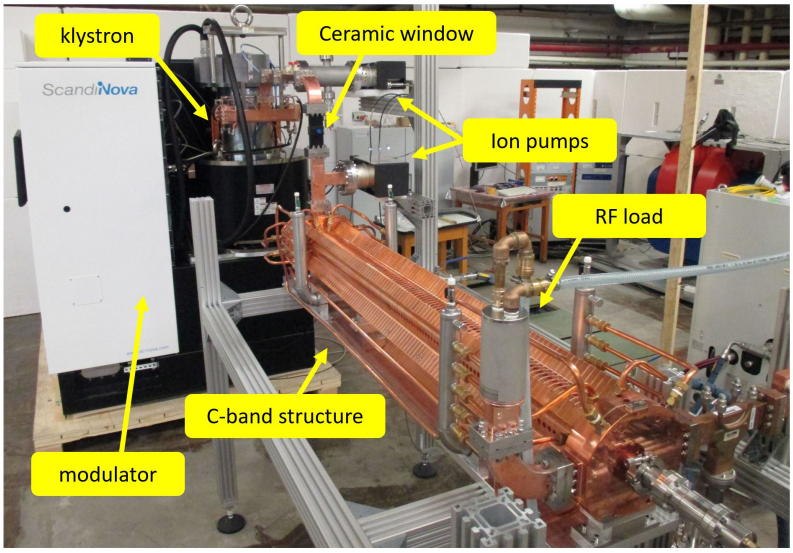

Figure 3.21: Picture of the high power RF test set-up of the first ELI-NP C-band accelerating structure in the ELSA Facility (Boon, Germany).

Toshiba klystron E37212. For this test was not foreseen the final low level RF system, to form and shape the RF input pulse profile, thus, it was generated by a setup similar to the one used during the factory acceptance test of the modulators. The C-band RF signal was generated through a $\times 2$ frequency multiplier combined with a 3 GHz signal generator an amplifier, a pass-band filter and a RF switch that receives the 100 Hz from the control system. The conditioning procedure was semi-automatic and has been performed from the ELSA control room. During the whole test the signals of the directional couplers pickups and the current absorption of the three ion pumps have been monitored. The forward/reflected power signals at the input and output couplers were measured using diodes and an oscilloscope (see Figure 3.22). These readings were recorded by means of a Labview GUI which calculates the corresponding power levels.

To prevent damages of the structure due to discharge and breakdown, different interlock systems have been implemented. By turning off the trigger signal to the modulator, these system removed the RF power pulse at the output of the klystron. An interlock was implemented in the Labview control system and stopped the trigger signal if the ion pumps current absorption exceeded a threshold corresponding to a pressure of 1×10^{-7} mbar. A second interlock system

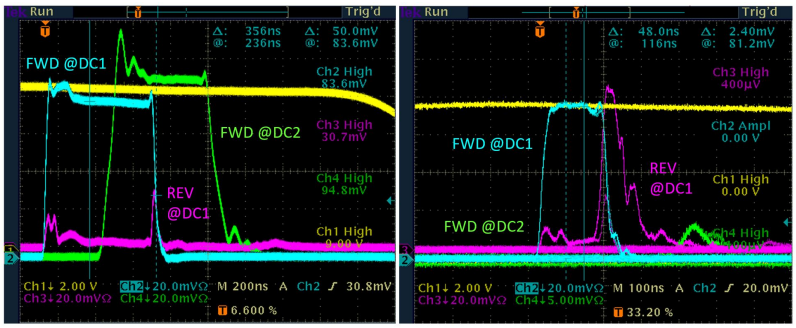

Figure 3.22: Signals measured by an oscilloscope during the RF conditioning of the first C-band ELI-NP structure: normal operation (Left), breakdown event (right).

was embedded in the modulator in order to stop the trigger signal if the reflected peak power, measured from DC1, exceeded the 10% of the forward peak power level. In addition, there were the internal interlocks on the status of modulator and an interlock on the cooling of the structure.

The conditioning strategy was to increase progressively the RF power acting on the high voltage (HV) of the modulator, keeping constant the LLRF input. The goal of the entire test was to reach 40 MW pulse peak power, at the input coupler of the accelerating structure, at a repetition rate of 100 Hz with 820 ns pulse width (one filling time plus beam time). The conditioning started at 10 Hz with a pulse of 100 ns and minimum power. Reached the nominal input pulse power, the repetition rate was increased and if the system was stable the pulse length could be increased starting again the ramp from the minimum input power.

The target values have been reached after 190 hours. In Figure 3.23 the behavior of the RF Pulse length, input power and repetition rate as a function of time are reported. The vacuum pressure has been constantly measured both at the beginning and at the end of the structure and after reaching the final nominal parameters of the structure was of the order of 1×10^{-8} mbar. Figure 3.24 shows the vacuum pressure measured by the three ion pumps current absorption as a function of the conditioning time. The reached breakdown rate at the end of the conditioning procedure was of the order 10^{-6} bpp/m.

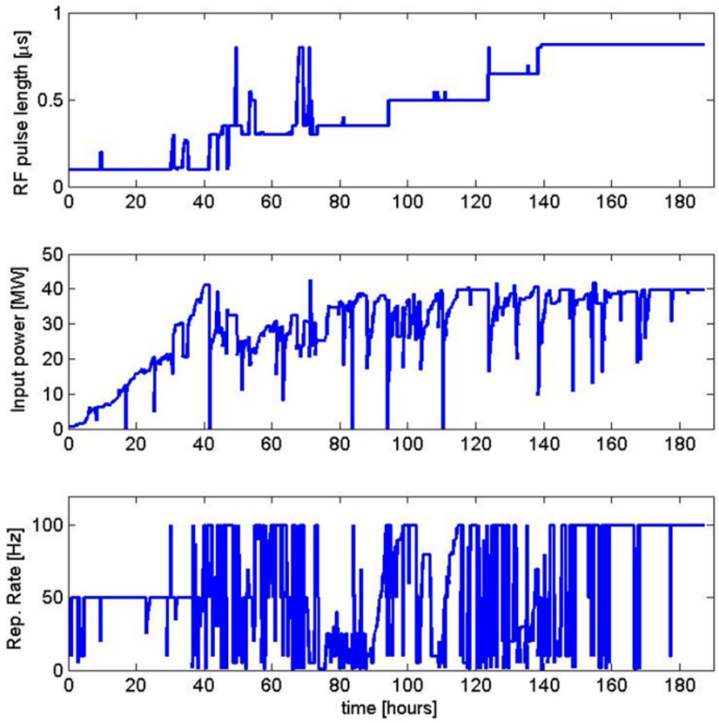

Figure 3.23: Behavior of the RF pulse length, input power and repetition rate as a function of time during the high power test of the first ELI-NP C-band structure.

3.6 Beam loading compensation

In the scope of this thesis work, calculation of the beam loading effect in the ELI-NP C-band structure has been performed and a possible scheme for its compensation has been studied. The beam passing through a cavity is equivalent to a generator which can either absorb energy from the cavity modes or deliver energy to them. The effects of the beam on the cavity fields in the accelerating mode are referred to as beam loading. They arise physically as a result of the charges induced in the walls of the cavity as the bunches, together with their co-moving electromagnetic fields, pass through the cavity [57]. The main effect of the beam loading is the decrease of the accelerating field gradient in the structure since the effective field can be assumed as a superposition of the RF field and of the induced longitudinal wakefield. When a single bunch passes through a TW structure it leaves part of its energy exciting the fundamental mode with

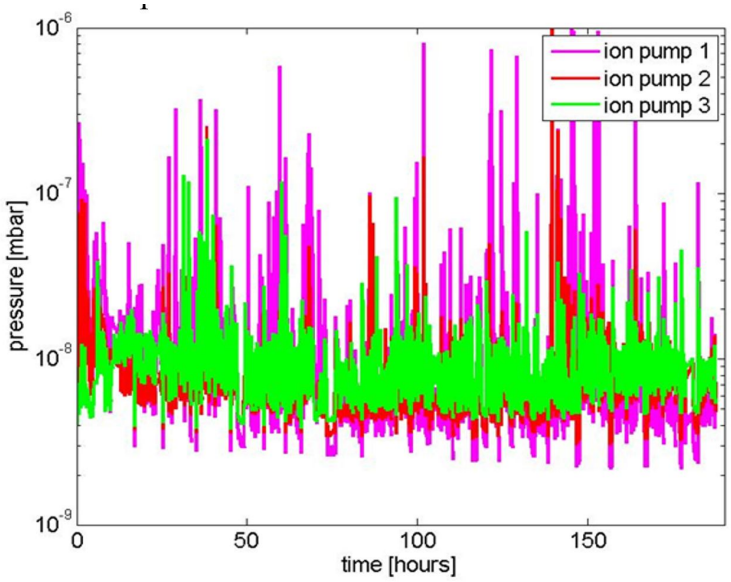

Figure 3.24: Vacuum pressure as a function of the conditioning time during the high power test of the first ELI-NP C-band structure.

a decelerating phase. The profile of the accelerating field perturbation travels forward along the structure with a local velocity equal to the group velocity of the structure, while the phase of the wave travels with the beam velocity (c). The total accelerating field probed by a subsequent bunch is the superposition of the propagating perturbation generated by the leading bunch and the external RF field. This simplified treatment neglects the dispersive effects related to the fact that the beam excites the field at all frequencies of the pass-band accelerating mode. All field components propagate into the structure with different group and phase velocities. A complete treatment has been done for other structures [60] and demonstrated that this simplified approach describes with an acceptable approximation the whole beam loading process.

The beam loading affects the RF acceleration efficiency in terms of effective accelerating gradient, hence, if not compensated, it can produce a variation of the bunch energy along the train from the first to the last bunch. In the ELI-NP case, this bunch to bunch energy spread produced by beam loading effect has been studied in detail in [61] and, if not properly compensated, can easily overcome the machine specifications ($< \pm 0.1\%$). There are quite a few techniques to

compensate this effect [62, 63, 64, 65, 66], as reported in [67], in our case we propose to use the pulse shaping capabilities of the low level RF system through the amplitude modulation of the input RF power signal that drives the klystron. Before the injection of the first bunch into the accelerating structure, it must be pre-loaded with a field profile equal to the steady state beam loading one. In order to evaluate the steady state field due to beam loading a first order study has been performed for the ELI-NP C-band travelling wave structures. Assuming each bunch as a point-like charge, the longitudinal wakefield at the working frequency excited in the structure by a single bunch (per unit charge) can be computed by [68] :

$$W(z) = \frac{1}{2}\omega_{RF}\frac{r}{Q} = \alpha v_g r \tag{3.9}$$

where ω_{RF} is the C-band angular frequency, r is the shunt impedance, Q the quality factor, α the field attenuation in the structure and v_g the group velocity.

As mentioned, the multi-bunch operations of the ELI-NP linac foresees trains of 32 bunches. Every 16 ns a new bunch arrives generating a longitudinal wakefield, at the working frequency, that propagate into the structure. Since the bunch train is longer than the filling time of the structure ($313\,ns$) after the passage of 20 bunches, which correspond to $320\,ns$, the field profile into the structure generated by the superposition of the wakes reaches a steady state. Therefore, after the passage of 20 bunches the structure is in a regime of "full beam loading". The details of the analysis are reported in subsection 3.6. A snapshot of the wake as experienced by the 20th bunch and by the following ones while travelling along the structure is shown in Figure 3.25 (a).

Then the total wake potential is simply given by the sum of the 20 propagated sigle-bunch wakes times their charge (Figure 3.25 (b)). As said before the effective accelerating field is given by the difference between the ideal accelerating electric field and the total wake contribution. Thus, in order to compensate this transient effect and have a net average accelerating field equal to the nominal one (33 MV/m), the structure has to be preloaded with a tailored power pulse. The shape of the input RF pulse for an ideal beam loading compensation, assuming a bunch charge equal to $250\,pC$, is showed in Figure 3.26.

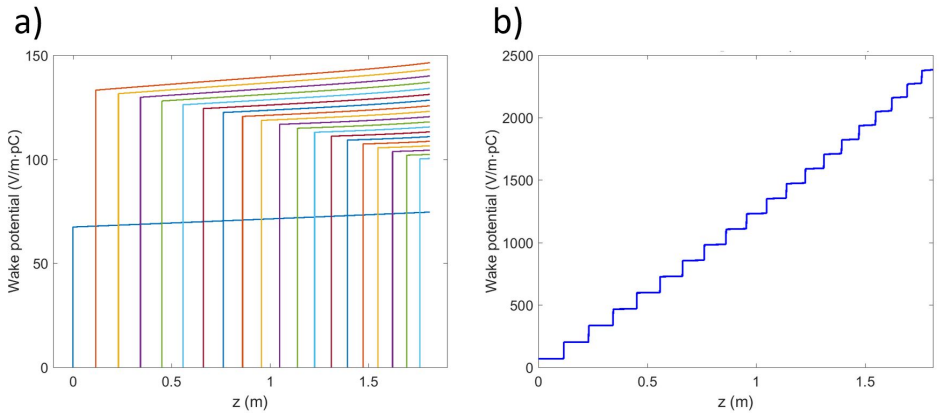

Figure 3.25: (1) Sanpshot of 20 wakefields propagating within the TW C-band structure and (b) calculated field profile after the passage of 20 bunches within the TW C-band structure.

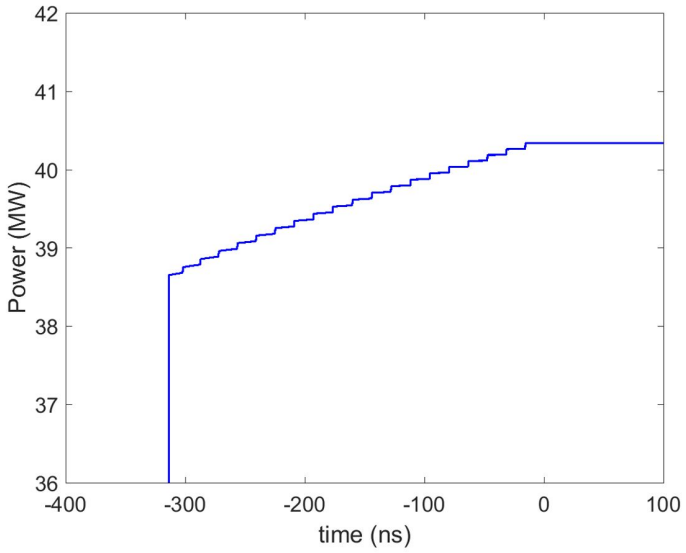

Figure 3.26: Input RF pulse for ideal beam loading compensation. The first bunch has to be injected at t=0.

However, it has to be taken into account that the shape of the actual vector modulator pulse will be distorted with respect to the one shown, mostly due to bandwidth limitation of the backend (16 MHz). Furthermore, a significant contribution from the bandwidth of the klystron system, which is expected to be of the order of 10 MHz, has to be considered. The real capabilities of the ELI

RF system for beam loading compensation will be investigated by means of a test with the integrated system composed by both LLRF and the C-band power source system.

Computation of the full beam loading field profile

Here is reported the analytic computation of the field profile in full beam loading regime, produced by the ELI-NP train of bunches in the C-band TW quasi-constant gradient structure. For the calculation of the long range wake-fields and their propagation within the structure we started from the main parameters for each cell in the structures, obtained from electromagnetic simulations: the linear field attenuation α, the group velocity v_g and the series impedance Z. Then, the quality factor ($Q = \frac{\omega_R F}{2\alpha v_g}$) has been computed for each cell and since its variation is rather small along the structure, it has been considered constant and equal to its mean value Q_{avg}=8860. Then, a direct dependence between $\alpha(z)$ and the group velocity $v_g(z)$ is established:

$$v_g(z) = \frac{\omega_{RF}}{2Q_{avg}\alpha(z)} \tag{3.10}$$

where the linear attenuation α_z has been fitted with a $3_r d$ degree polynomial:

$$\alpha(z) = \alpha_0 + \alpha_1 z + \alpha_2 z^2 + \alpha_3 z^3 \tag{3.11}$$

From the relations 3.10 and 3.11, the equation of motion of the pulse front edge $z = f(t)$ can be derived:

$$v_g(z) = \frac{dz}{dt} = \frac{\omega_{RF}}{2Q_{avg}\alpha(z)} \rightarrow \alpha(z)dz = \frac{\omega_{RF}}{2Q_{avg}}dt$$

$$t = f^{-1}(z) = \frac{2Q_{avg}}{\omega_{RF}} \sum_0^3 \frac{a_k}{k+1} z^{k+1} \tag{3.12}$$

The RF power $P(z)$ and the acceleration field $E(z)$ in the C-band section could be derived from:

$$\frac{dP(z)}{dz} = -2\alpha(z)P(z) \qquad E(z) = \sqrt{Z(z) \cdot P(z)} \tag{3.13}$$

then using equation 3.12 into the 3.13 the power and the field can be written as:

$$P(z) = P_0 e^{-2\sum \frac{\alpha_k}{k+1} z^{k+1}} = P_0 e^{-\frac{\omega_{RF}}{2Q_{avg}\alpha(z)} f^{-1}(z)} \tag{3.14}$$

$$E(z) = \sqrt{Z(z) P_0 e^{-2\sum \frac{\alpha_k}{k+1} z^{k+1}}} = \sqrt{Z(z) P_0 e^{-\frac{\omega_{RF}}{2Q_{avg}\alpha(z)} f^{-1}(z)}} \tag{3.15}$$

where P_0 is the power at the input of the first cell. These two quantities have been normalized to their peak values and reported in Figure 3.27.

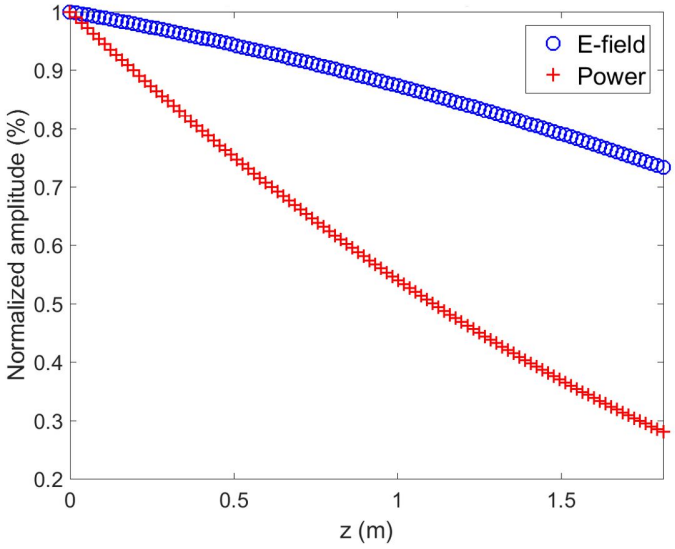

Figure 3.27: Normalized accelerating field (blue) and RF power (red) in the C-band structure.

The function $\eta(z) = E(z)/E_0$ is the linear form factor of the field along the structure (i.e. the profile of the blue curve in Figure 3.27). Thus, if the field value at a given position z_1 is $E(z_1) = E_1$, when the propagating wave reaches $z_2 > z_1$ the field value can be derived in this way $E(z_2) = E_2 = E_1 \frac{\eta(z_2)}{\eta(z_1)}$. At this point, being $r = Z/2\alpha$ the shunt impedance of each cell, using equation 3.9 is possible to calculate the longitudinal wakefield as a function of z for a single bunch (we are Assuming each bunch as a point-like charge). The function $W(z)$ represents the normalized electric field in the structure just after the passage of a point-like bunch, i.ee the field profile at t=0. That wake travels within the structure

according to the same non uniform equation of motion $f(z)$ and is attenuated as $\eta(z)$. So, after a certain amount of time $t > 0$, it becomes:

$$W(z, t > 0) = W(z', 0) \cdot \frac{\eta(z)}{\eta(z')} \cdot H(z') \tag{3.16}$$

where z' is the position at time $t = 0$ of the wavelet corresponding to position z at time $t > 0$. The use of the Heaviside function $H(z)$ is necessary to confine the wave within the structure. The value $z'(z, t)$ can be calculated using the equation of motion $f(t)$ founded before and its inverse function:

$$z' = f(f^{-1}(z) - t) \tag{3.17}$$

Since the filling time of the structure is about $313\,ns$ and the bunch separation is $T_b = 16\,ns$, the wake reaches a steady state after the passage of 20 bunches. If we consider a finite set of instants $t_n = nT_b$ (n=0,1,...19), it is possible to take snapshots of the wake every time a bunch arrives. All the functions $W(z, nT_b)$ have been calculated and the snapshots of the single bunch wake at $t = nT_b$ have been shown in Figure 3.25 (a). The wake experienced by the 20th bunch due to its own interaction with the structure is given, according to the beam loading theorem [68, 57], by a half of the single bunch potential. The total wake (W_{TOT}) induced by a train of 20 equal bunches, normalized to their charge, is equal to the sum of all the contributions of the calculated wakes and is shown in Figure 3.25 (b). The field profile in full beam loading (whose average is designed to be $E_{avg} = 33MV/m$) is defined as the difference of the nominal electric field in the structure and the total wake multiplied by the bunch charge ($E_{fullBL} = E_{nominal} - W_{TOT} \cdot Q_{bunch}$). Assuming $Q_{bunch} = 250\,pC$ the full beam loading field profile corresponding to an average accelerating field of 33 MV/m is shown in figure .

Clearly, the beam loading effects could be fully compensated if the structure is pre-loaded from the klystron with an electric field profile matching this full beam loading field profile. Then the RF power along the structure is given by $P_{fullBL}(z)^2/Z$ corresponding to an input power profile as a function of time $P_{in}(-t) = P_{fullBL}(f(t)) \cdot e^{\frac{\omega_{RF}}{Q_{avg}}t}$. In conclusion, the input power profile reported

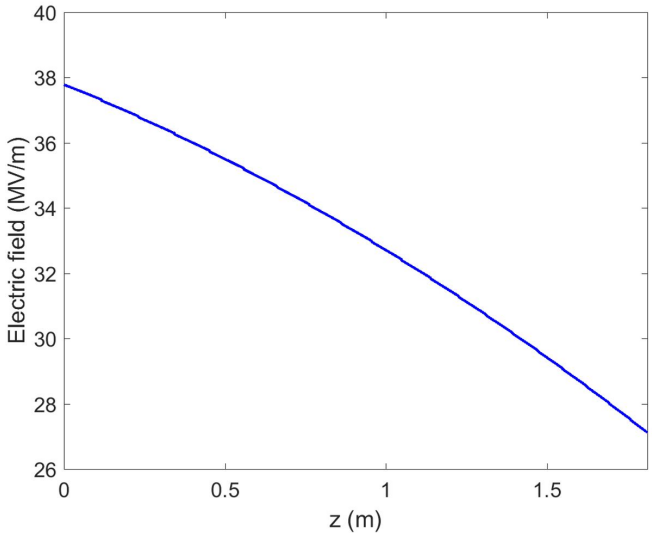

Figure 3.28: Accelerating field profile along the structure in full beam loading regime ($E_{avg} = 33MV/m$).

in Figure 3.26 provides the same average accelerating field of $33\,MV/m$ to each bunch, regardless of its position along the train.

CHAPTER

4 RF Electron Gun

Content

4.1 Introduction

The ELI-NP photoinjector is composed by an S-band radiofrequency Gun and two S-band travelling wave accelerating structures. Photocathode RF Guns are multi-cell standing wave (SW) structures, in which the electron beam is generated by photoemission using a drive-laser pulse to illuminate the surface of a copper cathode and is then quickly accelerated through high electric field. To control the transverse beam emittance of the beam at low energies, a solenoidal magnetic field is applied just after the accelerating cavities of the gun. The emittance of the beam is related to the beam brightness, defined as:

$$B = \frac{2I}{\varepsilon^2} \tag{4.1}$$

where I is the beam current and ε is the transverse emittance of the beam. In recent years much work and studies have been conducted, from the electromagnetic point of view, in order to increase as much as possible the peak field on the gun cathode, because the achievable beam brightness is proportional to the maximum achievable accelerating field at the cathode itself [69, 70, 71]. In the following sections the ELI-NP RF gun design criteria are briefly illustrated. Then the low and high power tests, are reported.

4.2 RF Gun design

The radiofrequency electron Gun designed for the ELI-NP Linac is a 1.6 cells gun of the BNL/SLAC/UCLA type [72]. With respect to the original design of such type of gun it implement several new radiofrequency and realization features that have been already integrated in the gun recently realized for the SPARC_LAB photoinjector [73] and currently in use at UCLA for electron diffraction experiments. In particular, this gun implements the new realization technique, called gasket-clamping technique, that has been recently developed at the INFN laboratory of Frascati [74]. This technique allows avoiding the brazing process in the realization of the gun by using special RF-vacuum gaskets that allow to guarantee at the same time the radiofrequency contact and the vacuum sealing when the different machined parts are clamped together. Figure 4.1 report the assembly procedure of the Gun realized with the clamping-gasket technique. The advantages of avoiding the brazing process and using this technique will be described in more detail in Chapter 5.

From the electromagnetic point of view, the main feature that have been implemented are:

- the iris profile of the cell has an elliptical shape and a larger aperture to simultaneously reduce the peak surface electric field, increase the pumping speed on the half cell and to increase the frequency separation between the 0-mode and the working π-mode to fed the gun using very short RF pulse.

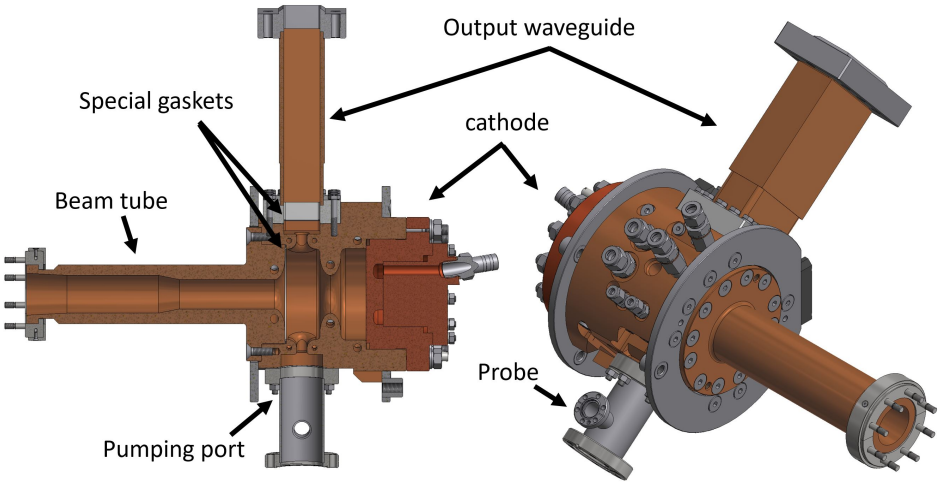

Figure 4.1: Mechanical drawing of the ELI-NP RF gun: longitudinal section (left), entire (right).

- two bi-directional tuners are present on the outer wall of the full cell, allowing to tune the fields at the right frequency by small deformation of the cell geometry.

- the profile of the coupling window between the rectangular waveguide and the full cell has been strongly rounded to reduce the peak surface magnetic field and, as a consequence, the pulsed heating [75].

Because the ELI-NP Gun has to work at 100 Hz repetition rate and long RF pulses for the multi-bunch operation, great attention has been also paid in the thermal design of this device. For this reason the number of the cooling pipes has been increased with respect to the SPARC gun and their position has been carefully designed to guarantee a better gun temperature uniformity. Also the copper cathode has been designed to incorporate a dedicated cooling system and to be easily replaced. To compensate the dipole field component, induced by the presence of the input coupling slot [76], a symmetric port has been inserted in the gun. This is used as pumping port and is connected to a circular pipe below cut-off that incorporates a calibrated probe that monitors the field inside the device. The final design parameters of the gun are summarized in table 4.1.

Parameter	Value
f_{res}	2856 MHz
RF repetition rate	100 Hz
Working mode	π
Max RF input power	16 MW
Peak field at the cathode	120 MV/m
Max RF pulse duration	$2\,\mu s$ (1.5 nominal)
RF pulse duration for beam	$0.5\,\mu s$
Q_0	14600
R/Q factor	117
Average dissipated power	1.3 kW
Working temperature	$34°C$
Coupling coefficent β	3
Filling time τ_F	420 ns
Shunt Impedance (R)	1.78 $M\Omega$
Operating vacuum pressure	$1 - 5 \cdot 10^{-9} mbar$
Number of cells	1.6
Type of cathode	copper
Cathode quantum efficiency (at 266 nm)	$> 2 \cdot 10^{-5}$
Frequency separations between 0 and π-mode	40 MHz

Table 4.1: Parameters of the ELI-NP RF gun.

4.3 Low power measurements of the prototype

First of all, to verify the electromagnetic design and to test the overall realization process a simplified prototype of the gun has been realized. Low power measurements on this prototype have been conducted through a Vector Network analyzer (VNA) R&S ZVB 20. In Figure 4.2 is reported a picture of the RF gun prototype, taken during the test. It has been made of Anticorodal 6082 (Al), that is a magnesium-aluminum-silicon alloy, so the results obtained by the measurements on the prototype have been scaled to compare them with the design parameters of the real copper RF gun.

For the RF characterization, the waveguide port has been connected to a waveguide to 3.5 SMA adaptor, while the gun probe, used for transmission measurements, has been realized with the inner conductor of a coaxial cable

Figure 4.2: ELI-NP RF Gun prototype made of Anticorodal 6082.

inserted in the circular pipe below cut-off, connected on the other side of the full cell through the pumping port. This antenna probe inside the pipe has been positioned to be undercoupled. A resonant frequency of the π-mode equal to 2.85565 GHz has been measured in air (Humidity = $40\,\%$, $T_{air} = 24.2°C$, $T_{gun} = 23.9°C$, Pressure = 991 hPa, $\sigma_{Al} = 28 \cdot 10^6$ S/m) and this is in good agreement with the calculated resonant frequency that we expect for the Gun prototype in vacuum calculated with 3.4. To estimate correctly the relative permittivity of the air in those ambient conditions, we also measure it with a single pillbox cavity. Comparing the measurements of the pillbox resonant frequency, in vacuum and in air we have been able to calculate the relative permittivity of the air $\varepsilon_{r\,air}$.

$$\varepsilon_{r\,air} = (\frac{f_{0\,vac}}{f_{0\,air}})^2 = 1.0006804 \tag{4.2}$$

where $f_{0\,vac}$ and $f_{0\,air}$ are respectively the resonance frequency of the cavity in vacuum and in air. The theoretical calculation for the air relative permittivity in those ambient condition is 1.00062. For the calculation of the unloaded

quality factor of the gun, we refer to the formalism reported in [76]. First of all, we measured the loaded quality factor $Q_{L\,Al}$ of the prototype by using the bandwidth function of the VNA in transmission (Figure 4.3).

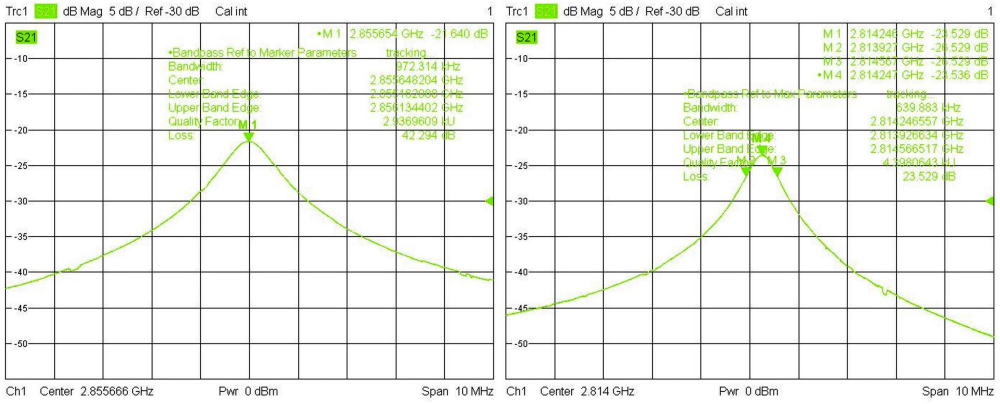

Figure 4.3: Screenshot of the Q_L measurement of the gun prototype π-mode (left) and 0-mode (right) on the Vector Network analyzer (VNA) Rohde&Schwarz ZVB 20.

Then, through the measurement of the reflection coefficient S_{11} of the prototype at the resonant frequency, is possible to calculate the coupling coefficient β using the equation:

$$\beta = \frac{Q_0}{Q_{ext}} \approx \frac{1+\rho}{1-\rho} = \frac{1+S_{11}}{1-S_{11}} \tag{4.3}$$

where Q_0 is the unloaded quality factor, Q_{ext} is the external quality factor and ρ is the reflection coefficient at the input of the gun. The measured S_{11} at resonance was equal to 380.8 mU. Therefore, by using equation 4.3 has been obtained $\beta_{Al} = 2.2$ for the anticorodal prototype. Finally the unloaded quality factor $Q_{0\,Al}$ can be derived using the expression:

$$Q_{0\,Al} = Q_{L\,Al} \cdot (1+\beta_{Al}) = 9348 \tag{4.4}$$

To compare the design unloaded quality factor of the real copper gun with those measured on the prototype, it is necessary to scale this last with the formula:

$$Q_{0\,Al} = Q_{0\,Cu} \cdot \sqrt{\frac{\sigma_{Al}}{\sigma_{Cu}}} \tag{4.5}$$

where $\sigma_{Al} = 24 \cdot 10^6\, S/m$ and $\sigma_{Cu} = 58 \cdot 10^6\, S/m$. Scaling $Q_{0\,Al}$ through equation 4.5, we obtain $Q_{0\,Cu} = 14532$ that is in good agreement with the design value. In table 4.2 are reported the results of the measurements on the prototype.

Parameter	**Measurements**
f_r π-mode	2855.65 MHz
f_r 0-mode	2814.25 MHz
β_{Al}	2.2
$Q_{L\,Al}$	2937
$Q_{0\,Al}$	9348
Frequency separations	41 MHz

Table 4.2: Results of measurements on the Anticorodal ELI-NP RF Gun prototype.

To measure electromagnetic field profile of the two modes of the RF gun, we used the perturbation method based on Slater theorem [77]. Introducing a small perturbation to the boundary condition of the mode inside the cavity, we obtain an unbalance in the stored electric and magnetic energy of the cavity. This unbalance leads to a variation of the resonance frequency of the mode and, in the hypothesis of small perturbation object, this frequency variation is proportional to the intensity of the magnetic and electric field in the position of the bead. The Slater theorem is expressed through the formula:

$$\frac{\Delta\omega}{\omega_0} = \frac{\omega_p - \omega_0}{\omega_0} = \frac{\Delta U_m - \Delta U_e}{U} = \frac{1}{4U}\int_{\Delta V} (\mu_0 H_0^2 - \epsilon_0 E_0^2) dV \tag{4.6}$$

where ω_0 is the unperturbed resonance frequency ω_p is the perturbed resonance frequency, U is the total unperturbed stored energy in the volume V, ΔU_m and ΔU_e are the magnetic and electric stored energies removed as result of the perturbation. From equation 4.6, with the hypothesis of small spherical bead the electric field on the axis of the cavity can be expressed as:

$$E^2 \approx \left| \frac{\Delta\omega}{\omega_0} \right| \frac{U}{\varepsilon \pi a^3} \tag{4.7}$$

where a is the radius of the spherical bead. A small bead is moved on the axis of the cavity while the frequency of the cavity is measured by the VNA. The bead has been dropped vertically along the axis of the gun. Figure 4.4 shown a schematic of the measuring setup.

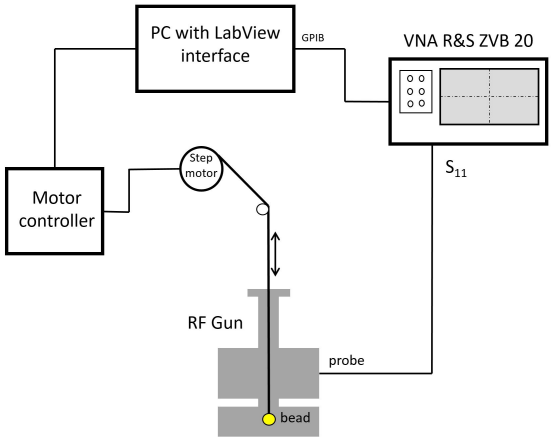

Figure 4.4: Schematic diagram of the field measuring apparatus based on the Slater theorem.

The set up used was composed by the following elements:

1. Vector network analyzer R&S ZVB 20;
2. PC interfaced with the VNA through bus GPIB (General Purpose Interface Bus) and connected to the motor controller;
3. Step motor controller IPSES;

4. perturbation bead, which is a spherical lead object, glued on a nylon wire;

5. Labview virtual instrument which allows to control the motor and to automatically acquire the signals from the VNA.

The motor was driven by the IPSES motor controller, that elaborates the strings of bit transmitted on a serial cable from a PC. It allowed to wrap or unwrap the nylon wire and so to move the bead inside the gun. To synchronize and control the motor and the VNA a Labview interface has been developed and it has been already described in Chapter 3. The resonance frequency of the cavity has been measured by the VNA as a function of the position of the bead on the axis.

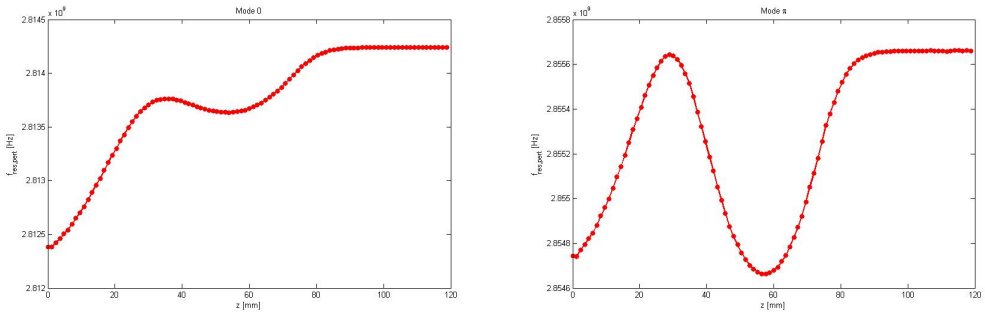

Figure 4.5: Frequency variation for the 0-mode (left) and π-mode (right) obtained with the bead-drop measurement

The profile s of the measured electric field of the π and 0 mode are given in Figures 4.6 and 4.7 respectively, As discussed in [78], from this mesurement is possible also to get the R/Q of the RF gun through the equation:

$$\frac{R}{Q} = \frac{1}{2\pi\omega_0\varepsilon a^3}\left|\int_z \sqrt{|\Delta\omega/\omega|}s(z)e^{j\omega_0 z/c}, dz\right|^2 \tag{4.8}$$

where $s(z)$ is the sign function that has to be introduced in order to recover the sign of the field, because using the Slater theorem the information on the phase of the field in a standing wave structure is lost. Using equation 4.8 we get a $R/Q = 113\Omega$. The R/Q factor is only a geometrical parameter and does not depend on the material and therefore the obtained value is consistent with

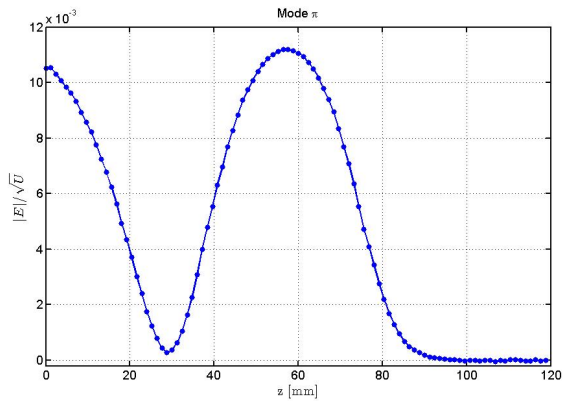

Figure 4.6: Normalized profile of the electric field of the π-mode of the RF-gun prototype.

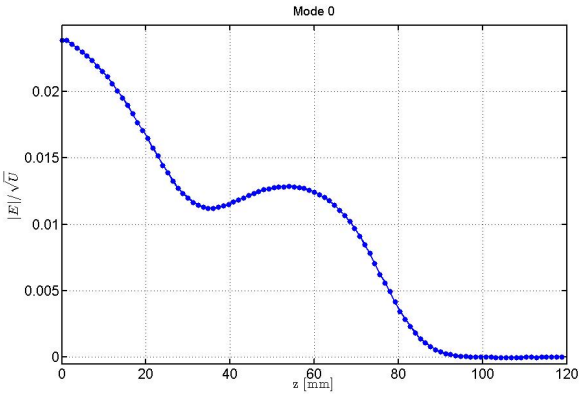

Figure 4.7: Normalized profile of the electric field of the 0-mode of the RF-gun prototype.

the design value (Table 4.1). On the basis of the good results obtained from these measurements, it has been possible to confirm the electromagnetic design of the RF gun and the overall realization process. therefore, after this test, it was possible to start the realization of the final copper device.

4.4 Structure assembly and low power tests

The machining of the different parts of the RF Gun has been done by Comeb [52]. In Figure 4.8 are showed the main components of the RF Gun before the

cleaning and assembly:

1. the cathode;
2. the closing cap with the beam tube;
3. the body, which is composed by the 1.6 cells, the aperture for RF feeding and the pumping port

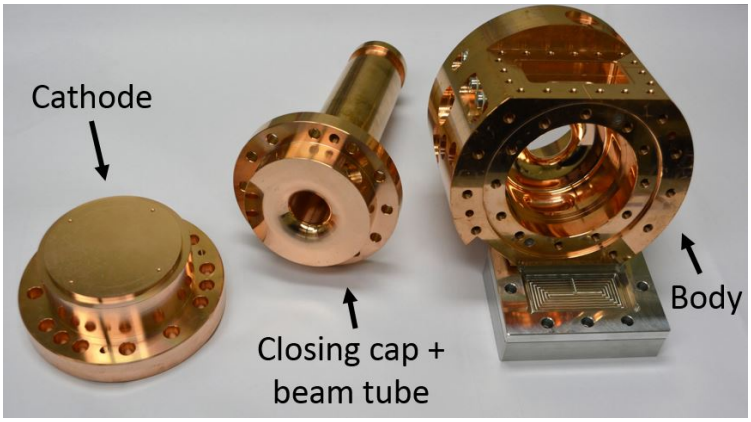

Figure 4.8: Machined parts of the ELI-NP RF Gun before cleaning and assembly.

The different components have been cleaned in a bath of Almeco (Na2 Sodium Tetraborate), a detergent, at $60°C$ with ultrasound for 30 minutes. Then they have been rinsed with raw water and deoxidized, in a bath with citric acid and ultrasound at $45°C$ for 10 minutes. Finally, they have been rinsed again with demineralized water, and have been dried with a jet of helium. The remaining water has been removed under vacuum.

The assembly procedure has been very delicate because we had to check the right compression of the gaskets to guarantee the right inside dimensions of the cells and the absence of leaks. In order to verify the quality of the RF contacts and the right compression of the gasket at the cathode, the quality factor of the gun working mode was monitored during the clamping procedure. Before the low power measurements a vacuum test with He leak detector demonstrate the complete sealing of the device. In Figures 4.9 and 4.10 are reported some steps of the cleaning process and the structure during the assembly procedure.

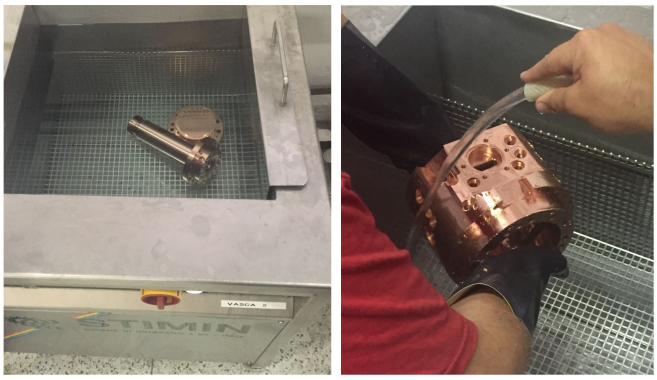

Figure 4.9: Pictures of the cleaning procedures of the machined parts.

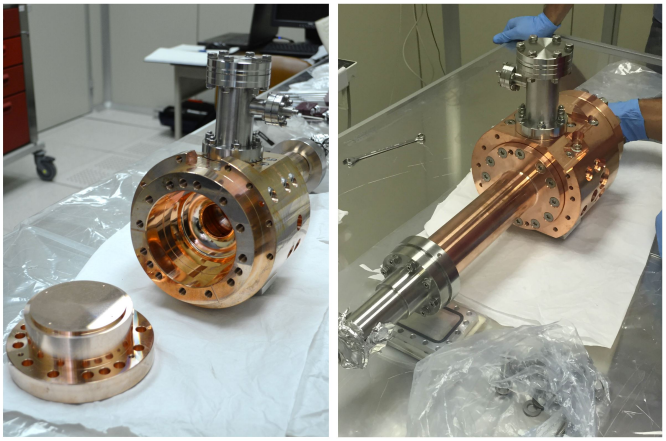

Figure 4.10: ELI RF-Gun during the assembly procedure.

The main goal of the low power RF tests was the complete characterization of the cavity at the nominal working conditions. Since the nominal working temperature of the device is $34°C$ in vacuum, a frequency scaling has been made in order to assess the realistic performances of the cavity. Temperature, humidity and air pressure were constantly monitored, and the measurement frequency has been corrected according to these parameters, as it was done for the prototype. Both resonant modes have been measured and characterized. All the measurements have been done with a room temperature of $T_{air} = 22.9°$C, a cavity temperature of $T_{cav} = 21.8°$C, atmospheric pressure of $P = 995.2$ hPa and a humidity of $H = 52.4\%$. In this condition the π-mode working frequency has been calculated to be $f_\pi = 2.855617$ GHz. The first measurement of the

working resonant frequency give us $f_\pi = 2855.77$ MHz that is 600 kHz higher than the nominal one. This detune has been confirmed also through field flatness measurement using the bead-drop measurement and, consequently, using a bidirectional tuner the volume of the entire cell has been slightly increased. After this tuning the new resonant frequency measured for the working π-mode was $f_\pi = 2855.62$ MHz. In Figures 4.11 and 4.12 are shown the reflection coefficient and the transmission coefficient measured at the gun after the tuning.

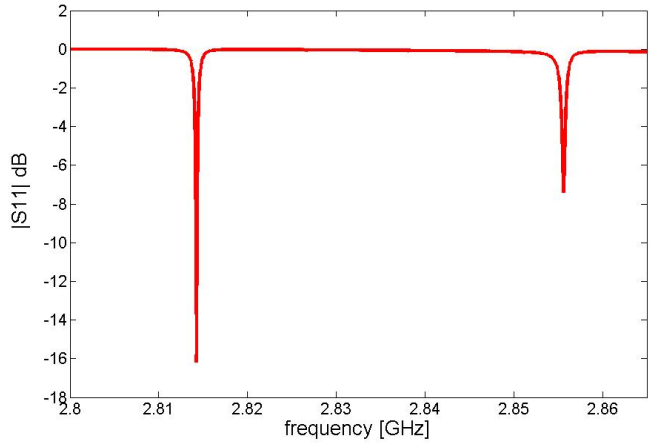

Figure 4.11: Reflection coefficient measured at the input port of the gun. Both resonant modes are shown.

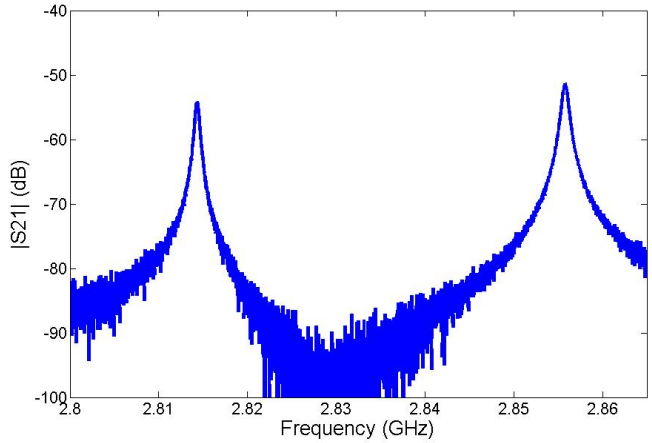

Figure 4.12: Transmission coefficient measured with a RF probe inside the gun.

From the reflection and transmission coefficients all the RF parameters have been measured. The resonant frequency of π-mode is $f_\pi = 2.85562GHz$ with a $S_{11} = -6.9dB$. The coupling coefficient is $\beta = 2.64$, the loaded quality factor $Q_{loaded} = 4115$ and the unloaded quality factor is Q_0=14980. The 0-mode instead has a resonant frequency at $f_0 = 2.81426GHz$, a reflection coefficient $S_{11} = -15.6dB$ with a coupling coefficient $\beta = 1.4$, finally the mode separation is $\Delta f = 41MHz$. Finally, to perform the electric field profile in the two cells of the gun the bead-drop measurement has been performed with the same set-up described in the previous section, inserting a lead sphere (2 mm radius) fixed on a thin nylon wire (0.1 mm radius) through the beam pipe of the gun. The results for the two resonant modes, after the tuning, are reported in Figure 4.13 and Figure 4.14, while Table 4.3 summarizes all the measured parameters of the ELI-NP gun.

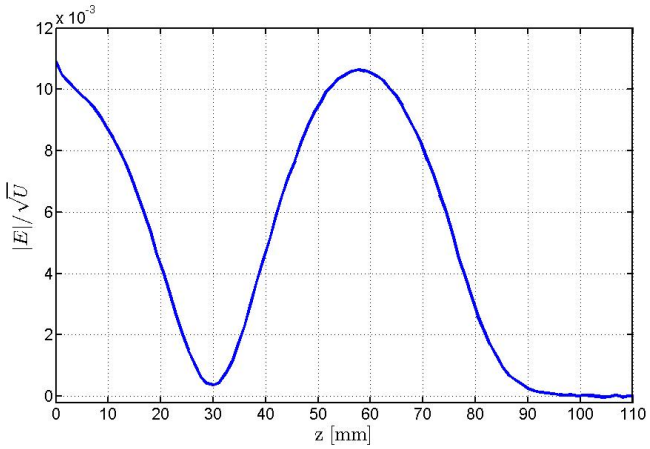

Figure 4.13: Normalized profile of the electric field of the π-mode of the ELI RF Gun.

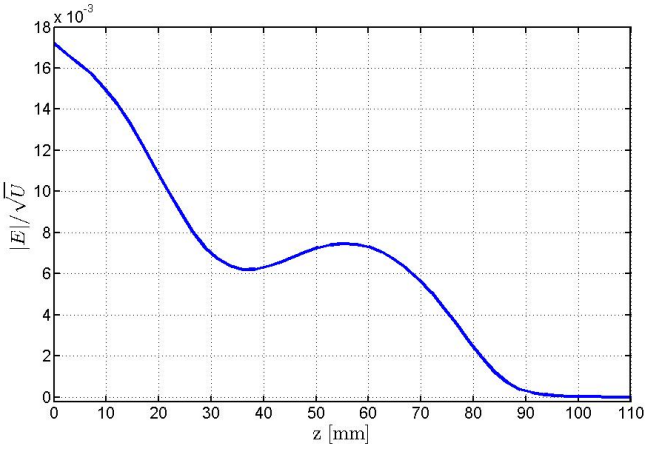

Figure 4.14: Normalized profile of the electric field of the 0-mode of the ELI RF Gun.

Parameter	π**-mode**	**0-mode**
f_{res}	2855.62 MHz	2814.26 MHz
$S_{11}@f_{res}$	-6.9 dB	-15.6 dB
Coupling coefficent β	2.64	1.4
Q_{loaded}	4115	
Q_0	14978	
mode separation (Δf)	41 MHz	

Table 4.3: ELI-NP RF Gun measured parameters.

4.5 High power test

After vacuum test and complete RF characterization at low power, the RF Gun has been tested at high power. The conditioning of the device has been conducted in the ELSA facility at the University of Bonn under the responsibility of Research Instrument GmbH (RI) [59]. In Figures 4.15 and 4.16 are showed a schematic and some pictures of the gun installation set-up.

As it is possible to see in the pictures, the experimental setup of the test area was composed by the following elements:

1. LLRF system (signal generator and switch),

2. 60MW RF Source,

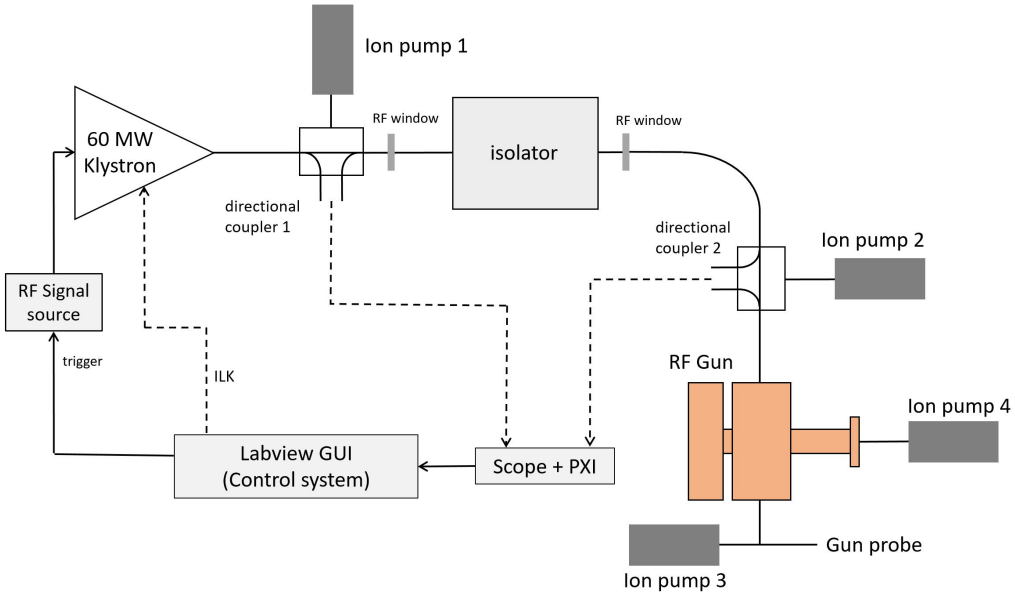

Figure 4.15: Schematic diagram of the high power RF test set-up in the ELSA facility (Bonn, Germany).

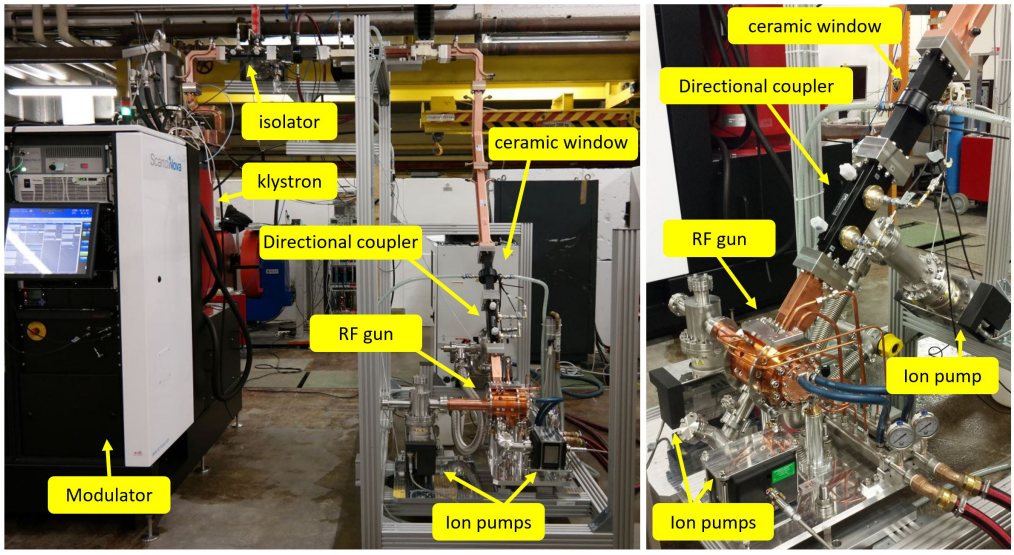

Figure 4.16: Picture of the high power RF test set-up (Left) with a detail of the RF Gun (right).

3. Radiofrequency SF6 WR284 isolator,

4. Two RF ceramic windows,

5. Two directional couplers (DCs),

6. Four vacuum ion pumps,

7. Chiller for gun cooling.

The gun has been fed by the nominal ELI-NP power sources: K2-3 Scandinova modulator adapted for a 60MW S-band Toshiba klystron E37314 (described in 2.3). The source includes also the RF amplifier, which amplify the LLRF signal to the klystron input. During the conditioning, the RF power into the gun has been increased keeping constant the LLRF signal (0dBm) and increasing the voltage of the modulator. Hence, before the test, the output power of the klystron connected to an RF load has been measured as function of the modulator CCPS voltage (as reported in Figure 4.17).

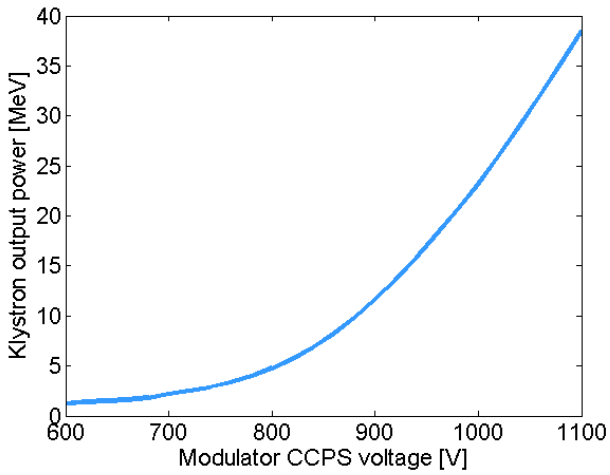

Figure 4.17: Output power of the S-band klystron measured through a power meter as function of the capacitor charging power supply voltage of the modulator.

The low power RF signal that fed the RF amplifier is generated by a LLRF system composed by a 3 GHz signal generator combined with an RF switch. An isolator was inserted between the klystron and the Gun to protect the klystron from the reflected power. The working temperature of the Gun was stabilized by a thermo-chiller. The isolator and vacuum ceramic windows were also water cooled and all the cooling system was controlled through flow switches.

Different signals were monitored during the conditioning procedure. The forward/reflected power signals were available at two directional couplers (DC1 and DC2), the first placed just after the klystron and the second at the gun input. These signals, together with the gun probe, have been measured using peak detector diodes and an oscilloscope. In Figure 4.18 are reported the signals monitored through the oscilloscope during the conditioning procedure: Forward power signal from DC1, forward and reflected power signal from DC2 and the gun probe signal, that gives informations about the field level inside the gun.

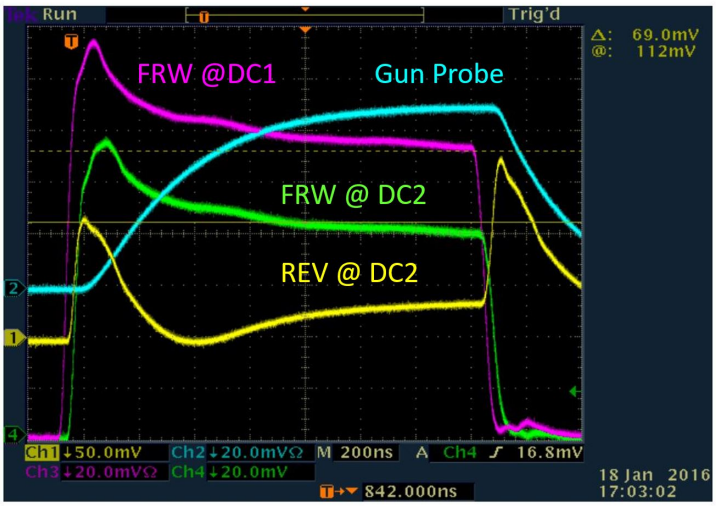

Figure 4.18: Typical signals monitored at the directional couplers and the gun probe during the ELI-NP RF gun conditioning: Forward signal at the output of the klystron (Magenta), forward signal at gun input (Green), reflected signal at the gun input (Yellow) and signal at the gun probe (Cyan).

All these readings were recorded by means of a Labview interface which calculates the corresponding power levels taking into account the provided signal attenuation and calibration curves of the diodes. To be sure of the correct feeding of the Gun and trust the read value on the interface, the oscilloscope measurements at the different pick ups (DC1 forward, DC2 forward, DC2 reverse and Gun probe) have been cross checked with those taken through a calibrated power meter.

The control system realized through this Labview interface, was monitoring also the vacuum levels and generated the trigger signal and the vacuum and

temperature interlock signals. Moreover it allowed to the operator to control the hardware to increase the power and the length of the RF signal. A log file reporting all the acquired data was generated every minute and at each interlock occurrence.

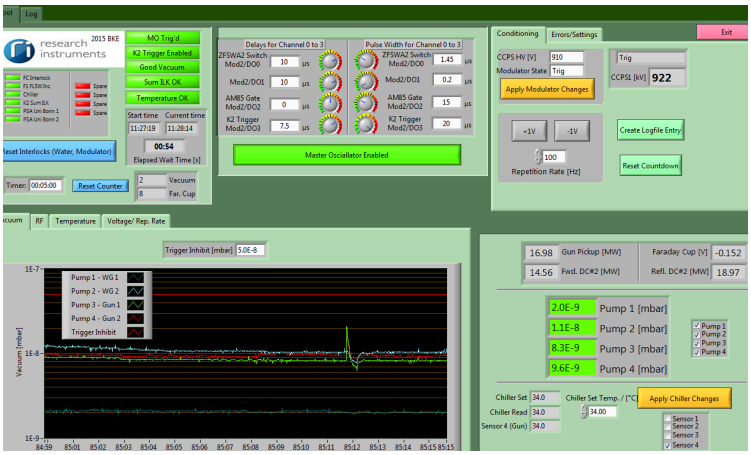

Figure 4.19: Control system programmed in Labview (Courtesy of Research Instrument GmbH [59]).

The current absorption of four ion pumps were monitored throughout the whole process, one was connected after the klystron, two at the gun input/output and the last one was connected to the pumping port opened in the gun full cell. Changing in vacuum levels are indication of discharges inside the device under test. If the ion pumps current absorption exceeded a threshold, corresponding to a pressure of $1 \times 5 \cdot 10^{-8}$ mbar, an interlock occurs and the control system stops triggering the LLRF signal and the modulator. For this test an additional fast breakdown detector system has been implemented through a standalone fast digitizer system in order to generate interlock that stop the RF signal in the shortest possible time after a breakdown event. It consisted in a shape monitor of the reflected signal at the gun input, realized through a mask. That mask (showed in Figure 4.20) allowed to detect shape distortions of the monitored signal. Hence, this system was able to detect breakdowns or discharges four times faster then the interlock on the ion pumps current absorption. Therefore it prevents gun damages in a more reliable way with respect to the vacuum threshold interlock.

In summary, an interlock signal could be generated by:

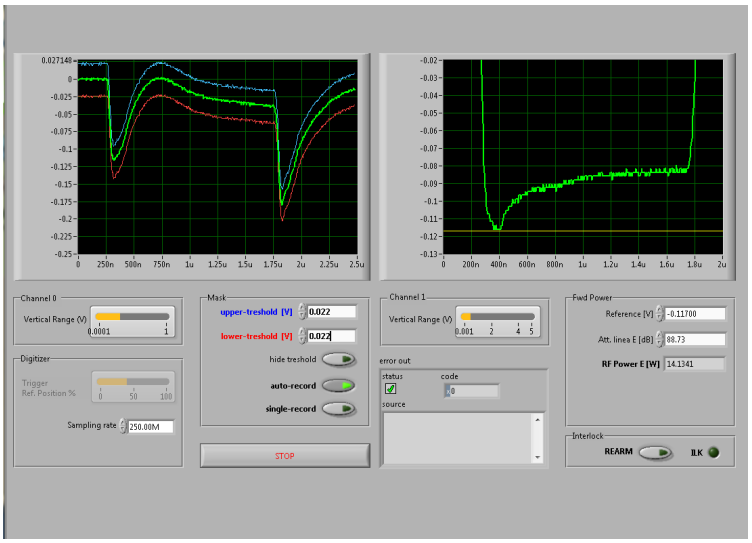

Figure 4.20: Mask shape comparator used as discharge detector during the gun conditioning.

- An operator, directly from the Labview GUI;
- The interlock on the vacuum threshold;
- Modulator internal interlock;
- Temperature and cooling system interlock;
- Shape monitor on the reflected power signal at the gun input.

The RF conditioning test had two main goals. The first goal was to reach 15 MW (pulsed), 100 Hz repetition rate and $1\ \mu s$ pulse length, in order to reach an electric peak field on the cathode equal to 120 MV/m, the second was to reach a peak pulse power of 14 MW, 100 Hz repetition rate and $1.5\ \mu s$ pulse length. The procedure started with a short pulse (200 ns), 10 Hz repetition rate and minimum power. The power was increased with steps of about 0.5 MW according to the experimental observation. Reached the nominal power, the pulse length was increased of 200 ns, the repetition rate and power restored to the starting values and the procedure was repeated.

During the conditioning the optimum operating temperature of the gun has been determined. The signal generator frequency was swept to maximize the

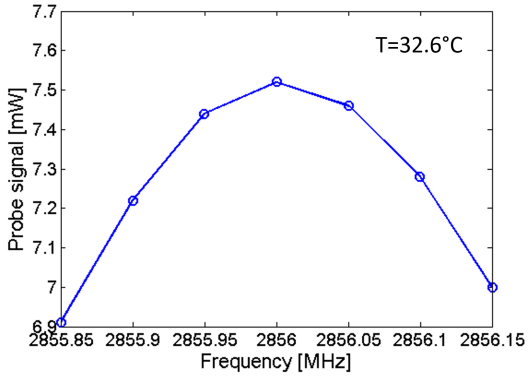

Figure 4.21: Measurement of the gun probe signal as function of the signal generator frequency at the optimum gun temperature.

pick up signal at a stable RF input pulse level. From the frequency deviation the optimum gun temperature $T = 32.6°C$ has been determined. In Figure the measurement of the resonance frequency sweep at the optimum gun temperature is reported.

Full parameter have been achieved in about 150 hours of conditioning with overall extremely good performances. In Figure 4.22 the behavior of the RF pulse length input power and repetition rate as a function of time are reported. The vacuum levels was $1.6{\cdot}10^{-9}$ mbar at DC1 and $1{\cdot}10^{-8}$ mbar at DC2, $7.9{\cdot}10^{-9}$ mbar at the gun cavity and $8.3 \cdot 10^{-9}$ mbar at the beam tube. Figure 4.23 shows the vacuum pressure measured by the three ion pumps current absorption as a function of the conditioning time. The reached breakdown rate at the end of the conditioning process was of the order 10^{-6} bpp. In table 4.4 the results of the ELI-NP gun RF conditioning are reported.

Parameter	**Value**	**Unit**
Peak power	14.6	MW
Repetition Rate	100	Hz
Pulse length	1.5	μs
Breakdown rate	$1 \cdot 10^{-6}$	bpp/m
Gun vacuum pressure	$7.9 \cdot 10^{-9}$	mbar

Table 4.4: Results of the ELI-NP Gun conditioning test.

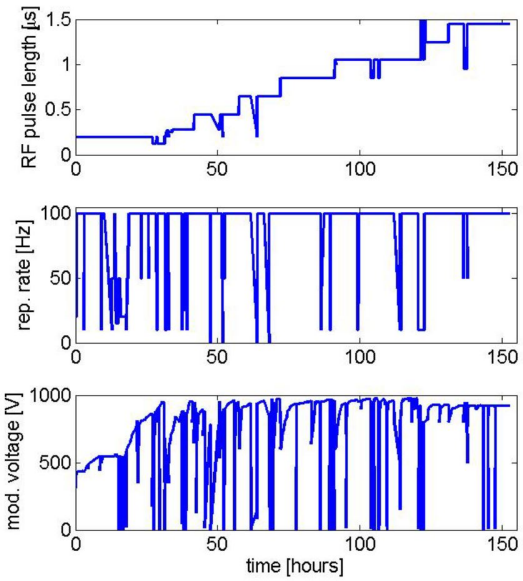

Figure 4.22: Behavior of the RF Pulse length, input power and repetition rate as a function of time during the high power test of the ELI-NP RF Gun.

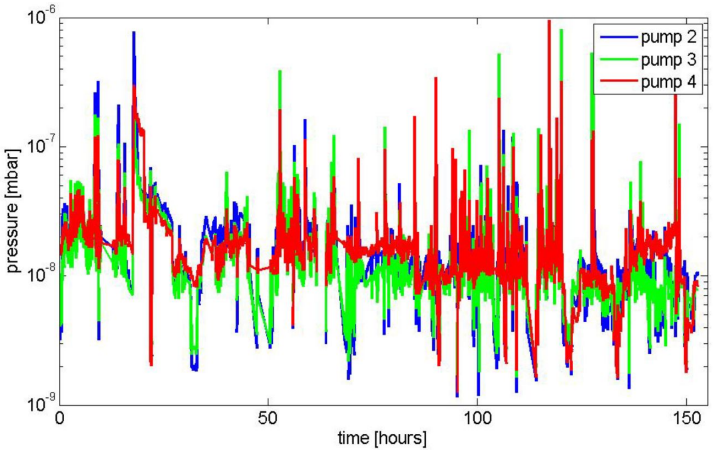

Figure 4.23: Vacuum pressure as a function of the conditioning time during the high power test of the ELI-NP RF Gun.

CHAPTER

5 Linac with the Gaskets Clamping Technique

Content

5.1 Gasket Clamping technique

There is a growing demand from the research and industrial communities for compact and high gradient RF accelerating structures in order to obtain energetic and high brightness beams. Generally, these structures are manufactured

by machining the different components through high precision lathes and/or milling machines. Then these copper components are joined together by brazing. The brazing process is a metal joining process in which two metal parts are bonded together by melting an alloy that, at high temperature (typically above 800-900$^{\circ}C$), flows into the gaps between the parts to join, by capillary action. At each step of brazing a lower melting point alloy has to be used in order to avoid breaking of previous brazing. Typical copper alloys are 25%Au / 75%Cu, 35%Au / 65%Cu, and 50%Au / 50%Cu. To avoid oxidation throughout this process, big and expensive vacuum furnace are used. This process increases the copper ductility reducing its hardness (copper annealing) and during each brazing step the parts undergo high mechanical and thermal stresses ($> 800^{\circ}C$) due to the high temperature.

Summarizing the brazing process presents several drawbacks:

- the risks of failure of the brazing is not negligible (vacuum leaks, damages, etc.);
- it requires large vacuum furnace available available in few companies or laboratories;
- only few companies around the world can afford it;
- in general, it is expensive;
- at the end of the process the copper is ”soft” since it has lost its mechanical hardness.

Furthermore, breakdown-rate studies (BDR) in X-band indicated that, avoiding the copper annealing associated with the high temperatures involved in the brazing process the BDR probability can be reduced [75]. For all these reasons, a new fabrication method, called gasket-clamping technique, has been developed at the INFN-LNF laboratories [74]. It allows avoiding the brazing process in the structure fabrication by using special RF-vacuum gaskets to join the different machined parts. Hence, these parts are simply clamped together by means of screws radially disposed around the cells. As discussed in previous chapter this technique has been successfully applied for the realization of both the new

SPARC_LAB 1.6 cells RF gun [73] and the ELI-NP-GBS one, presented in this work. The extremely good results obtained for these devices in terms of reached cathode peak field and low BDR, open the possibility to apply this technique to more complicated RF structures. In particular, the possible application of this technique, in the realization of an entire TW Linac structure, has been investigated with the design of a S-band structure prototype [79]. The goal of the design and realization, of this prototype, is to demonstrate the feasibility of this technique for the realization of an entire Linac structure. This approach can have also a strong economic and industrial impact worldwide, since, in principle, all Companies that are able to machine with high precision copper components, will be able to fabricate a Linac structure.

In this chapter the design of the S-band TW structure is presented, putting in evidence the deep connection between mechanical constraints and electromagnetic parameters. The prototyping phase and the realization of this structure consists in different steps and the recent results are finally reported.

5.2 Electromagnetic design of the S-band prototype

In the design two aspects have to be considered: the electromagnetic design and the mechanical design of the structure. A continuous feedback between these two aspects is necessary since they are strongly interconnected in particular for this kind of structure.
The prototype, we have designed, is a 10 cell S-band TW structure with constant impedance and $2\pi/3$ field phase advance per cell. The S-band frequency as been chosen, in order to relax the machining tolerances needed for the realization of the different parts and speed up their production. All the electromagnetic simulation have been done with the 3D electromagnetic code Ansys HFSS [80]. The electromagnetic design of the S-band TW prototype can be summarized in three main steps: single cell design, input/output coupler design and power splitter design.

Cell design

There are analytical expressions that bond the geometrical dimensions of the cell to the fundamental parameters of the field that propagate in a periodic TW structure [57]. The final dimensions and shape of the single cell (reported in Figure 5.1) has been optimized to obtain a low peak electric field on the irises, an average accelerating gradient comparable with the one of a commonly used SLAC type S-band structure (25 MV/m) and a relatively high group velocity.

All the geometrical dimensions of the single cell have direct impact on the RF performances. In particular, the aperture radius a strongly affects the group velocity and the shunt impedance of the structure. The aperture radius has been chosen as large as possible in order to guarantee an high acceleration efficiency and, at the same time, low power dissipation on the cavity wall, short filling time and a good pumping speed. The short filling time, $\tau_F = L/v_g$, allows using short RF pulses, thus reducing the BDR [75].

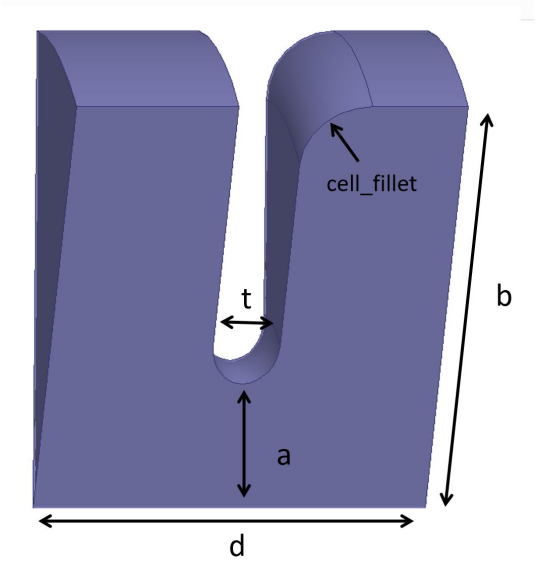

Figure 5.1: Model of the single S-band cell with Ansys HFSS.

The phase velocity of the field propagating inside the travelling wave structure has to be equal to the particle velocity (that in case of electrons is constant and equal to c) [57]. This fix the cell length for a given working frequency and phase advance ($\frac{2\pi}{3}$ at 2.856 GHz, in our case). According to the formula

$\beta \cdot z = \frac{\omega}{c} \cdot z = \frac{2\pi}{3}$ we obtain a cell length $d = 34.99$ mm. The disk thickness t has been chosen equal to 6 mm to ensure a good mechanical strength of the structure and a good coupling between the different cells.

In Appendix A a brief summary of the main figures of merit of the single cell of a travelling wave structure is reported. In order to find a good compromise for the choice of the iris half aperture dimension a, these figures of merit have been calculated and plotted considering a variation step of the iris equal to 1 mm. For each value of the iris, the outer cell radius has been tuned to resonate at the nominal working frequency. Because of the 2D symmetry of the cell TM010-like accelerating mode, it has been possible to simulate a portion of the cavity (30 degrees in our case) with the proper perfect H boundary conditions, thus reducing the computational time.

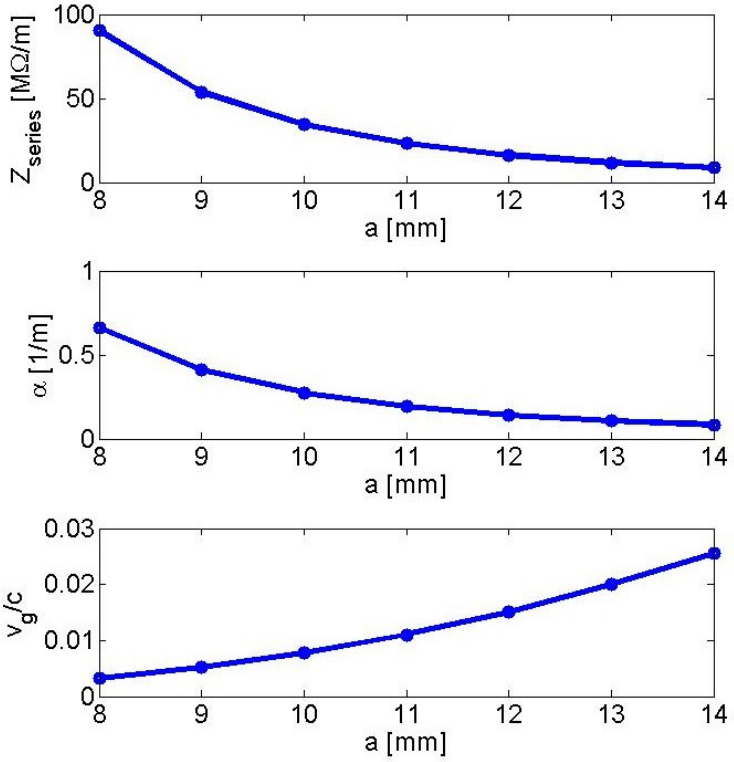

Figure 5.2: Main figures of merit of the single cell as a function of the iris aperture.

Figure 5.2 reports the results of the parametric analysis in terms of series impedance, attenuation factor and group velocity as a function of the iris half

aperture a. Since the prototype is a Constant Impedance (CI) section with equal cell irises, an half aperture of 13 mm has been finally chosen as the best compromise between all structure parameters. A CI structure with all equal cells allows simplifying the mechanical design and the realization. To decrease the peak surface electric field on the irises, an elliptical cross-section shape with an aspect ratio 4/3 has been chosen. This guarantees a reduction of the surface field of the order of 10% with respect to the round profile, which is desirable for high gradient application.

In the final configuration of the cell, one of the internal edges has been rounded with a fillet radius equal to 3 mm, both to increase the quality factor (of about a factor 10%) and to simplify the mechanical realization of the cell cups, avoiding sharp edges. The cell phase advance and the frequency sensitivity for different geometrical parameters of the cell are reported in Table 5.1. From these quantities it is possible to extrapolate the maximum tolerances of fabrication and how to correct errors with a proper cell tuning.

Parameter	**Frequency sensitivity**	**Cell phase advance sensitivity**
Cell radius	-73 kHz/μm	-0.15 deg/μm
Iris half aperture	22 kHz/μm	0.05 deg/μm
Cell length	-5 kHz/μm	-0.01 deg/μm
Iris thickness	10 kHz/μm	-0.02 deg/μm

Table 5.1: Frequency and cell phase advance sensitivity with respect to the cell main parameters

To conclude the single cell analysis also the dispersion curve has been calculated and is reported in Figure 5.3.

Coupler design

There are different possible geometries to realize a coupler for travelling wave structures [76] but the need to implement the clamping gasket technique limited the possible choices. Two main requirements are responsible of this limitation: first, the necessity to design the coupler cell with a geometry that allows the insertion of a closed gasket to seal the coupler cell itself, second the necessity

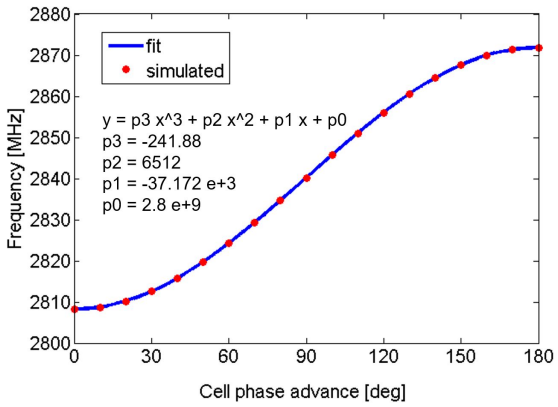

Figure 5.3: Dispersion curve for the designed cell and polynomial fit.

to insert the screws around the coupler cell as close as possible to the gasket in order to compress it with a uniform pressure. In particular, it was not possible to adopt a standard z-coupling coupler used in general for TW structure (such as the SLAC type structure [81]), because it makes unfeasible the placement of a gasket between the coupling cell and the adjacent cell. For these reasons the coupler has been realized through a coupling aperture (see Figure 5.4) directly machined on the coupling cell wall. This aperture consists in a rounded slot opened between the coupling cell and the waveguide. Its dimensions have been optimized to match the waveguide mode TE10 to the accelerating one TM01-like. The surfaces of that slot have been strongly rounded to reduce the pulsed heating and the coupling cell has been designed with a racetrack shape to facilitate its machininig and for field distorsion compensation, both this aspects will be discussed in detail in 5.2.

One of the main mechanical constraints in this design was to keep the transverse dimension w of the coupling slot as small as possible to reduce the distance between the clamping screws. For this reason and in order to make symmetric the feeding avoiding dipole kicks a dual feed scheme has been implemented. Finally, in order to insert two screws near to the aperture, the thickness t_c has been chosen larger than the diameter of the screws we adopted and has been fixed equal to 16 mm.

The main goal of the coupler tuning is to minimize the reflected power at the input/output coupling port of the structure. This can be done through different

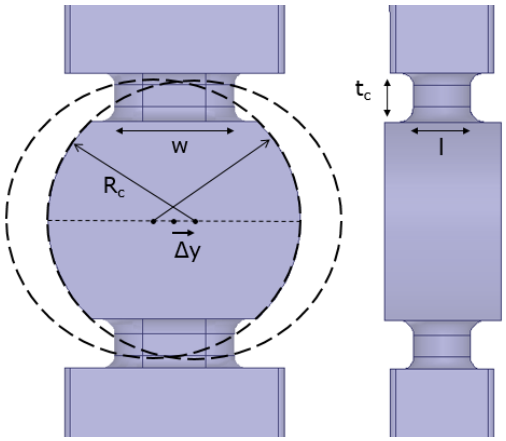

Figure 5.4: Sketch of the front view (left) and lateral view (right) of the input/output coupler.

techniques. The geometrical parameters used for the tuning depend on the kind of coupler and in our case the most effective are the slot width (w), the length (l) and the radius of the coupling cell (R_c).

By electromagnetic codes it is possible to simulate with input and output coupler and few number of cells. In this case the coupler is designed modifying the dimensions in order to minimize the reflection coefficient at the input but also, verifying that the phase advance per cell of the TW structure is constant and equal to the nominal one ($2\pi/3$ in our case). Obviously, the only condition on the reflection coefficient is not sufficient, because one can have a very low reflection coefficient due to a combination of reflected waves from the input and output coupler that compensate each other. This procedure is very time consuming and require the full simulation af a structure with both couplers and few cells. There is another technique [82] that allows reducing the computational time.

This technique is based on the modeling of the coupling cell as a two port network with scattering matrix $[S]$ as shown in Figure 5.5).

Using the transmission line formalism, we obtain that, a perfectly matched coupler must have the first element of the scattering matrix S_{11} equal to zero. By closing the circuit represented in Figure 5.5, after a certain number of cells n, with a short circuit (i.e. a perfect electric wall) and neglecting the losses, is possible to demonstrate the following relation [82]:

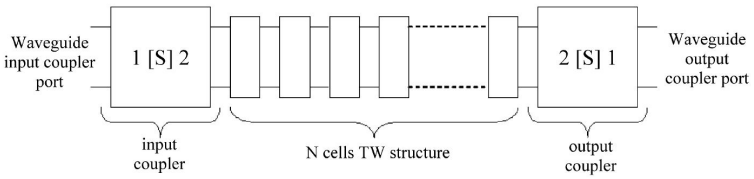

Figure 5.5: Equivalent circuit model of the TW structure with couplers.

$$S_{11} = 0 \longleftrightarrow \frac{\Gamma_s(n+2)}{\Gamma_s(n+1} = \frac{\Gamma_s(n+1)}{\Gamma_s(n)} = e^{-j2\phi} \tag{5.1}$$

with $|\Gamma_s(n)|= 1$. In that relation $\Gamma(n)$ is the reflection coefficent at the coupler input port when the structure is short circuited (n is the position of the short-circuited cell) and $-\phi$ is the phase advance per cell in the TW structure. This theorem is valid for a structure operating at any frequency and for each operating mode. Equation 5.1 can be combined with the simulation of three corto-circuited structures (n=1,2,3 see Figure 5.6) and guarantee that the S_{11} of the coupler is equal to zero only if are verified the conditions:

$$\angle\Gamma(2) - \angle\Gamma(1) = -240^\circ \tag{5.2}$$

$$\angle\Gamma(1) - \angle\Gamma(0) = -240^\circ \tag{5.3}$$

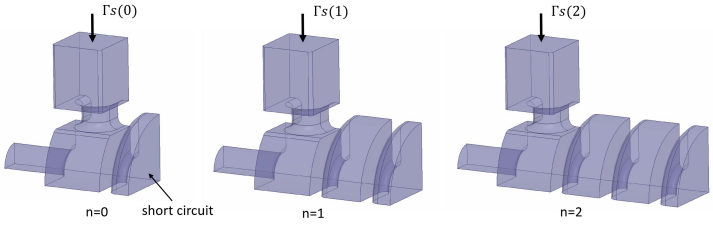

Figure 5.6: HFSS model of short circuited cells for coupler matching.

moreover is possible to plot directly the $|S_{11}|$ as function of $\Gamma(n)$ through the relation valid under the condition of small $|S_{11}|$ and demonstrated in [82]:

$$|S_{11}| \cong \frac{1}{2(\sin(\phi))^2}\sqrt{\frac{(\theta_{21}+\theta_{10})^2}{4(\cos\phi)^2} + \theta_{10}^2 - \theta_{10}(\theta_{21}+\theta_{10})} \tag{5.4}$$

where θ_{10} and θ_{21} are the phase distortions at the waveguide input due to a non-ideal coupler:

$$\theta_{10} = \frac{\angle[\Gamma_s(1)/\Gamma_s(0)]}{2} + \phi \tag{5.5}$$

$$\theta_{21} = \frac{\angle[\Gamma_s(2)/\Gamma_s(1)]}{2} + \phi \tag{5.6}$$

Starting from the wrong dimensions of the coupler through the conditions 5.3 and the equations 5.4 is possible to evaluate the $|S_{11}|$ of the coupler and understand how to modify these dimensions. To this purpose a simple iterative algorithm has been developed and used in our case. By naming $\varphi_{21} = \angle\Gamma(2) - \angle\Gamma(1)$ and $\varphi_{21} = \angle\Gamma(1) - \angle\Gamma(0)$ is possible to define:

$$\Delta\varphi_{21} = C_1 \cdot \Delta R_c + C_2 \Delta w \tag{5.7}$$

$$\Delta\varphi_{10} = C_3 \cdot \Delta R_c + C_4 \Delta w \tag{5.8}$$

$$C = \begin{pmatrix} C_1 & C_2 \\ C_3 & C_4 \end{pmatrix} \tag{5.9}$$

where the elements of the matrix C are the partial derivatives of $\Delta\varphi_{21}$ and $\Delta\varphi_{21}$ and can be calculated using the expressions:

$$C_1 = \frac{d\varphi_{21}}{dR_c}|_{dw=0} \tag{5.10}$$

$$C_2 = \frac{d\varphi_{21}}{dw}|_{dR_c=0} \tag{5.11}$$

$$C_3 = \frac{d\varphi_{10}}{dR_c}|_{dw=0} \tag{5.12}$$

$$C_4 = \frac{d\varphi_{10}}{dw}|_{dR_c=0} \tag{5.13}$$

inverting the square matrix C is possible to derive the variation that must be applied at the starting dimensions by:

$$\begin{pmatrix} \Delta R_c \\ \Delta w \end{pmatrix} = C^{-1} \cdot \begin{pmatrix} \Delta\varphi_{21} \\ \Delta\varphi_{10} \end{pmatrix} \tag{5.14}$$

where $\Delta\phi_{21} = -240 - \phi_{21}$ and $\Delta\phi_{10} = -240 - \phi_{10}$. Summing the starting values of R_c and w to the deviations ΔR_c and Δw, is possible to find the new coupler dimensions. After having calculated the phase differences of the reflection coefficients with the new dimensions, this procedure must be applied again until the conditions 5.3 are verified with a maximum error of $\pm 1^\circ$ (that corresponds to a reflection coefficient $< 35\, dB$). In our case this algorithm has been applied only in the final optimization and fine tuning of the coupler. As already said, because we have to keep as small as possible the length w of the coupler, we fixed that parameter and use the length l (see Figure 5.4) and the coupling cell radius R_c for the optimization. An initial rough indication on these dimensions have been obtained using the formula for the $|S_{11}|$ reported in [82], then the described algorithm has been applied. The plot of $|S_{11}|$ as function of R_c and l in combination with the plots of the two surfaces given by equations 5.3, has been used to get information about the directions towards the right values for the two optimum parameters. For the fine tuning of the coupler the algorithm has been applied with increments ΔR_c and Δl equal to 0.005 mm. In Figure 5.7 the final $|S_{11}|$ is reported.

Finally, a fine tuning ($\sim 1\mu m$) of the couplers dimensions has done simulating the entire structure with the two couplers and a reduced number of cells (7). This fine tuning has been performed minimizing the S_{11} and checking at the same time the field flatness and the cell-to-cell phase advance. In this way, also the second order effects, neglected in the tuning algorithm (evanescent fields at the coupler, losses etc), have been taken into account.

The final dimension of the coupler are $R_c = 42.25\, mm$, $l = 18.235\, mm$ and $w = 21\, mm$, from Figure 5.7 is possible to see that in that point there is a minimum for the reflection coefficient of the coupler. The results of the simulations of the final configuration are reported in 5.2.

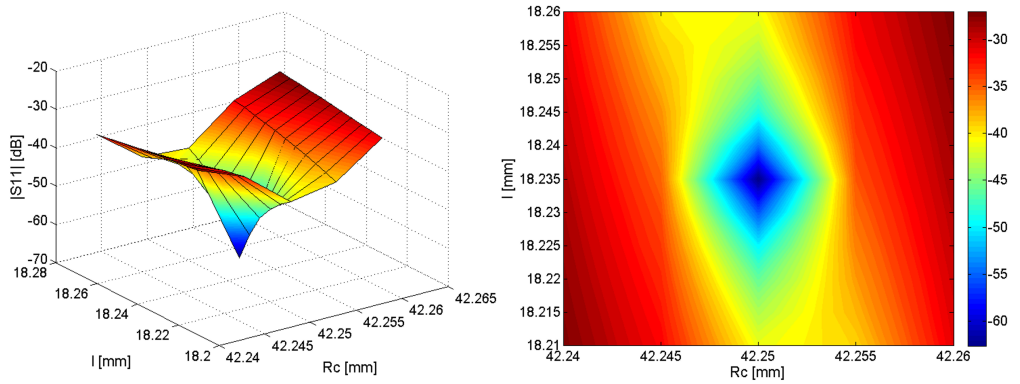

Figure 5.7: 3D plot (left) and 2D plot (right) of the $|S_{11}|$ as function of the coupler cell radius R_c and the aperture length l.

Compensation of multipole field distorsion and calculation of the pulsed heating

In an ideal closed pillbox the accelerating mode TM01-like is characterized by an azimuthally symmetric magnetic field which is zero at the center and maximum on the cavity wall. According to [76] coupling slots in the cavity wall introduce distortions in the field distribution and multi-pole components of the magnetic field can appear on the beam axis and affect the dynamics of the beam. These effects are more important in the design of an RF Guns, as example, because of the relatively low energy of the electron beam but, if not well compensated, can affect also the dynamic of an electron beam passing through the coupling cavity of an accelerating structure.

The use of a symmetric dual feeding automatically avoid the presence of dipole components and all odd components. Nevertheless even field components such as quadrupole, octupole, etc. have to be compensated.

As already pointed out, in our case, to simplify the machining the coupler cell has been designed with a racetrack shape, as given in Fig. 5.4. The use of a racetrack shape also allows to easily compensate the quadrupole field components induced by the presence of the two hole apertures. In particular the displacement Δy, between the centers of the two circumferences which describes the coupling cell, has been optimized to compensate the quadrupole component.

With a displacement Δy equal to $2mm$ the quadrupole component has been completely compensated. In Figure 5.8, as an example, the magnetic field on a circle of 5 mm radius in the center of the coupler has been reported for a circular cell and for a racetrack shape with different Δy. From the plot it is possible to see that with a displacement of $2mm$, in the negative directions, the quadrupole component is compensated.

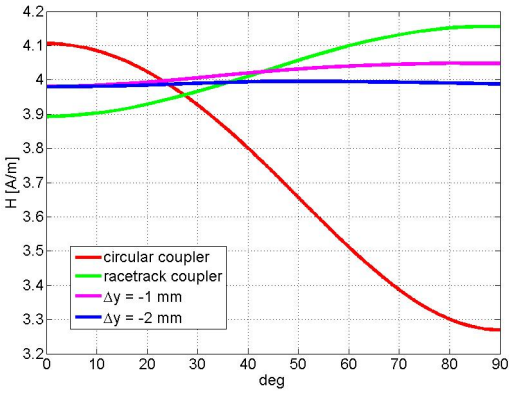

Figure 5.8: Azimuthal magnetic field at 5 mm from the center of the coupler cell for different geometries of the cell.

Slots and apertures, like the aperture of the coupler or the iris of the accelerating structures, are place where the surface currents flowing along the edges of them can reach very high density. These high currents can give localized losses and create hot spots that can lead to dangerous breakdown effects. The cause of this phenomena is known as pulsed heating and has to be carefully evaluated and monitored in each place of the designed structure where there are high surface currents (i.e. high magnetic field). In our design the coupling hole has been strongly rounded to reduce pulsed heating on the surfaces. A fillet of 5 mm on one side and 4 mm on the other has been applied to the coupling hole. As reported in [76] and [75], in order to evaluate the pulsed heating, the following formula, valid in case of copper structures, can be used:

$$\Delta T[^{\circ}C] = 127|H_{\parallel}[MA/m]|^2\sqrt{f_{RF}[GHz]}\sqrt{t[\mu s]} \tag{5.15}$$

Experimentally, if the temperature increasing due to pulsed heating is above $50^{\circ}C$ the probability of coupler damages due to pulsed heating increases. The

surface magnetic field on the coupler has been calculated using HFSS and it is reported in Figure 5.9. The temperature increase due to pulsed heating on the coupler is $< 17°C$ for an RF pulse of $1\mu s$, while on the regular cell iris, it has been evaluated $< 2°C$.

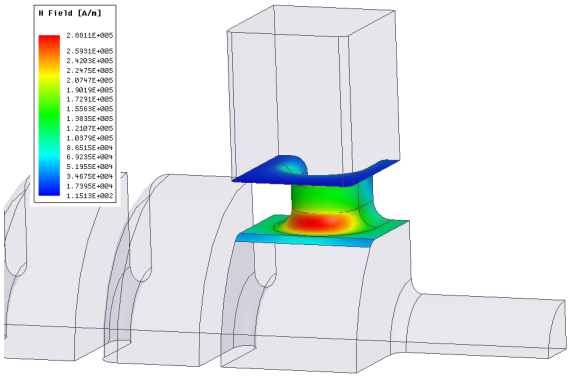

Figure 5.9: Surface magnetic field on the coupling aperture of the coupler.

Splitter design

As described in the previous section the input coupler presented uses the double symmetric feeding scheme in order to keep small the coupling aperture and to compensate the dipole magnetic field component. In the final implementation of the system for the high power tests a splitter will be inserted on the input coupler to guarantee the correct phase between the two ports while the output ports will be connected to two RF loads. The splitter is composed by a 3dB power divider which split in two branches the main input power coming from the klystron, and two rounded arms that fed the two input of the coupling cell. In figure 5.10 is reported the HFSS model of the splitter.

The two quantities a and b of the splitter have been used to minimize the reflection coefficient S_{11} and to ensure the correct power splitting. The parameter d instead has been used to tune the 3dB splitter at the correct working frequency (2856 MHz). Figure 5.11 reports the results of the tuning and optimization of the splitter through Ansys HFSS. At the frequency of 2856 MHz a reflection coefficient of -59 dB and the transmission coefficients S_{21} and S_{31} are both -3.007 dB have been obtained.

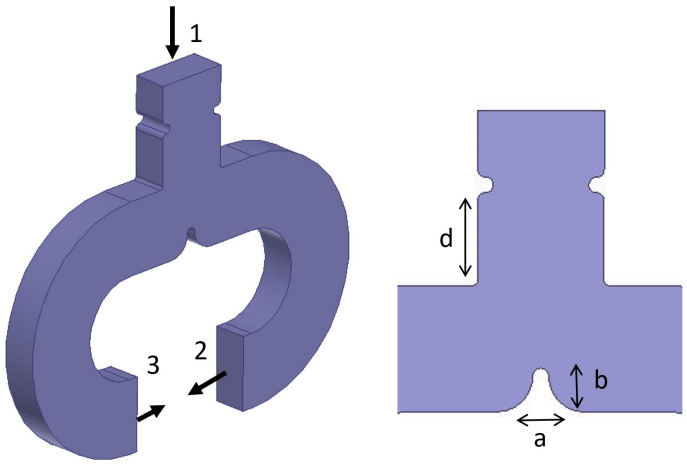

Figure 5.10: HFSS model of the designed splitter (left), detail of the 3dB power divider of the splitter with the parameters used for its tuning (right).

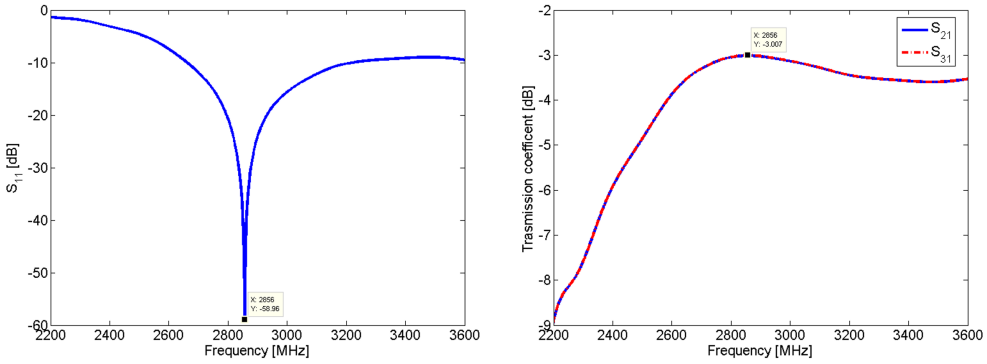

Figure 5.11: Reflection (left) and transmission (right) coefficients of the splitter after the tuning at 2856 GHz.

Finally, in Figure 5.12, is showed the electric field magnitude along the splitter for an input power of 40 MW, obtained after the optimization. As it was done previously in the case of the coupler, the pulsed heating on the surfaces has to be evaluated to avoid breakdown phenomena. Through peak magnetic field calculation reported in Figure 5.12 and the formula 5.15 a temperature increase of 0.2°C has been calculated, considering an RF pulse of 1μs.

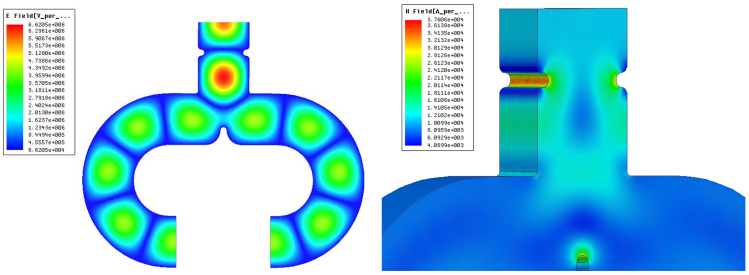

Figure 5.12: Electric field magnitude inside the splitter, for $40\,MW$ input power, after the optimization (left), magnetic field magnitude on the rounded surfaces of the 3dB splitter.

Final design results

Finally to verify the electromagnetic design of the coupler and of the cells and to evaluate the overall performances a 7 cell model of the TW structure has been simulate with Ansys HFSS. In Figure 5.13 is reported the simulated geometry. The amplitude and phase of the accelerating field are given in Figures 5.14 and 5.15 for a 7 cell plus in/out couplers structure.

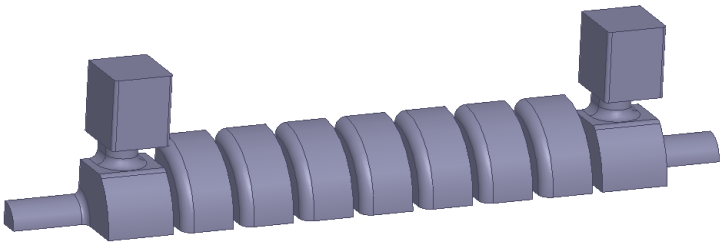

Figure 5.13: Model of a 7 cells structure simulated with Ansys HFSS.

An input reflection coefficient lower than -37 dB has been found at the working frequency, the simulated phase shift between two adjacent accelerating cells is equal to $(120 \pm 0.5)^{\circ}$. In Table 5.2 are summarized the main parameters for the designed 10-cell S-band prototype.

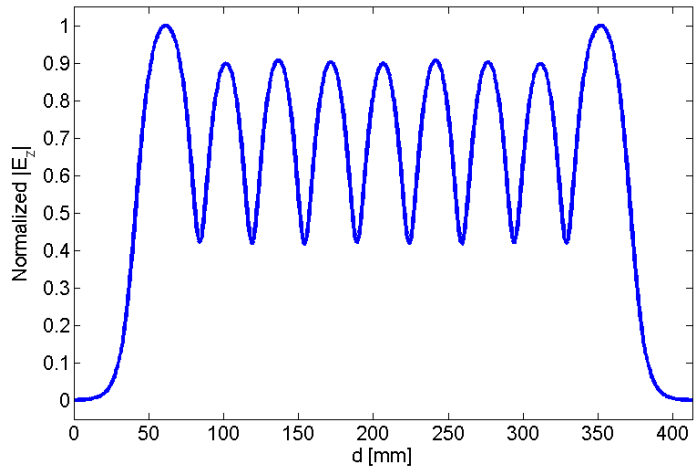

Figure 5.14: Normalized electric field module on the axis of a 7 cells structure.

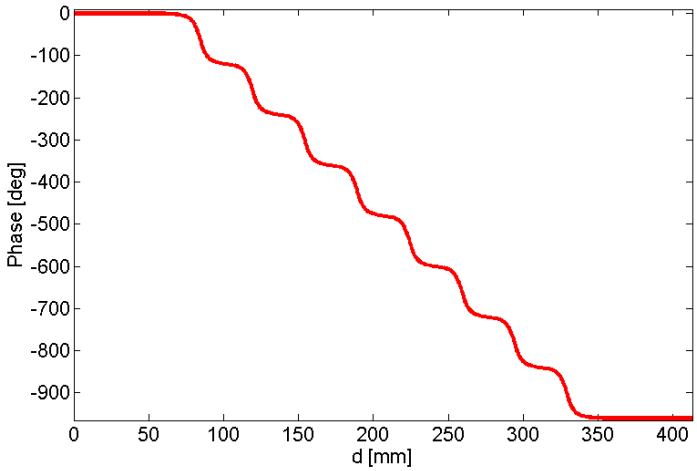

Figure 5.15: Electric field phase on the axis of a 7 cells structure.

5.3 Mechanical design of the S-band prototype

The mechanical design has been performed through Autodesk Inventor [83] that is a 3D modeling software for mechanical design. The main challenge of this design was to implement the gaskets technique without affecting electromagnetic performances. For this reason the use of the electromagnetic code has been performed in parallel to the mechanical design of the different components

Parameter	Value
Working frequency	2856 MHz
Phase advance per cell	$2\pi/3$
Number of cell	10 + 2
Structure type	CI
Structure length	545 mm
Iris half aperture radius	13 mm
Period	34.99 mm
Unloaded quality factor Q_0	14200
Group velocity (v_g/c)	0.02
Field attenuation	0.11 m^{-1}
Shunt impedance r_{shunt}	55 $M\Omega/m$
Series impedance Z_{series}	11.67 $M\Omega/m$
$E_{acc}/\sqrt{P_{in}}$	3.4 $\frac{MV/m}{\sqrt{MW}}$
Pulsed heating (for 1μs pulse length)	$< 17°C$

Table 5.2: Main parameters of the 10 cell S-band TW structure realized with the clamping-gasket technique.

and a continuous feedback between the two designs has been necessary.

As already mentioned, in the gasket-clamping technique the various machined copper components of the structure are clamped together by means of simple screws and using special RF-vacuum gaskets [74]. This gaskets guarantees at the same time the RF contact and a perfect vacuum sealing, avoiding sharp edges and gaps. The gaskets are made of copper realized with high precision lathe. In Figure 5.16 the transverse section of the gasket is reported.

The sealing and the RF contact are realized by compression of the gasket. The gasket is compressed to the correct value when the two outer parts of the cells reach the mechanical contact. In the prototype three kinds of special gaskets are used with different shapes to adapt to different profiles of the parts to combine. In Figure 5.17 the models of the three designed gaskets are reported.

The circular shaped gaskets are used to combine the regular cells, like the one used in [73], while the racetrack shaped gaskets are used between the input/output couplers and their adjacent cells. The transverse dimensions of the gasket are 1.3 mm $\times$ 4 mm and the surface that guarantees the rf/vacuum contact is of 0.25 mm. The gasket is compressed by only 0.2 mm in order to guarantee

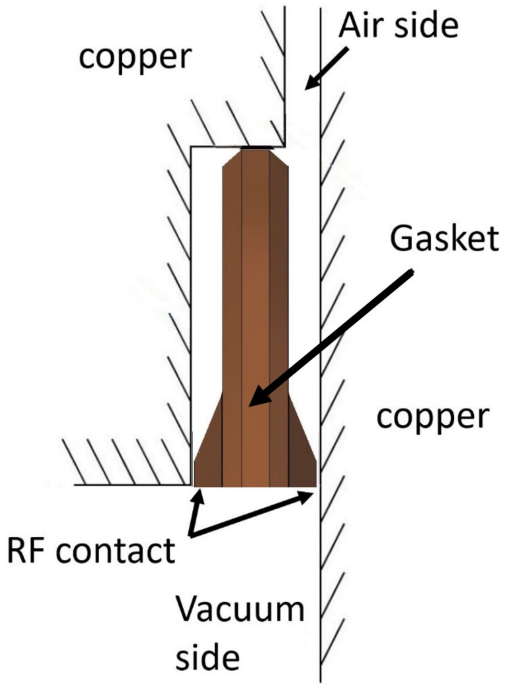

Figure 5.16: Sketch of the transverse profile of the special vacuum/rf gasket used for gasket clamping technique.

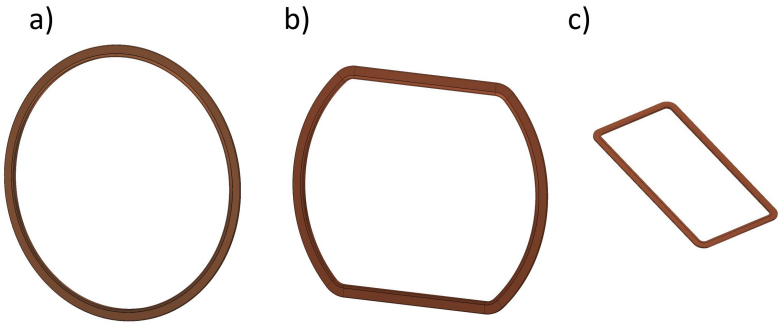

Figure 5.17: Model of the special rf/vacuum gaskets designed with Autodesk Inventor: a) gasket used to link adjacent cells, b) gasket used to link the input/output coupler cell to the adjacent cell, c) gasket used to link the output waveguide to che coupler cell.

an elastic deformation of the gasket itself during its compression. The compression factor has been incremented with respect to the one used for the ELI gun in order to have a stronger contact after the gasket compression. The last type of gasket has a rectangular shape and is used to connect the output waveguide to

the coupling cell.

The prototype structure is composed by an input coupler, ten accelerating cells and an output coupler sealed with a final closing cap. All the cells are mechanically identical except those two adjacent to the couplers that have a different profile to allow the connection with the couplers themselves. Figure 5.18 shows the detail of a single cell. It has eight through-holes and eight threaded holes for the connection with the two adjacent cells disposed at 45 degree to provide an homogeneous force on the gasket when the cells are clamped together. Threaded holes are used to clamp the cell with the previous one as showed in Figure 5.21 and to clamp together the different parts M8 hexagonal head screw torque are used.

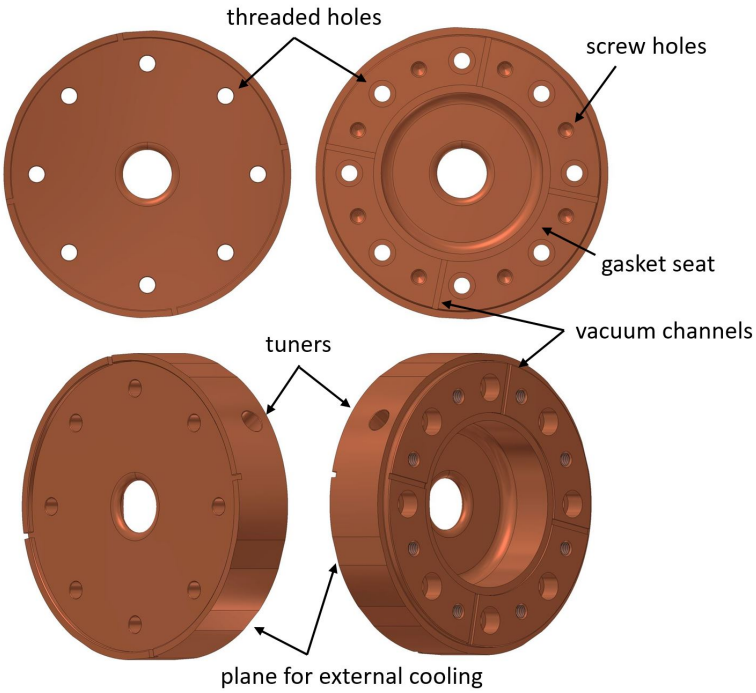

Figure 5.18: Different views of the single cell components designed with Autodesk Inventor.

Two opposite bi-directional tuners of the same type used for the ELI C-band structures tuning, are inserted on each cell and on the couplers. Each cell presents a step, on the outer edge, for cell alignment during assembly and four

longitudinal planes on the external surface, that will be used to weld four pipes for external cooling system once the structure is assembled in its final configuration. In Figures 5.19 and 5.20 the models of the input/output coupler cells and of the closing cap that complete the output coupler cell are reported.

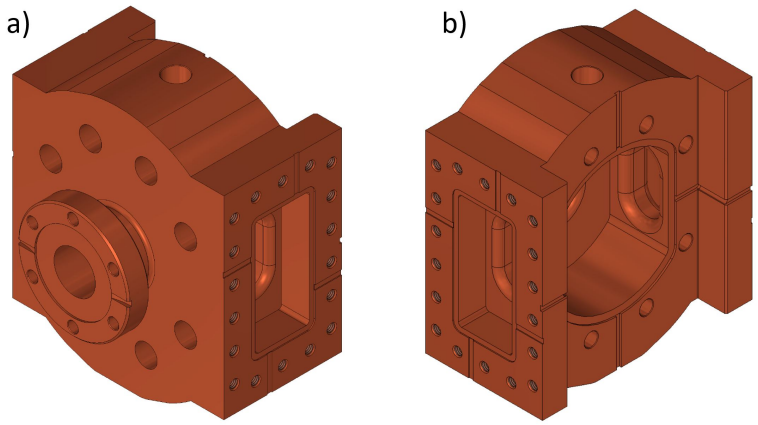

Figure 5.19: Mechanical drawings of the of the input coupler: front view(a), back view(b).

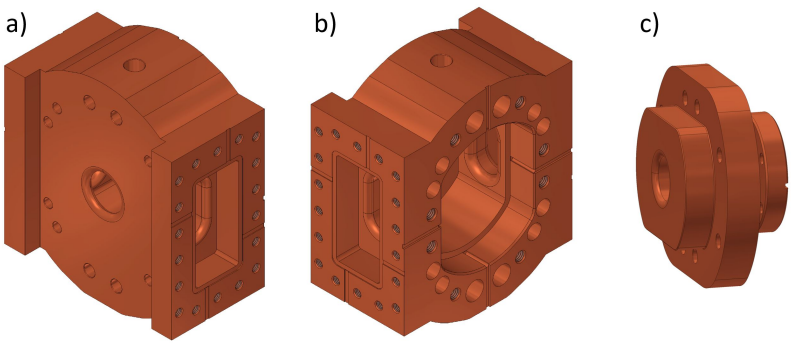

Figure 5.20: Mechanical drawings of the of the output coupler: front view(a), back view(b) and closing cap(c).

Also in this case, it's important to provide a uniform and well distributed pressure on the gaskets when the coupler cell is clamped with the adjacent cell. So, in order to compress it in an homogeneous way the screws have been distributed regularly around the cell profile and as close as possible to the gasket. Once all the different parts will be fabricated, the structure can be assembled.

The assembly procedure will start from the the input coupler, then all the cell are stacked up one after the other, inserting the gaskets between them and fixing each part with the previous one through screws.

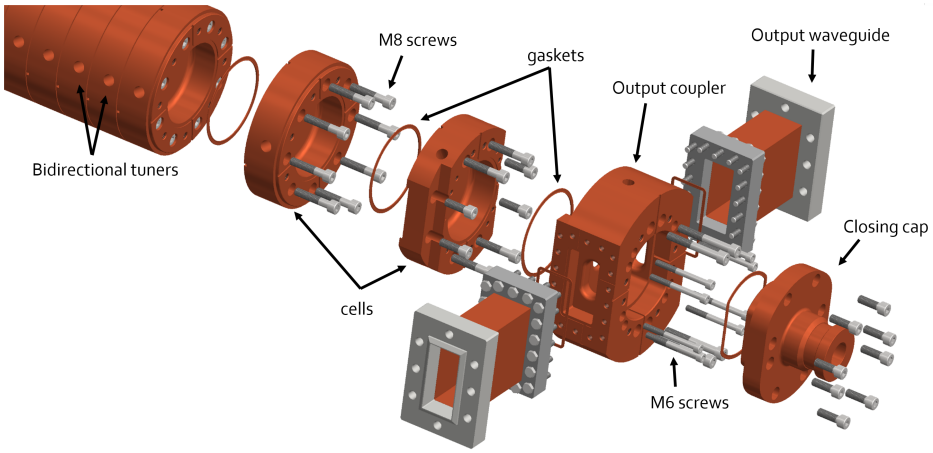

Figure 5.21: Mechanical drawing of the 10 cells S-band prototype: detail of the assembly procedure.

Figure 5.21 shows the details of the structure assembly. The assembly ends with the installation of the output coupler cell, the closing cap and the input/output waveguides. Each part will be fabricated from cylinders of Oxygen Free High Conductivity (OFHC) copper. The single cell will be machined as a cup using a high precision lathe. The input and output coupler instead will be realized with a computer controlled milling machine. Figure 5.22 reports the complete assembled structure and his longitudinal section.

5.4 Results and next steps

An intense activity of prototyping has been started in order to validate all the design technical choices and to test the performance of this Linac. Moreover, this was also an opportunity to verify and optimize the manufacturing procedures for the machining of the different components.

A first prototype has been realized to test the vacuum sealing realized by the special gasket. A simple scheme composed only by two half cells components sealed through a cell gasket (showed in 5.17(a)) has been designed. In Figure

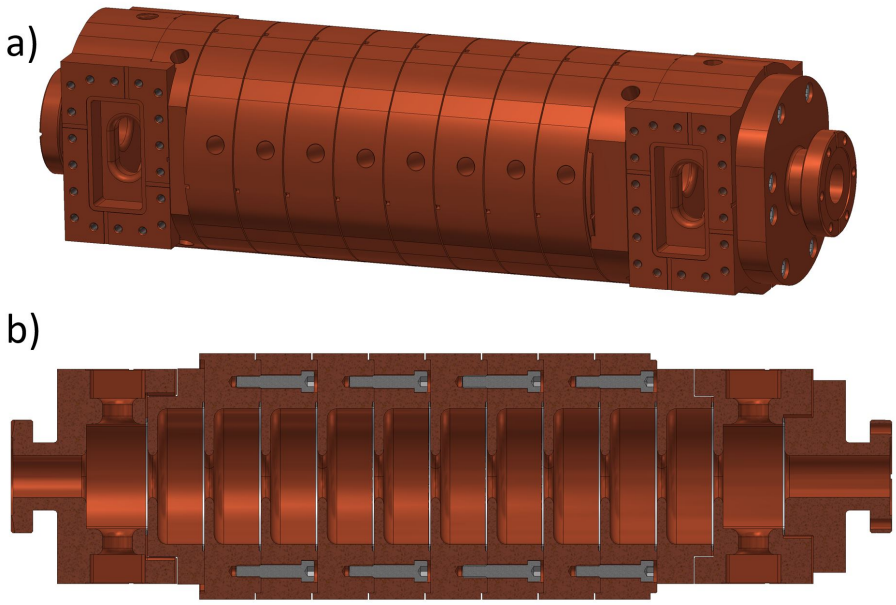

Figure 5.22: Mechanical drawing of the 10 cells S-band prototype (a) and longitudinal secion of the assembled structure (b).

5.23 the mechanical design is reported. To test the proper functioning of the gasket and the presence of vacuum leaks after its compression, that cell implements the same kind of RF/vacuum sealing that will be used in the final configuration of the Linac.

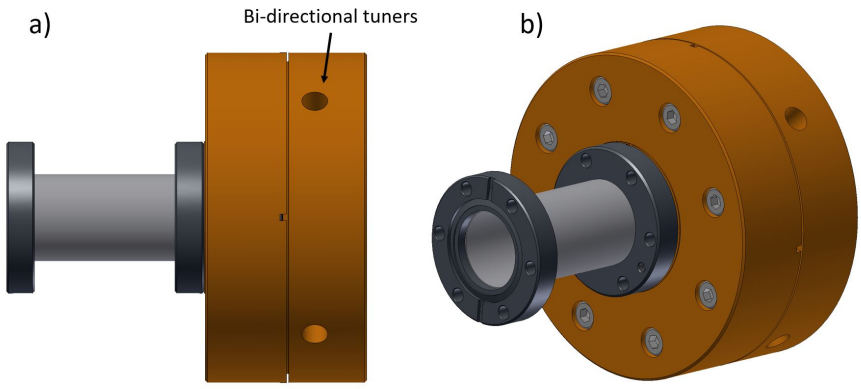

Figure 5.23: Mechanical drawing of the single cell prototype used for vaccum and tuners tests.

The two half cells components of this first prototype have been realized at the INFN-Roma1 workshop while the gasket has been realized by an external company. In Figure 5.24 is possible to see the two machined components before clamping and the entire cell. On this prototype also a test of the bi-directional tuners will be performed. For this reason, four bi-directional tuners with different thickness (1 mm, 1.25 mm, 1.5 mm and 1.75 mm) from the cell wall have been implemented.

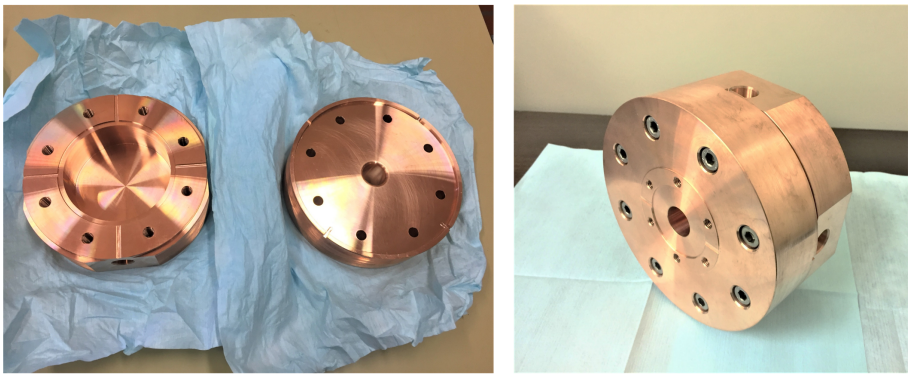

Figure 5.24: Machined half cell components for the vacuum test before (left) and (after) clamping.

We are now working in the realization of a second full scale prototype for low power RF test. This second prototype will be realized in aluminum and is based on a simplified mechanical design, reported in Figure 5.25. This structure will be used to verify the RF design properties and so all the internal dimensions and tolerances correspond to those of the final structure.

Finally, high power and vacuum leak test will be conducted on a final copper 10 cell structure prototype. Figure 5.26 shows this prototype in his final configuration for high power RF test. It implements also the splitter for symmetrical feeding of the input ports and the two RF loads.

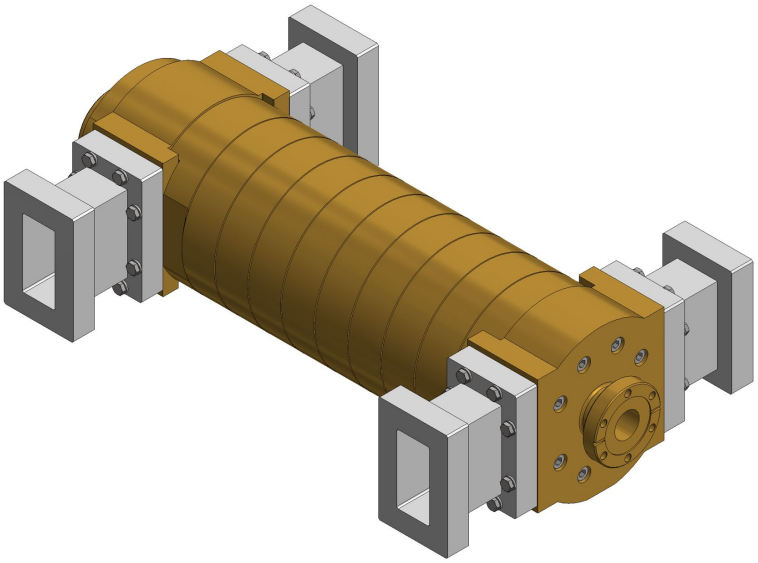

Figure 5.25: Mechanical drawing of the simplified alluminum/brass prototype used for radiofrequency test.

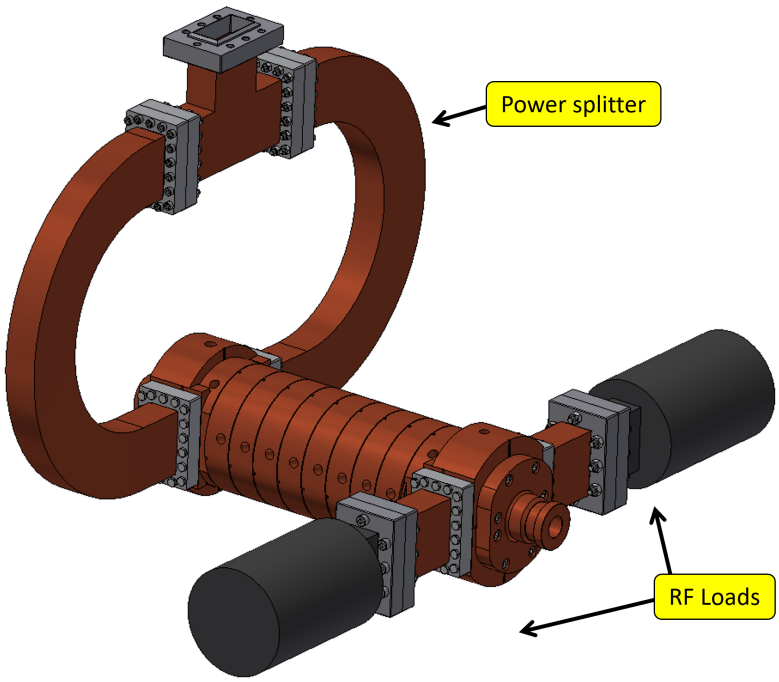

Figure 5.26: Mechanical drawing of the 10 cells S-band TW Linac realized with the gasket-clamped technique in his final configuration.

Conclusions

This Ph.D. work has been performed in the framework of activities of the RF, Vacuum and Linac group of the Frascati laboratories of INFN, related to the ELI Nuclear Physics Gamma Beam System (ELI-NP-GBS) project.

In the ELI-NP-GBS a high power Laser pulse is Compton scattered with an electron beam generated through an high brightness Linac. In this way a highly polarized, and nearly mono-energetic γ ray beam with a tunable energy from about 0.2 MeV to 19.5 MeV and a high spectral density (10^4 photons/s·eV) is produced. This unique gamma-ray beam has a wide range of applications from nuclear physics to astrophysics, from medical research to homeland security and industrial applications. The high photon beam performances impose strong requirements on the electron beam, thus on the Linac and his RF system. The Linac is required to achieve a normalized emittance in both directions lower than 0.5 mm·mrad and an energy spread below 0.1%. Moreover to increase the maximum photon flux the Linac has to work in multibunch mode with a repetition rate of 100 Hz. Since the performance of the RF system obviously affect those of the electron beam, great care is needed in its design and commissioning. Starting from the RF waveguide network, the entire RF system of the ELI-NP Linac has been described in detail in this dissertation.

Overall, 13 RF sources feed the Linac, these are composed by a Toshiba klystron and a Scandinova solid state modulator. The power sources fabricated

have been tested in order to verify their reliability and compliance with the requirements on the pulse to pulse stability ($< 0.005\%$) and pulse flatness ($< 1\%$). All the systems realized up to now have been successfully characterized and no serious faults have been detected during all the performed tests. The measurement set-up and the acceptance protocol used during this acceptance phase have been described.

Each accelerating structure is individually fed by a dedicated power station in order to have the possibility to shape each RF pulse thus compensating beam loading effects and variation of the RF amplitude along the bunch train. The C-band accelerating structures designed for the ELI-NP Source have been designed with a dipole HOM damping system to avoid beam break-up, in order to allow the multi-bunch operation. The machining technology used to realized accelerating structures components has a limited precision in producing identical cells. Moreover, during the brazing process the structure is subjected to high thermal stress that can lead to further modification of the cells internal dimensions. Therefore, a tuning procedure has been necessary to ensure the right phase advance between adjacent cells, and minimize the reflection from the detuned cells. For this reason an automatic bead-pull measurement set-up and a tuning algorithm have been implemented through a Labview interface in order to tune the fabricated structures. Nowadays four ELI-NP C-band structures have been realized, tuned and tested successfully. For each structure a deviation $< \pm 2^\circ$ on the delta phase advance per cell $\Delta\phi$ and a total cumulative phase advance excursion $< 5^\circ$ have been obtained. The set-up, the methodology and the results of the procedure used have been illustrated in the thesis. High power conditioning of the accelerating structure is necessary to reach the nominal parameters in term of accelerating gradient and pulse duration. For this reason, an high power test has been performed on the first C-band structures. In about 190 hours of RF conditioning, it reached the nominal parameters in terms of gradient (33 MV/m), repetition rate (100 Hz) and pulse length (800 ns) with a breakdown rate at the end of the conditioning of the order 10^{-6} bpp/m. A preliminary study of the beam loading effects in the C-band sections has been also performed. These effects have to be properly compensated with the LLRF system, shaping the driver pulse, in order to control the bunch by bunch energy variation along the train.

A combined test of LLRF, modulator and klystron system will be conducted to estimate the bandwidth limitations on the proposed beam loading compensation method.

The ELI-NP Linac particle source is a 1.6 cell RF photo-gun that implement several new features both from the electromagnetic and mechanical point of view. In particular, it implements the new realization technique, called "Gasket-Clamping technique", that has been recently developed at the INFN laboratory of Frascati [74]. This technique allows avoiding the brazing process in the fabrication procedure by using special RF-vacuum gaskets that guarantee, at the same time, the radiofrequency contact and the vacuum sealing while the different machined parts are clamped together. To completely characterize the device an automatic measurement set-up has been implemented. The assembly and low level RF measurements of this device have been presented and the recent high power test conducted at the university of Bonn has been described extensively. Full parameter have been achieved in about 150 hours of conditioning with overall extremely good performances.

Taking into account the optimum results obtained by the RF Gun, the possibility to extend the new gasket clamping technique to the realization of an entire travelling wave Linac structure has been explored with the design of an S-band TW accelerating structure. In this work the electromagnetic and mechanical design of this prototype have been presented emphasizing their strong correlation. From the electromagnetic point of view. every aspect of the design has been considered: cell design, coupler design, field distortions and pulsed heating. The first single cell prototype for vacuum leak test, has been recently realized at the INFN-Roma1 workshop and a 10 cell structure based on reported design will be realized to perform low and high power RF tests. An intense prototype activity has been started and will open new perspectives to further extensions of this technique to the realization of more complicated C/X-band structures able to work in multibunch operation and at high repetition rate. This approach can have also a strong economic and industrial impact worldwide, since, in principle, all Companies that are able to machine with high precision copper components, will be able to fabricate a Linac structure.

APPENDIX

A

Figures of merits of a single cell

The main figures of merit for a single cell of a travelling wave structure are given below:

$$Z = \frac{E_{acc}^2}{Pin} \qquad \text{Series impedance} \tag{A.1}$$

$$\alpha = \frac{p_{diss}}{2Pin} \qquad \text{Field attenuation constant} \tag{A.2}$$

$$v_g = \frac{P_{in}}{w} \qquad \text{Group velocity} \tag{A.3}$$

$$r = \frac{E_{acc}^2}{p_{diss}} \qquad \text{Shunt impedance per unit length} \tag{A.4}$$

defining E_z the complex accelerating field on axis and D the single cell length, we have:

$$eV_z = e\left|\int_0^D E_z \cdot e^{j\omega\frac{z}{c}} dz\right| \quad \text{is the single cell energy gain,}$$

$$E_{acc} = \frac{V_z}{D} = \frac{\left|\int_0^D E_z \cdot e^{j\omega\frac{z}{c}} dz\right|}{D} \quad \text{is the accelerating field in the cell,}$$

$$P_{in} = \int_S \frac{1}{2} Re(\underline{E} \times \underline{H}^*) \cdot \hat{z} dS \quad \text{is the average input power (flux power),}$$

$$P_{diss} = \frac{1}{2} R_s \int_{S_{ext}} |H_{tan}|^2 \, dS_{ext} \quad \text{is the average dissipated power in the cell,}$$

$$p_{diss} = \frac{P_{diss}}{D} \quad \text{is the average dissipated power per unit length,}$$

$$W_h = \frac{1}{4}\mu_0 \int_V \underline{H} \cdot \underline{H}^* dV \quad \text{is the stored magnetic energy in the cell,}$$

$$W_e = \frac{1}{4}\varepsilon_0 \int_V \underline{E} \cdot \underline{E}^* dV \quad \text{is the stored electric energy in the cell and}$$

$$w = \frac{W_e + W_h}{D} \quad \text{is the stored energy per unit length.}$$

Bibliography

[1] V. Petrillo *et al.*, "Photon flux and spectrum of γ-rays Compton sources," *Nuclear Instruments and Methods in Physics Research Section A: Accelerators, Spectrometers, Detectors and Associated Equipment*, vol. 693, pp. 109–116, 2012.

[2] C. Sun *et al.*, "Theoretical and simulation studies of characteristics of a Compton light source," *Physical review special topics-accelerators and beams*, vol. 14, no. 4, p. 044701, 2011.

[3] R. H. Milburn, "Electron scattering by an intense polarized photon field," *Physical Review Letters*, vol. 10, no. 3, p. 75, 1963.

[4] F. Arutyunian *et al.*, "The Compton effect on relativistic electrons and the possibility of obtaining high energy beams," *Physics Letters*, vol. 4, no. 3, pp. 176–178, 1963.

[5] L. Federici *et al.*, "Backward Compton scattering of laser light against high-energy electrons: the LADON photon beam at Frascati," *Il Nuovo Cimento B (1971-1996)*, vol. 59, no. 2, pp. 247–256, 1980.

[6] F. Amman *et al.*, "Two-beam operation of the 1.5 GeV electron-positron storage ring adone," *Lettere Al Nuovo Cimento (1969-1970)*, vol. 1, no. 15, pp. 729–737, 1969.

[7] C. Vaccarezza *et al.*, "The SPARC˙LAB Thomson source," *Nucl. Instrum. Meth.*, vol. A829, pp. 237–242, 2016.

[8] C. Tang *et al.*, "Tsinghua Thomson scattering X-ray source," *Nuclear Instruments and Methods in Physics Research Section A: Accelerators, Spectrometers, Detectors and Associated Equipment*, vol. 608, no. 1, pp. S70–S74, 2009.

[9] W. Brown *et al.*, "Experimental characterization of an ultrafast Thomson scattering x-ray source with three-dimensional time and frequency-domain analysis," *Physical Review Special Topics-Accelerators and Beams*, vol. 7, no. 6, p. 060702, 2004.

[10] F. E. Carroll *et al.*, "Pulsed tunable monochromatic X-ray beams from a compact source: new opportunities," *American journal of roentgenology*, vol. 181, no. 5, pp. 1197–1202, 2003.

[11] S. Kashiwagi *et al.*, "Compact soft x-ray source using Thomson scattering," *Journal of applied physics*, vol. 98, no. 12, p. 123302, 2005.

[12] E. Miura *et al.*, "X-ray generation via laser Compton scattering using quasi-monoenergetic electron beam driven by laser-plasma acceleration," in *Advanced Accelerator Concepts: 15th Advanced Accelerator Concepts Workshop*, vol. 1507, no. 1. AIP Publishing, 2012, pp. 304–309.

[13] E. Eggl *et al.*, "The Munich Compact Light Source: initial performance measures," *Journal of Synchrotron Radiation*, vol. 23, no. 5, pp. 1137–1142, Sep 2016. Available online: https://doi.org/10.1107/S160057751600967X

[14] A. Bacci *et al.*, "The Star Project," in *Proceedings, 5th International Particle Accelerator Conference (IPAC 2014): Dresden, Germany, June 15-20, 2014*, 2014, p. WEPRO115. Available online: http://jacow.org/IPAC2014/papers/wepro115.pdf

[15] A. Variola *et al.*, "ThomX conceptual design report," *LAL RT*, vol. 9, p. 28, 2010.

[16] E. Eggl *et al.*, "X-ray phase-contrast tomography with a compact laser-driven synchrotron source," *Proceedings of the National Academy of Sciences*, vol. 112, no. 18, pp. 5567–5572, 2015.

[17] R. Hajima *et al.*, "Proposal of nondestructive radionuclide assay using a high-flux gamma-ray source and nuclear resonance fluorescence," *Journal of Nuclear Science and Technology*, vol. 45, no. 5, pp. 441–451, 2008.

[18] T. Shizuma *et al.*, "Nondestructive identification of isotopes using nuclear resonance fluorescence," *Review of Scientific Instruments*, vol. 83, no. 1, p. 015103, 2012.

[19] "The White Book of ELI Nuclear Physics," 2011. Available online: http://www.eli-np.ro/documents/ELI-NP-WhiteBook.pdf

[20] C. Vaccarezza *et al.*, "A European Proposal for the Compton Gamma-ray Source of ELI-NP," *Conf. Proc.*, vol. C1205201, pp. 1086–1088, 2012.

[21] L. Serafini *et al.*, "Technical Design Report EuroGammaS proposal for the ELI-NP Gamma beam System," 2014.

[22] "EuroGammaS Association." Available online: http://www.e-gammas.com/

[23] L. Serafini *et al.*, "High intensity X/γ photon beams for nuclear physics and photonics," in *EPJ Web of Conferences*, vol. 117. Nuclear Structure, 2016, p. 05002.

[24] K. Dupraz *et al.*, "Design and optimization of a highly efficient optical multipass system for γ-ray beam production from electron laser beam Compton scattering," *Physical Review Special Topics-Accelerators and Beams*, vol. 17, no. 3, p. 033501, 2014.

[25] K. Dupraz, "Conception et optimisation d,Äôun recirculateur optique pour la source haute brillance de rayons gamma d,ÄôELI-NP," Ph.D. dissertation, Paris 11, 2015.

[26] A. Bacci *et al.*, "Electron linac design to drive bright Compton backscattering gamma-ray sources," *Journal of Applied Physics*, vol. 113, no. 19, p. 194508, 2013.

[27] V. Fusco *et al.*, "Beam dynamics study of a C-band linac driven FEL with S-band photo-injector," *Proceedings of PAC09, Vancouver, May 2009*, vol. TH5PFP066.

[28] D. Alesini *et al.*, "Status of the SPARC project," *Nuclear Instruments and Methods in Physics Research Section A: Accelerators, Spectrometers, Detectors and Associated Equipment*, vol. 528, no. 1, pp. 586–590, 2004.

[29] A. Mostacci *et al.*, "Operational experience on the generation and control of high brightness electron bunch trains at SPARC-LAB," in *SPIE Optics+ Optoelectronics*. International Society for Optics and Photonics, 2015, pp. 95 121Q–95 121Q.

[30] M. Ferrario *et al.*, "Experimental Demonstration of Emittance Compensation with Velocity Bunching," *Phys. Rev. Lett.*, vol. 104, p. 054801, Feb 2010. Available online: http://link.aps.org/doi/10.1103/PhysRevLett.104.054801

[31] R. E. Collin, *Foundations for microwave engineering*. John Wiley & Sons, 2007.

[32] A. S. Gilmour, *Principles of Klystrons, Traveling Wave Tubes, Magnetrons, Cross-Field Ampliers, and Gyrotrons*, 1st ed. Artech House, 2011.

[33] F. Sannibale *et al.*, "DAϕNE Linac commissioning results," *Dafne technical notes, INFN-LNF, Accelerator Division*, vol. BM-2, 1997.

[34] B. Buonomo *et al.*, "DAϕNE Linac: Beam diagnostic and outline of last improvement," *TUPWA057, these proceedings, IPAC*, vol. 15.

[35] R. Cassel *et al.*, "A solid state induction modulator for SLAC NLC," in *Particle Accelerator Conference, 1999. Proceedings of the 1999*, vol. 3. IEEE, 1999, pp. 1494–1496.

[36] C. Pappas *et al.*, "Power modulators for FERMI's linac klystrons," in *2007 IEEE Particle Accelerator Conference (PAC)*. IEEE, 2007, pp. 2448–2450.

[37] W. Crewson *et al.*, "Power modulator," May 18 1999, uS Patent 5,905,646. Available online: https://www.google.com/patents/US5905646

[38] E. Cook, "Review of Solid-State Modulators," *Invited paper at the 20th International Linear Accelerator Conference, Monterey, CA*, 2000.

[39] "ScandiNova Systems AB." Available online: http://www.scandinovasystems.com/

[40] "Toshiba electron tubes and devices Co Ltd." Available online: http://www.toshiba-tetd.co.jp/eng/tech/klystron.htm//

[41] "Microwave amplifiers Ltd." Available online: https://microwaveamps.co.uk/

[42] "Instrumentation tecnology." Available online: http://www.i-tech.si/

[43] D. Alesini *et al.*, "The damped C-band RF structures for the European ELI-NP proposal," *Proceedings of IPAC2013, Shanghai, China*, p. 2726, 2013.

[44] D. Alesini *et al.*, "Design and RF test of damped C-band accelerating structures for the ELI-NP linac," in *Proceedings of 5th International Particle Accelerator Conference (IPAC 2014), THPRI042*, 2014.

[45] D. Alesini *et al.*, "Design of high gradient, high repetition rate damped C-band RF structures for the european ELI-NP Project," *submitted to PRST*, 2016.

[46] D. Alesini *et al.*, "The C-Band accelerating structures for SPARC photoinjector energy upgrade," *Journal of Instrumentation*, vol. 8, no. 05, p. P05004, 2013.

[47] D. Alesini *et al.*, "Design, realization and test of C-band accelerating structures for the SPARC˙LAB linac energy upgrade," *Nuclear Instruments*

and Methods in Physics Research Section A: Accelerators, Spectrometers, Detectors and Associated Equipment, vol. 837, pp. 161 – 170, 2016. Available online: http://www.sciencedirect.com/science/article/pii/S0168900216309342

[48] V. Pettinacci *et al.*, "Thermal-mechanical analysis of the RF structures for the ELI-NP proposal."

[49] S. A. Heifets *et al.*, "Coupling impedance in modern accelerators," *Rev. Mod. Phys.*, vol. 63, pp. 631–673, Jul 1991. Available online: http://link.aps.org/doi/10.1103/RevModPhys.63.631

[50] R. M. Jones, "Wakefield suppression in high gradient linacs for lepton linear colliders," *Phys. Rev. ST Accel. Beams*, vol. 12, p. 104801, Oct 2009. Available online: http://link.aps.org/doi/10.1103/PhysRevSTAB.12.104801

[51] W. Wuensch, "CLIC accelerating structure development," CERN, Tech. Rep., 2008.

[52] "Comeb." Available online: http://www.comeb.it/

[53] D. Alesini *et al.*, "Realization and High Power Tests of Damped C-Band Accelerating Structures for the ELI-NP Linac," in *Proceedings, 7th International Particle Accelerator Conference (IPAC 2016): Busan, Korea, May 8-13, 2016*, 2016, p. MOPMW004. Available online: http://inspirehep.net/record/1469618/files/mopmw004.pdf

[54] C. W. Steele, "A nonresonant perturbation theory," *IEEE Transactions on Microwave theory and Techniques*, vol. 14, no. 2, pp. 70–74, 1966.

[55] J. Shi *et al.*, "Tuning of CLIC accelerating structure prototypes at CERN," Tech. Rep., 2010.

[56] D. Alesini *et al.*, "Tuning procedure for traveling wave structures and its application to the C-Band cavities for SPARC photo injector energy upgrade," *Journal of Instrumentation*, vol. 8, no. 10, p. P10010, 2013. Available online: http://stacks.iop.org/1748-0221/8/i=10/a=P10010

[57] T. P. Wangler, *RF Linear accelerators*. John Wiley & Sons, 2008.

[58] E. Persico *et al.*, "Principles of particle accelerators," 1968.

[59] "Research Instrument GmbH." Available online: http://research-instruments.de/

[60] D. Boussard, "Beam loading," *CERN Accelerator School, Oxford, England*, pp. 16–27, 1985.

[61] A. Giribono *et al.*, "6D phase space electron beam analysis and machine sensitivity studies for ELI-NP GBS," *Nucl. Instrum. Meth.*, vol. A829, pp. 274–277, 2016.

[62] C. Adolphsen *et al.*, "Beam loading compensation in the NLCTA," in *Particle Accelerator Conference, 1997. Proceedings of the 1997*, vol. 2. IEEE, 1997, pp. 1676–1678.

[63] O. Kononenko *et al.*, "Transient beam-loading model and compensation in Compact Linear Collider main linac," *Physical Review Special Topics-Accelerators and Beams*, vol. 14, no. 11, p. 111001, 2011.

[64] S. Liu *et al.*, "Beam loading compensation for acceleration of multi-bunch electron beam train," *Nuclear Instruments and Methods in Physics Research Section A: Accelerators, Spectrometers, Detectors and Associated Equipment*, vol. 584, no. 1, pp. 1–8, 2008.

[65] M. Satoh *et al.*, "Initial-beam-loading compensation system for high-intensity electron linacs," *Nuclear Instruments and Methods in Physics Research Section A: Accelerators, Spectrometers, Detectors and Associated Equipment*, vol. 538, no. 1, pp. 116–126, 2005.

[66] D. Schulte *et al.*, "Beam loading compensation in the main linac of CLIC," *arXiv preprint physics/0008132*, 2000.

[67] L. Piersanti *et al.*, "The RF System of the ELI-NP Gamma Beam Source," in *Proceedings, 7th International Particle Accelerator Conference (IPAC*

2016): Busan, Korea, May 8-13, 2016, 2016, p. MOPMW006. Available online: http://inspirehep.net/record/1469620/files/mopmw006.pdf

[68] L. Palumbo *et al.*, "Wake fields and impedance," in *Advanced accelerator physics. Proceedings, 5th Course of the CERN Accelerator School, Rhodos, Greece, September 20-October 1, 1993. Vol. 1, 2*, 1994, pp. 331–390.

[69] I. V. Bazarov *et al.*, "Maximum achievable beam brightness from photoinjectors," *Physical review letters*, vol. 102, no. 10, p. 104801, 2009.

[70] P. Musumeci *et al.*, "Experimental generation and characterization of uniformly filled ellipsoidal electron-beam distributions," *Physical review letters*, vol. 100, no. 24, p. 244801, 2008.

[71] J. Rosenzweig *et al.*, "Next generation high brightness electron beams from ultra-high field cryogenic radiofrequency photocathode sources," *arXiv preprint arXiv:1603.01657*, 2016.

[72] D. T. Palmer, "The next generation photoinjector," Stanford Linear Accelerator Center (SLAC), Tech. Rep., 1998.

[73] D. Alesini *et al.*, "New technology based on clamping for high gradient radio frequency photogun," *Physical Review Special Topics - Accelerators and Beams*, vol. 18, 2015.

[74] D. Alesini *et al.*, "Process for manufacturing a vacuum and radio-frequency metal gasket and structure incorporating it," Int'l patent application PCT/IB2016/051464 assigned to INFN.

[75] V. Dolgashev *et al.*, "RF Breakdown in normal conducting single-cell structures," 2005, 21st IEEE Particle Accelerator Conference, Knoxville, TN, USA, (IEEE, Piscataway, NJ).

[76] D. Alesini, "Power coupling," in *Proceedings, CAS - CERN Accelerator School: RF for Accelerators, Ebeltoft, Denmark, 8 - 17 Jun 2010*, 2011. Available online: https://inspirehep.net/record/1081347/files/arXiv:1112.3201.pdf

[77] J. Maier *et al.*, "Field measurements in resonant cavities," *Journal of applied physics*, vol. 23, no. 1, pp. 68–77, 1952.

[78] P. Baldini *et al.*, "DAϕNE cavity r & d: A shunt impedance measurement system based on the perturbative method," 1991".

[79] F. Cardelli *et al.*, "Design of Linac with the New Gaskets Clamping Fabrication Technique," in *Proceedings, 7th International Particle Accelerator Conference (IPAC 2016): Busan, Korea, May 8-13, 2016*, 2016, p. MOPMW005. Available online: http://inspirehep.net/record/1469619/files/mopmw005.pdf

[80] "Ansys HFSS." Available online: http://www.ansys.com

[81] R. B. Neal *et al.*, "The Stanford Two-Mile Accelerator," *Physics Today*, vol. 23, p. 76, 1970.

[82] D. Alesini *et al.*, "Design of couplers for traveling wave RF structures using 3D electromagnetic codes in the frequency domain," *Nucl. Instrum. Meth.*, vol. A580, pp. 1176–1183, 2007.

[83] "Autodesk INVENTOR." Available online: http://www.autodesk.it/products/inventor/overview

List of Figures

List of Tables